Dynamic Model Development and Simulation of an Autonomous Active AUV Docking Device using a Mechanically Actuated Mechanism to Recover AUVs to a Submerged Slowly Moving Submarine in Waves

by

Colin B. Gillis

BSc. in Engineering, University of New Brunswick, 2011
Diploma in Engineering, St. Francis Xavier University, 2009

A THESIS SUBMITTED IN PARTIAL FULFILLMENT OF THE REQUIREMENTS FOR THE DEGREE OF

Masters of Science in Engineering

In the Graduate Academic Unit of Mechanical Engineering

Supervisor(s):	Juan A. Carretero, PhD, Mechanical Engineering (UNB)
	Rickey Dubay, PhD, Mechanical Engineering (UNB)
	Tiger Jeans, PhD, Mechanical Engineering (UNB)
	George D. Watt, PhD, Mechanical Engineering (DRDC)
Examining Board:	Edmund Biden, D.Phil., Mechanical Engineering
	Gordon Holloway, PhD, Mechanical Engineering
	Saleh Saleh, PhD, Electrical Engineering

This thesis is accepted by the

Dean of Graduate Studies

THE UNIVERSITY OF NEW BRUNSWICK

April, 2014

Abstract

Autonomous Underwater Vehicles (AUVs) are presenting an ever expanding range of applications that enhance human capabilities and mitigate human risk. Development of a successful subsurface autonomous launch and recovery system would expand the functional use of AUVs in many fields.

Defence Research and Development Canada (DRDC) is leading a collaborative project with the University of New Brunswick (UNB) to develop such a system that would recover AUVs to a slowly moving submerged submarine. This thesis provides an overview of the design, dynamic modelling, and preliminary control in simulation of an electro-mechanically actuated AUV dock concept, which operates without using hydrodynamic fluid power to provide motive force. The device is partially faired and has a R$\perp$R$\perp$P serial manipulator architecture. In short, the device is referred to as the mechanically actuated RRP serial manipulator.

High speed actuation of the device is required to compensate for relative trajectory errors between the submarine and AUV during significant sea states in littoral waters. Hydrodynamic forces present in water cannot be

ignored and will be modelled using the Morison Equation. Unimodal Linear Wave Theory is used to simulate AUV kinematics, establishing end effector design trajectories, as well as providing wave kinematics for hydrodynamic modelling. Alterations to the recursive Newton-Euler derivation of manipulator dynamics are explained, and results of simulations are presented. Model Predictive Control (MPC) of the mechanically actuated RRP serial manipulator is simulated using a Dynamic Matrix Control (DMC) architecture.

The dynamic models are verified analytically and provide accurate evaluation without lose of generality. Dynamic modelling shows the actuator loads for the proposed device are significant. Drag is the largest contributer and indicates the device must be streamlined. The link diameter used for simulation is overly conservative and should be optimized to reduce its size, this will decrease the required actuator loads. The control simulation shows the DMC controller is a robust design for tracking, however it needs to be combined in a cascading architecture to control both position and velocity for precise control.

Overall, the mechanically actuated RRP serial manipulator is a viable design but requires further modelling and development. The device becomes more promising as it is streamlined and reduced in overall length.

Dedication

For Heather.

Acknowledgements

I sincerely appreciate the ongoing support from Mom, Dad, Family, and close friends. Dr. George D. Watt (and Defence Research and Development Canada Atlantic) has coordinated the AUV Active Dock project, funded through the DRDC Technology Investment Fund, from its inception. The guidance from supervisors Dr. Juan Carretero, Dr. Rickey Dubay, Dr. Tiger Jeans, and Dr. George Watt have made this project a success and all have contributed to my growth as a professional. There has been significant collaboration and effort by DRDC, its colleagues and industrial partners, as well as the Faculty and Staff of the Department of Mechanical Engineering over the duration of the work. Thank you all, I enjoyed the challenge.

Table of Contents

List of Tables

List of Figures

Nomenclature

AUV	Autonomous Underwater Vehicle
DRDC	Defence Research and Development Canada
UNB	University of New Brunswick
ROV	Remotely Operated Vehicle
L&R	Launch and Recovery
JT	Joint Type
JC	Joint Configuration
DOF	Degrees of Freedom
$\perp$	Perpendicular
$\parallel$	Parallel
R	Revolute Joint
P	Prismatic Joint
U	Universal Joint
S	Spherical Joint
RRR	Revolute$\perp$Revolute$\parallel$Revolute serial manipulator
RRP	Revolute$\perp$Revolute$\perp$Prismatic serial manipulator

2$\underline{\text{P}}$UU-SS	2-Prismatic-Universal-Universal Spherical-Spherical parallel manipulator
$\equiv$	Equivalent
x	Cartesian position in x-axis
y	Cartesian position in y-axis
z	Cartesian position in z-axis
$\dot{x}$	Cartesian velocity in x-axis
$\dot{y}$	Cartesian velocity in y-axis
$\dot{z}$	Cartesian velocity in z-axis
$\ddot{x}$	Cartesian acceleration in x-axis
$\ddot{y}$	Cartesian acceleration in y-axis
$\ddot{z}$	Cartesian acceleration in z-axis
u	Fluid Velocity in x-axis
v	Fluid Velocity in y-axis
w	Fluid Velocity in z-axis
$\mathbf{q}$	Cartesian velocity vector of the onset fluid
$\dot{\mathbf{q}}$	Cartesian acceleration vector of the onset fluid
$c.v.$	Control Volume
$c.s.$	Control Surface
m	Mass
L	Length
ρ	Fluid Density
dV	Elemental Volume

$\mathbf{n}$	3×1 vector normal to an elemental plane on the control surface
dS	elemental surface area
∇	Cartesian gradient operator
C	Denotes a closed boundary
Γ	Circulation
$\mathbf{l}$	Line path of closed line integral
Φ	Velocity Potential of a fluid at a given Cartesian point
$\mathbf{p}$	Cartesian reference point
$\mathbf{p_o}$	Arbitrary Cartesian reference point
h	Overall Sea depth
e	Free surface elevation from the mean surface level $z = 0$ at position x and time t
g	Acceleration of Gravity
H	Wave Height
k	Wave Number
T	Wave Period
T_{min}	Minimum statistical wave period
T_{avg}	Average statistical wave period
T_{max}	Maximum statistical wave period
θ_x	Angular coordinates of the horizontal, x-axis, particle kinematics
θ_z	Angular coordinates of the vertical, z-axis, particle kinematics
0	Denotes base frame of manipulator
ee	Denotes end effector frame of manipulator

α_{i-1}	Link twist
a_{i-1}	Link length
d_i	Joint offset
$\theta_{\mathbf{i}}$	Joint angle i
$\dot{\theta}$	Joint velocity i
$\ddot{\theta}$	Joint acceleration i
$\mathbf{\Theta}$	Joint angle vector $(i \times 1)$ of joint angles i
$\dot{\mathbf{\Theta}}$	Joint velocity vector $(i \times 1)$ of joint velocities i
$\ddot{\mathbf{\Theta}}$	Joint acceleration vector $(i \times 1)$ of joint accelerations i
${}^{i}_{i-1}\mathbf{T}$	Homogeneous transformation matrix describing frame $\{i\}$ as seen from frame $\{i-1\}$
${}^{i}_{i-1}\mathbf{R}$	Rotation matrix describing the rotation of frame $\{i\}$ as seen from frame $\{i-1\}$
${}^{i}_{i-1}\mathbf{p}$	Cartesian position vector of frame i as seen from frame $i-1$
$\mathbf{x}$	Cartesian position vector of x, y, and z displacements
$\dot{\mathbf{x}}$	Cartesian velocity vector of $\dot{x}$, $\dot{y}$, and $\dot{z}$ displacements
$\ddot{\mathbf{x}}$	Cartesian acceleration vector of $\ddot{x}$, $\ddot{y}$, and $\ddot{z}$ displacements
$\mathbf{J}$	Jacobian matrix of manipulator
$\dot{\mathbf{J}}$	Time derivative of Jacobian matrix of manipulator
${}^{j}\mathbf{v}$	Local velocity at frame $\{j\}$
$\boldsymbol{\omega}_i$	Angular velocity of link i
${}^{i}\mathbf{p}_j$	Local position vector of point j as seen from frame i
$\mathbf{v}_i$	Cartesian velocity of the link as seen from joint i

${}^{j}\dot{\mathbf{v}}$	Local acceleration at frame $\{j\}$
$\dot{\boldsymbol{\omega}}_i$	Angular acceleration of link i
$\dot{\mathbf{v}}_i$	Cartesian acceleration of the link as seen from joint i
$\mathbf{f}_d$	Drag
$\mathbf{f}_{am}$	Force due to Added Mass
${}^{j}\mathbf{f}_d$	Drag seen at frame $\{j\}$
C_D	2D dimensionless drag coefficient
d_o	Outer diameter of the cylindrical link
${}^{i}\mathbf{n}_{dj}$	Moment due to the drag at frame $\{j\}$ as seen from frame $\{i\}$
${}^{j}\mathbf{f}_{am}$	Force due to added mass at frame $\{j\}$
${}^{i}\mathbf{n}_{amj}$	Moment due to the force due to added mass $\{j\}$ as seen from frame $\{i\}$
${}^{i}\mathbf{f}_h$	Net Hydrodynamic forces acting on link i as seen from frame $\{i\}$
${}^{i}\mathbf{n}_h$	Net Hydrodynamic moment acting on link i as seen from frame $\{i\}$
${}^{i}\mathbf{n}_i$	Moment vector experienced by joint i
${}^{i}\mathbf{f}_i$	Force vector experienced by joint i
$\dot{\boldsymbol{\omega}}$	Angular velocity vector of link
$\dot{\boldsymbol{\omega}}$	Angular acceleration vector of link
$\dot{\mathbf{v}}$	Acceleration vector of link
$\mathbf{F}$	Inertial force of link
$\mathbf{N}$	Inertial moment of link
$\dot{\mathbf{v}}_\mathbf{c}$	Velocity vector at center of mass of link
$\mathbf{p}_\mathbf{c}$	Position vector of center of mass of link
τ_i	Actuator torque or force sustained by joint i

Chapter 1

Introduction

Autonomous Underwater Vehicles (AUVs) are presenting an ever expanding range of applications that enhance human capabilities and mitigate human risk. The main limitation of these vehicles is endurance. Oceanographers and scientists envision continuous automated surveying of geology and marine life. Navies and governments desire continual surveillance of territory, and autonomous front line capabilities delivered covertly by submarines [19]. The bottleneck in the adoption of these capabilities is a viable autonomous Launch and Recovery (L&R) system [21].

Watt *et al.* [33] discuss three kinds of AUV L&R systems: passive subsurface stationary docks, surface ships, and torpedo tube L&R for military submarines. The majority of existing AUV docking devices use some form of man-in-the-loop control with the exception of autonomous subsurface stationary docks. Present autonomous AUV docking experiments have

yielded marginal success rates, primarily due to limited lateral dexterity of streamlined AUVs. Active control of the dock appears to be necessary for higher success rates.

Defence Research and Development Canada (DRDC) has proposed an innovative project to develop an active automated docking device to be used on slowly moving submarines while maintaining level flight with various AUV designs. The University of New Brunswick (UNB) is collaborating on this multi-year project with the development of a prototype design along with its dynamic model and motion controller for multi-body simulations. This thesis discusses the formulation of a dynamic model and control simulations of a mechanically actuated docking device for which physical prototypes are to be built in the near future.

Related Research

The development of AUVs and AUV supporting systems have been gaining significance for over a decade. The United States of America's Department of the Navy has compiled an AUV master plan [19], outlining the strategic advantage of using, and the primary goals of implementing, an AUV program. The plan depicts the use of AUV fleets with a centralized mission control ship, discussing the importance of AUV support systems and infrastructure. The development of an active autonomous L&R docking device is required to progress the functionality of using AUVs.

The current autonomous docking devices have had marginal success rates, too low to merit the risk of using the AUVs in service. Stokey *et al.* [26] achieved a 62% docking rate using a REMUS 100 AUV and a 1 m diameter stationary funnel dock with acoustic homing. Allen *et al.* [5] obtained a similar docking rate of 60% using an updated version of a similar setup with a rectangular funnel dock. Both trials used varying locations and environmental conditions, and were conducted in conjunction with the Woods Hole Oceanographic Institution. Using electromagnetic homing, Feezor *et al.* [13] achieved successful docking five out of eight attempts. They used a Sea-Grant Odyssey IIB AUV, with a 1 m diameter stationary funnel dock. The trials were preformed over a two week period in environmental conditions with cross currents upwards of 0.3 m/s. They noted that docking typically failed when the AUV initially was misaligned with the dock by more than 30 degrees. Additional similar stationary docking trials have been preformed with various homing and sensing schemes [10, 20, 15] but without presenting docking success rates.

Surface ships typically use human-controlled L&R systems involving cranes or ramp systems [2]. There are surface L&R systems under development using towed bodies [22], and unmanned recovery ribs [1]. These systems' success depends on the sea state [33].

Many countries are interested in an AUV L&R capability for submarines [12, 24, 21, 7]. Fedor [12] discusses optimal AUV docking locations along a submarine. To maximize docking feasibility, Fedor suggests docking

occur in areas with minimal disturbances, *e.g.*, avoiding local turbulence and wakes from obstructions such as the submarine sail. The current submarine docking system under development utilize either tethered remotely operated vehicles (ROVs) [24, 21, 7] or a deployed stationary dock [25] for AUV recovery. The current methods also recover to the submarine's torpedo or missile tubes, disabling their functional use for the submarine.

The majority of these docking devices rely on either the AUV for correctly aligning itself with the dock or man-in-the-loop remote control. As described by the Director of Innovation, of the US Office of Naval Research, AUV recovery must account for the: sea state, operational tempo, autonomy, motion prediction, and AUV maneuvering and control authority to be successful and robust [21]. Seizer [22] notes the absence of ship-board autonomous AUV L&R devices. DRDC suggests that the deficiencies apparent with stationary autonomous docking systems might be corrected using active autonomous docking.

A successful active, autonomous AUV docking device will require a mechanism with the control and dexterity to achieve contact with the AUV in the presence of environmental disturbances. Mechanically actuated manipulators are currently in use with submerged remotely operated devices [3]. These are typically used for precision tasks but on a relatively small size scale. Control of ship board robotic manipulators has been explored by From *et al.* [14]. They augment a PD controller with a real-time wave prediction model to overcome the non-inertial effects of the manipulator base

and optimize joint torques for prescribed trajectories.

There has been significant effort to develop AUV docking systems, all with marginal success rates. The functional use of AUVs is limited by the absence of a robust AUV docking device. An active, autonomous, reliable AUV docking device would allow AUVs to be recovered to naval platforms quickly and accurately. The successful implementation of such a device will require the synthesis of sensing information, robust autonomous control, and an actuated mechanism with sufficient dexterity to overcome relative motion between the AUV and dock imposed by environmental disturbances. This project will contribute to the development of AUV docking by proposing an active autonomous AUV docking solution for submarines.

Chapter 2

Project Overview

2.1 Project Scope

The AUV underwater docking problem is complex. Defence Research and Development Canada (DRDC) states the docking solution should provide for [33]:

- deep water operations,
- littoral operations with minimal sea state limitations,
- automation for reliability and temporal efficiency,
- low risk to the submarine propeller or appendages should something break or let go during docking,
- low risk of AUV/submarine collision in the presence of environmental disturbance,

- a flexible choice of AUV size and shape to maximize endurance and functionality,
- minimal docking infrastructure on the AUV to simplify use of commercial-off-the-shelf vehicles,
- and a fail safe design for emergency maneuvers.

More specifically, it is convenient to consider docking in three primary stages: making physical contact between the AUV and dock, capture, and parking [33]. Achieving precise contact with the AUV has been identified as the most challenging task of this project, largely because the system has complex nonlinear dynamics and if unsuccessful, capture will become infeasible. As a consequence, designing a dock prototype which is capable of achieving precise contact with the AUV has been established as the first stage of the overall project. UNB will provide a proof-of-concept design, including a dynamic model of the prototype and its controller for initial multi-body simulations. DRDC and other collaborators will provide sensing systems, AUV homing trajectories, and expertise to assist in the development of the initial prototype design for dynamic simulation.

2.2 Design Criteria

AUV capture will occur alongside the submarine, heading into the waves, while the submarine is at depth maintaining level flight in littoral waters.

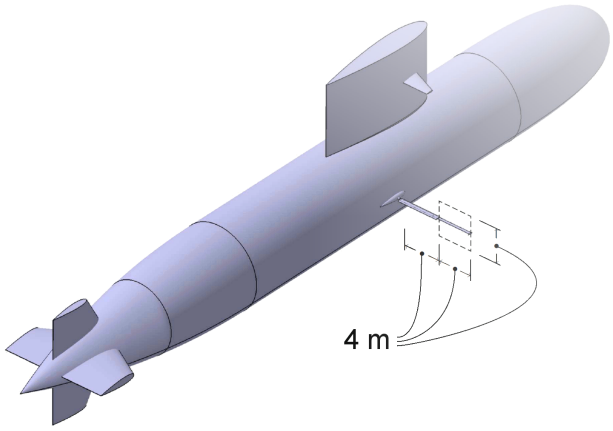

Figure 2.1: Proposed AUV docking envelope, defining the minimum required workspace for the device [32].

All designs must be made fail safe in operation to mitigate the risk to submariners. The most important of the UNB design objectives are:

- The primary objective of the mechanism is to provide transverse trajectory corrections for the AUV during the final stages of achieving contact,
- The submarine will maintain straight and level flight at 2 to 3 knots ($\approx$ 1 to 1.5 m/s),
- Docking will occur from 4 to 8 m off the side of the submarine's hull, at the midpoint of the submarine where the flow is most uniform, as shown in Figure 2.1,
- The dock must achieve precise contact with a point on the AUV; given a tolerance of ± 0.005 m,

- Initially, the orientation of the AUV will be neglected, reducing the task to three degrees of freedom and focusing on accurately contacting a point on the AUV,
- The worst case scenario is defined as docking at 15 m depth in littoral waters in sea state 6 (4 to 6 m high waves),
- The worst case AUV motion is assumed to be the fluid particle motion given by unimodal linear wave theory predictions of sea state 6 waves,
- and the dock design must be fail-safe minimizing risk to submariners.

2.3 Primary Concept Variants

A large number of actuation concepts have been analysed for the docking mechanism. They can be classified as either mechanically actuated or hydrodynamically actuated. Mechanically actuated designs contained more traditional power transformers such as scissor arm linkages, and motor actuated links, as shown in Figure 2.2a. Less conventional concepts such as tensioned spring and cable articulated bodies, and adjustable arrestor cables were also investigated [6, 9]. While, hydrodynamically actuated designs included directed water-jets, actively controlled hydrofoils, as shown in Figure 2.2b, or towed bodies.

Qualitative concept evaluation has been a large task, accounting for input from a wide variety of sources. Fail-safe design considerations, consul-

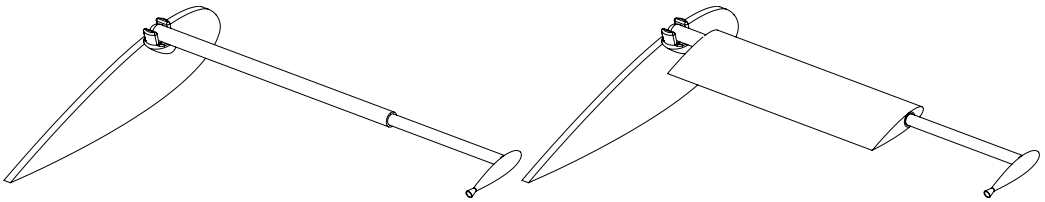

(a) (b)

Figure 2.2: Examples of the two primary autonomous dock concept variants, shown with their faired base. (a) Mechanically actuated 3-DOF arm , and (b) Hydrodynamically actuated wing.

tations with submariners, and proof-of-concept analysis have been the main drivers of the process. These inputs have lead to the avoidance of mechanisms using cables or towed bodies due to the increased risk of fouling the propeller. Eventually the two most promising concept variations have been agreed to be rigidly connected manipulators, which are either mechanically actuated or hydrodynamically actuated mechanisms, as shown in Figure 2.2. A mechanically actuated mechanism will be able to move in the longitudinal plane in addition to the transverse plane. Having each joint actively driven with a motor leads to the potential benefits of having rapid closed-loop response times, relatively simple and robust control algorithm, good disturbance rejection characteristics, and the fact that actuation does not require fluid flow.

Hydrodynamically actuated concepts use the forward motion imparted by the submarine and an actively pitched wing to indirectly provide motive force. This allows the device to move in the transverse plane, relying on the forward motion of the AUV to correct for relative error, in the longitu-

dinal plane, between itself and the submarine. Hydrodynamically actuated devices will derive potential benefits of: low actuation power and noise, inherent streamlining for reduced drag, and passive compliance to compensate for submarine roll.

2.4 Research Objective

The main objective of this research is to contribute to the overall docking project by proposing a mechanically actuated, active, autonomous dock design capable of achieving precise contact with an AUV subject to the given design parameters. The proposed mechanical device will be simulated with a preliminary controller to evaluate the potential performance of the device quantitatively.

The intent of this thesis is to provide DRDC with a thorough understanding of a possible mechanically actuated docking device, identifying any critical issues. The selection of the proposed device over alternate mechanically actuated docking devices will be discussed and justified. This will assist DRDC in their selection of a final docking solution.

2.5 Proposed Mechanically Actuated Mechanism Sub-Variations

The preliminary mechanically actuated sub-variants consist of Cartesian 3DOF serial or parallel mechanisms. Serial mechanisms consist of links and joints connected in a single series from base to end effector. Parallel mechanisms are closed loop structures consisting of multiple series of links and joints sharing one common end effector.

Both serial and parallel mechanisms consist of varying joint types (JT) and joint configurations (JC). Their architecture is commonly described in series of joint pairs, per series of links, with the general form of, JTJCJT. A joint type defines the joint's degrees of freedom and its local motion. While, a joint configuration describes the geometrical relationship between the position of one joint to another adjoining joint, *i.e.*, perpendicular ($\perp$) or parallel ($\parallel$). There are 4 primary joint types, revolute (R), prismatic (P), universal (U), and spherical (S). Revolute joints have 1DOF and rotate about a fixed axis. Prismatic joints have 1DOF and translate linearly along a fixed axis. Universal joints have 2DOF and consist of two revolute joints connected in a perpendicular joint configuration with an intersecting axis of rotation, *i.e.* U$\equiv$R$\perp$R. Spherical joints have 3DOF and consist of three revolute joints with an intersecting axis of rotation and are arranged perpendicularly to one another, *i.e.*, S$\equiv$R$\perp$R$\perp$R.

Initially, a R$\perp$R$\parallel$R robotic serial manipulator, as shown in Figure 2.3,

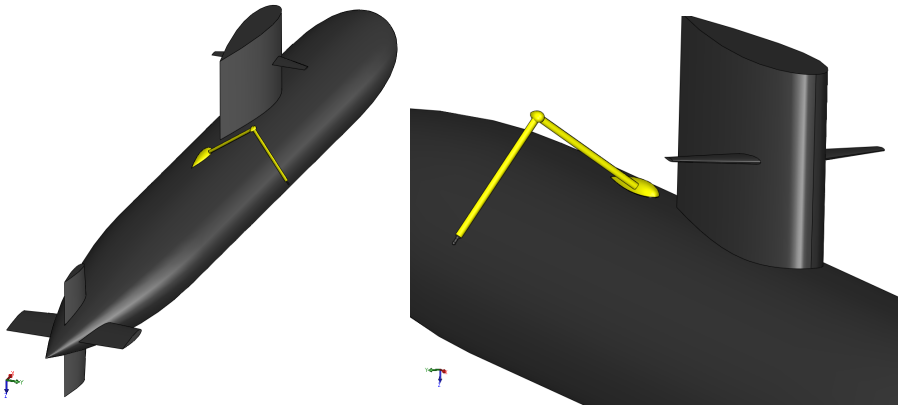

(a) (b)

Figure 2.3: R⊥R||R mechanically actuated concept under consideration.

was proposed [9]. The device has a 2DOF shoulder at its base and a 1DOF elbow along its mid-length.This mechanism is a deck-mounted device and along with its architecture provides a large workspace. The hypothesized benefits of this device include, its ability to dampen the effects of submarine roll on the end effector via its elbow, the ability to be serviced at sea (because it is accessible from the deck), and its potential to complete tasks beyond just AUV contact, such as AUV stowage. This potential design presents some challenges, primarily hydrodynamic drag and vibration from vortex shedding. Thus, actuator torque and power requirements are hypothesized to be unreasonably large and its flexibility may render precise control of the end effector impossible.

A parallel robotic manipulator, as shown in Figure 2.4, was proposed by MacKenzie [33]. The original mechanism was defined as a tripod dock with two drive legs, actuated with lead screws, and constrained with a pas-

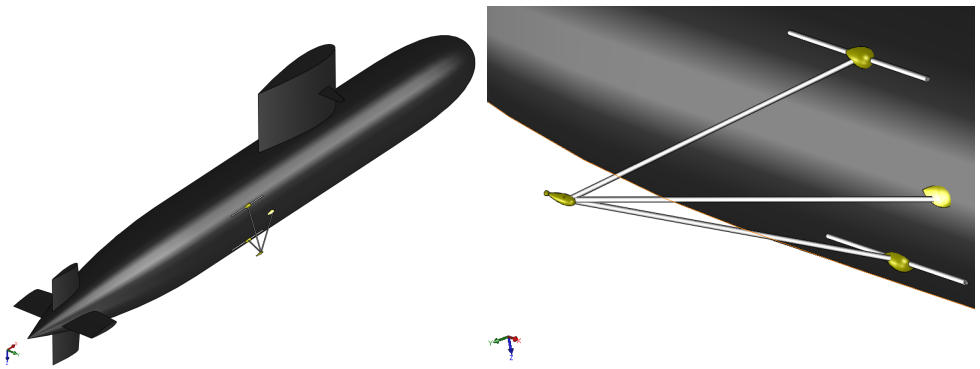

(a) (b)

Figure 2.4: 2$\overline{\text{P}}$UU-SS parallel manipulator concept under consideration.

sive support leg. The original design is expanded to include hypothesized joint architecture. The revised architecture is a 2$\overline{\text{P}}$UU-SS parallel manipulator. Similarly, there are two actuated legs consisting each of an actuated prismatic joint, denoted by $\overline{\text{P}}$, with a link between the $\overline{\text{P}}$ actuator and end effector, connected by two universal joints (U). The mechanism also contains a link connected by two spherical joints (S), between the base and the end effector. This architecture constrains the mechanism to 3DOF, although it is difficult to determine whether the device will produce the required end effector trajectory without further kinematic analysis. Parallel manipulators can maneuver large payloads quickly and accurately. Their closed-loop link architecture often increases the overall rigidity of the mechanism. As a consequence of their multiple links, their footprint and infrastructure are typically large in comparison to their workspace which may increase the effects of hydrodynamic forces.

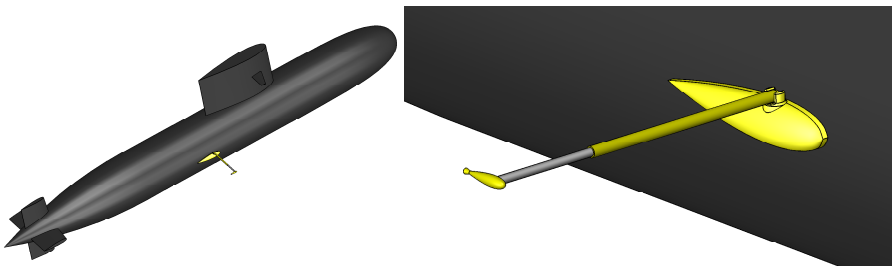

(a) (b)

Figure 2.5: R⊥R⊥P mechanically actuated concept under consideration.

An R⊥R⊥P robotic serial manipulator, as shown in Figure 2.5, is also proposed. This device consists of a 2DOF shoulder at its base, similar to the R⊥R∥R device, and a prismatic translating arm allowing the device to move in the longitudinal plane in addition to the transverse plane. This device is hypothesized to be the optimal mechanically actuated architecture as it contacts the AUV with the minimum required distance from the submarine. This in turn minimizes the device's exposed infrastructure in the onset flow, reducing hydrodynamic effects.

Chapter 3

Establishing a Design Trajectory

A benchmark end effector trajectory is first established based on the docking parameters. The worst case AUV kinematics, relative to the submarine, are assumed to be conservatively represented by those of a fluid particle disturbed by sea state 6 waves at a depth of 15 m in water 30 m deep. Unimodal linear wave theory is used to estimate the kinematics of a fluid particle as an ocean surface wave moves past that particle.

3.1 Linear Wave Theory

The fundamental governing equations describing fluid motion are derived by investigating conservation laws applied to a fluid passing through a fixed fluid element bounded by a control surface. These laws state that mass (m), momentum, and energy must be conserved. To develop the potential flow

problem the laws of conservation of mass and momentum are employed [35]. The conservation of mass states that the net rate of flow of mass into the fluid element equals the rate of increase of mass in the fluid element. The conservation of mass can be reduced to the continuity equation,

$$\frac{\partial \rho}{\partial t} + \nabla \cdot \rho \mathbf{q} = 0 \tag{3.1}$$

where ρ is the fluid density, ∇ is the Cartesian gradient operator, $\mathbf{q}$ is a Cartesian velocity vector of the fluid $\mathbf{q} = [u\ v\ w]^T$. The conservation of momentum states that the rate of increase of momentum of a fluid particle equals the sum of forces on the fluid particle. For a fixed fluid element the conservation of momentum can be reduced to,

$$\rho \frac{D\mathbf{q}}{Dt} = \rho g - \nabla P + \nabla \cdot \tau_{ij} \tag{3.2}$$

where $\frac{D\mathbf{q}}{Dt}$ is the total acceleration of a particle that instantaneously occupies the fluid element, g is gravity, P is pressure, and τ_{ij} is the viscous stress tensor acting on the element.

Hydrodynamics studies of fluid flows with high Reynolds numbers typically find viscous effects are limited to thin boundary layers and thin wake regions near the surface of a submerged body [16]. This allows the majority of analysis to assume the fluid flow is inviscid and incompressible. Inviscid flow neglects viscous effects, *i.e.*, viscosity $= 0$, while incompressible flows state that fluid density is constant and does not vary with time. Katz

and Plotkin [16] show that, the vorticity in the high Reynolds number flow fields being studied is confined to the boundary layer and wake regions where the influence of viscosity is not negligible and so it is appropriate to assume an irrotational as well as inviscid flow outside these confined regions. Therefore, White [35] shows the continuity equation for fluid flows which are inviscid, incompressible, and irrotational becomes,

$$\nabla^2\Phi = \frac{\partial^2\Phi}{\partial x^2} + \frac{\partial^2\Phi}{\partial y^2} + \frac{\partial^2\Phi}{\partial z^2} = 0 \tag{3.3}$$

where Φ is the velocity potential and is defined such that,

$$\mathbf{q} = \nabla\Phi \tag{3.4}$$

Laplace's equation, Eq. (3.3), is a linear differential equation and provides the basis for potential flow problems. The momentum equation, Eq. (3.2), can be reduced to the unsteady Bernoulli equation,

$$\frac{\partial\Phi}{\partial t} + \frac{P}{\rho} + \frac{\|\nabla\Phi\|^2}{2} + gz = Constant \tag{3.5}$$

To derive the particle kinematic equations for a Unimodal Linear Wave, the velocity potential pertaining to the fluid region, as described in Figure 3.1, must be determined. The velocity potential must satisfy Eq. (3.3), that is,

$$\frac{\partial^2\Phi}{\partial x^2} + \frac{\partial^2\Phi}{\partial z^2} = 0 \tag{3.6}$$

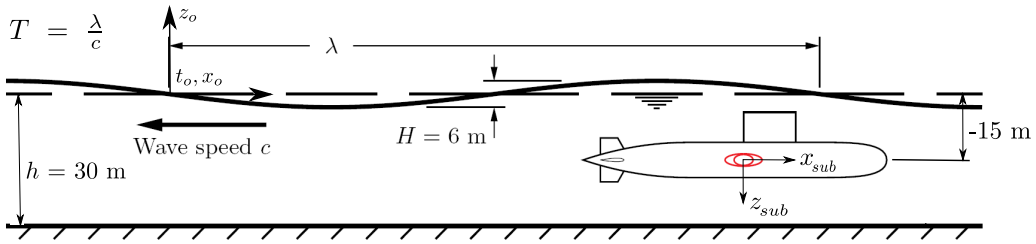

Figure 3.1: Definition sketch of a progressive wave train [23, 34].

The velocity potential will be bounded by the following conditions,

$$\frac{\partial \Phi}{\partial z} = 0 \qquad \text{at} \quad z = -h \tag{3.7}$$

where h is the overall sea depth. This means the vertical particle velocity $\dot{z}$ at the sea bed is equal to zero as the sea floor is fixed. Secondly, the vertical fluid motion has to be equal to the vertical velocity of the free surface.

$$\frac{\partial \eta}{\partial t} = \frac{\partial \Phi}{\partial z} \qquad \text{at} \quad z = \eta(x,t) \tag{3.8}$$

where η is the free surface elevation from the mean surface level $z = 0$ at position x and time t as the wave train moves past.

The dynamic free surface boundary condition is derived from the unsteady Bernoulli equation assuming the pressure at the free surface is constant and neglecting the second order quantity $\frac{\|\nabla\Phi\|^2}{2}$

$$\eta = \frac{-1}{g}\frac{\partial \Phi}{\partial t} \tag{3.9}$$

where g is the acceleration of gravity. The velocity potential can then be solved, and is described by,

$$\Phi = \frac{\pi H}{kT} \frac{\cosh(k(h+z))}{\sinh(kh)} \sin\left(kx - \frac{2\pi t}{T}\right) \tag{3.10}$$

where H is the wave height, k is the wave number, T is the wave period, and z is the mean depth of the wave particle. For a wave of a given period, propagating in an ocean of constant depth, k is determined using the linear dispersion relation,

$$kg \tanh(kh) = \left(\frac{2\pi}{T}\right)^2 \tag{3.11}$$

which relates k and T due to the free surface boundary condition. The corresponding horizontal particle velocity $\dot{x}$ can be derived as,

$$\dot{x} = \frac{\partial \Phi}{\partial x} = \frac{\pi H}{T} \frac{\cosh(k(h+z))}{\sinh(kh)} \cos\left(kx - \frac{2\pi t}{T}\right) \tag{3.12}$$

Likewise, the vertical particle velocity is defined as,

$$\dot{z} = \frac{-\partial \Phi}{\partial z} = \frac{\pi H}{T} \frac{\sinh(k(h+z))}{\sinh(kh)} \sin\left(kx - \frac{2\pi t}{T}\right) \tag{3.13}$$

The particle displacement and local acceleration can then be integrated and derived respectively.

It should be noted that although linear wave theory has its assumptions, the results provide a foundation for defining an AUV's trajectory. The

Table 3.1: Parameters for linear wave theory model.

NATO Sea State	6
Maximum Wave Height H (m)	6
T_{min}(sec)	10.5
T_{avg}(sec)	13.8
T_{max}(sec)	17.5
Sea depth h (m)	30
Particle depth z (m)	-15

behaviour is assumed to be unimodal, having a single frequency wave system. Observations show true wave behaviour is more complex where 59% of seas are multi-modal and nearly 45% of all observed wave are multi-directional [8]. Multi-modal waves have at least two distinct frequencies, potentially more, and can be unidirectional or multi-directional. These real effects must be considered in the overall docking process but this research will assume linear wave theory is sufficient to define the workspace and kinematic extremities the active dock may have to track without lose of generality.

3.2 AUV Motion Bounds

The specific variables used to define the particle trajectory are summarized in Table 3.1. The wave height and wave periods are determined from statistical data for operation in sea state 6 [8, 18]. While the operating conditions are defined in the design criteria. The AUV's kinematics can be evaluated during one phase of the passing of the wave train. The particle is assumed

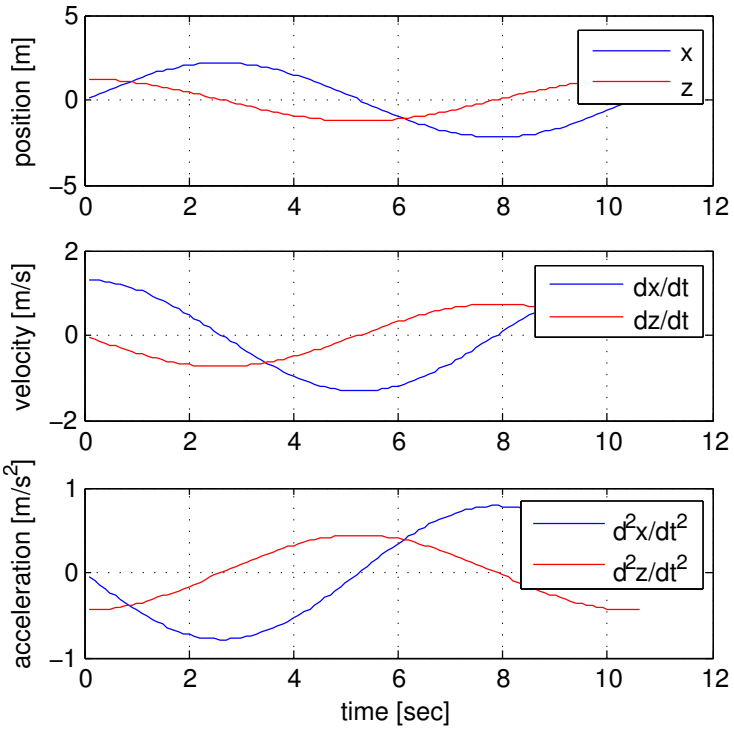

Figure 3.2: Fluid particle horizontal and vertical displacement, velocity, and acceleration amplitudes given a minimum wave period of $T_{min} = 10.5$ seconds.

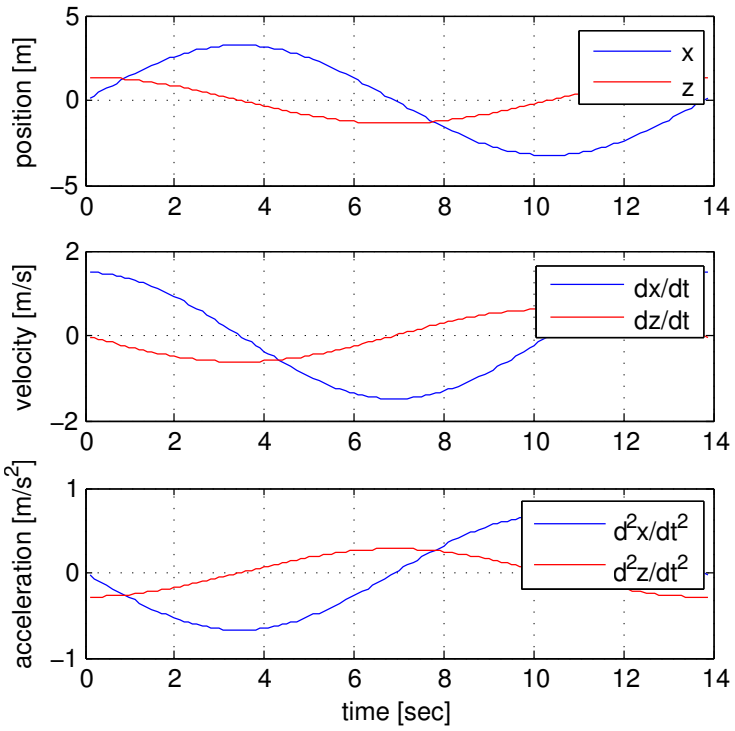

Figure 3.3: Fluid particle horizontal and vertical displacement, velocity, and acceleration amplitudes given an average wave period of $T_{avg} = 13.8$ seconds.

to be at position $x = 0$ relative to the wave train and its kinematics are described as a function of time. The results are described in an inertial frame and plotted in Figures 3.2-3.4, respectively.

3.3 Summary of AUV Design Trajectory

Conservatively assuming the submarine to be unaffected by the waves and the AUV motion is defined by the moition of a fluid particles induced by a passing wave, Unimodal Linear Wave Theory provides a benchmark end ef-

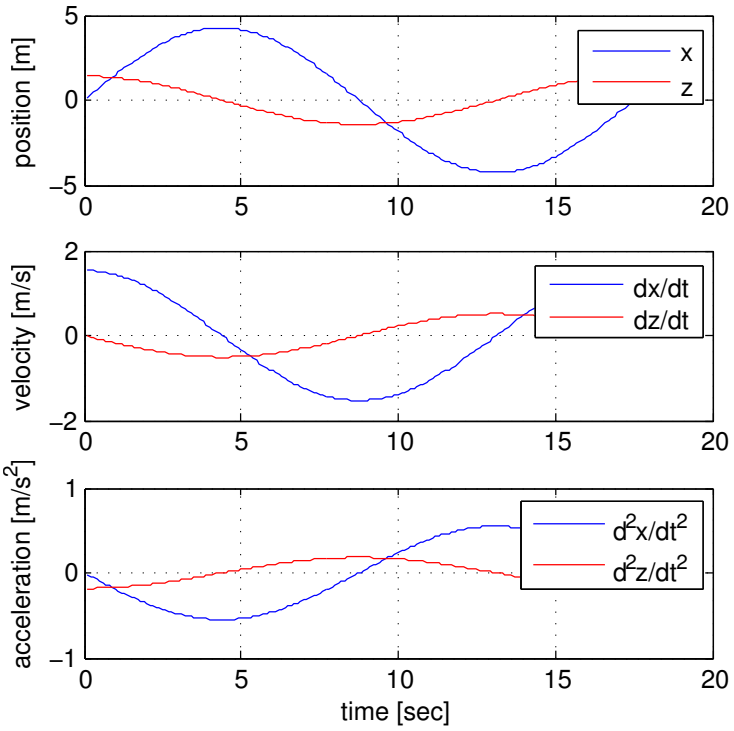

Figure 3.4: Fluid particle horizontal and vertical displacement, velocity, and acceleration amplitudes given a maximum wave period $T_{max} = 17.5$ seconds.

fector trajectory for the relative kinematics between the AUV and submarine. The results show that the relative motion between the submarine and the AUV can be significant. Maximum displacements can exceed $\pm$ 4 m within a 17 s wave period, while both the velocity and acceleration also have large amplitudes. It should be clarified that the docking device must be capable of achieving these trajectories, the device will not necessarily track this trajectory completely under real operation but must be capable of responding to these bounds.

Chapter 4

Dynamic Model Development

The dynamic equations of a manipulator allow the joint torques or joint forces (τ_i) to be calculated depending on joint type. Two common approaches are used when solving serial manipulator dynamics: Lagrangian, which is an energy based method, and Newton-Euler, which is a closed form method. The Newton-Euler method will be used.

The recursive Newton-Euler formulation analyzes a link uniquely and propagates the effects acting on each link to the others to develop a dynamic model for the overall mechanism. This differs from analyzing the mechanism as one whole body, which is the more common method used in hydrodynamic analysis. The advantage being, the recursive technique maintains constant moment of inertia tensors for each link. The method also allows direct observation of multiple dynamic variables of the mechanism.

4.1 General Derivation of Distributed Hydrodynamic Forces

The primary hydrodynamic forces to consider in a bluffed submerged mechanically actuated mechanism are drag ($\mathbf{f}_d$), the force due to added mass ($\mathbf{f}_{am}$), and the Froude-Krylov force ($\mathbf{f}_{FK}$) [27]. In general, bodies which are symmetric about local onset velocity $\mathbf{q}$, can only produce lift under special circumstances not considered here. This means that under expected operating conditions the cylindrical links in Figure 2.5 will produce drag, but not lift. These forces are evaluated using the Morison equation and applying strip theory by assuming the links are slender. That is, if a member is significantly longer than its own cross section; localized 2D section forces can be integrated over the length (L) of the member to obtain the net force.

4.1.1 Morison Equation for Slender Bodies

The Morison Equation, originally presented by Morison, O'Brien, Johnson, and Schaaf in 1950, is a semi-empirical equation which approximates the normal force per unit length acting on a body in oscillatory flow [23, 27, 29]. The Morison equation accounts for both the effects of the body moving through quiescent water as well as the effects of waves if present. To develop the equation we must first derive its components. It is convenient to develop the Morison equation in scalar form, which is equivalent to determining the total in-line normal force acting collinear to the onset flow vector. The application

of the Morison equation in three-dimensional vector form is discussed in the preceding section.

Drag is the force component parallel to the relative velocity of the moving fluid and it is proportional to the body's projected area in the flow. Drag consist of the force due to pressure on the cylinder as the flow passes around it and the force due to friction between the fluid and the cylinder. The magnitude of drag due to pressure (f_{dP}) per unit length of the cylinder can be described as,

$$\mathrm{f}_{dP} = \int_0^{2\pi} \frac{1}{2} P \cos\phi d_o \, d\phi \tag{4.1}$$

where P is pressure, ϕ is the angular position, and d_o is outer diameter of the cylinder. The magnitude of drag due friction (f_{dF}) per unit length of the cylinder can be described as,

$$\mathrm{f}_{dF} = \int_0^{2\pi} \frac{1}{2} \tau_o \sin\phi d_o \, d\phi \tag{4.2}$$

where τ_o is the wall shear stress on the cylinder surface. The total drag magnitude can be obtained by summing Eq. (4.1) and Eq. (4.2),

$$\mathrm{f}_d = \int_0^{2\pi} \frac{1}{2} d_o \left(P \cos\phi + \tau_o \sin\phi\right) d\phi \tag{4.3}$$

Eq. (4.3) can be rewritten in non-dimensional form, as described by Sumer [27],

and is given by,

$$\frac{\mathrm{f}_d}{\frac{1}{2}\rho d_o \|\mathbf{q}\|^2} = \int_0^{2\pi} \left(\frac{P - P_o}{\rho \|\mathbf{q}\|^2} \cos\phi + \frac{\tau_o}{\rho \|\mathbf{q}\|^2} \sin\phi \right) d\phi \tag{4.4}$$

where P_o is the hydrostatic pressure. The right-hand-side of Eq. (4.4) is more commonly denoted as C_D the 2D dimensionless drag coefficient. In general, C_D is a function of the Reynolds number defined as,

$$Re = \frac{\|\mathbf{q}\| d_o}{\upsilon} \tag{4.5}$$

where υ is the kinematic viscosity. Typically C_D is determined from accepted experimental data. This allows the drag component of the Morison equation to be defined as,

$$\mathbf{f}_d = \frac{1}{2} C_D \rho d_o \, \mathbf{q} \| \, \mathbf{q} \, \| \tag{4.6}$$

Note the $\|\mathbf{q}\|^2$ term is rewritten as $\mathbf{q}\|\mathbf{q}\|$ to maintain the sign of the velocity ensuring the force is in the direction of the onset velocity.

Added mass is the added inertia the link must overcome when accelerating; it represents the inertia of fluid being accelerated as the link accelerates. That is, as mass is the proportionality constant between the kinetic energy of a link and the square of its velocity, added mass is the proportionality constant between the kinetic energy of the fluid surrounding a link and the square of that link's velocity [30].

To calculate the force due to added mass the pressure on the surface

of the cylinder is integrated. The pressure is determined from the flow field around the body due to the pressure gradient created when accelerating the body in still water. The disturbance velocity potential of the fluid in the immediate region of the cylinder with forward velocity q is determined in polar coordinates and is given by Milne-Thomson via Sumer [27],

$$\Phi = \|\mathbf{q}\| \left(\frac{{d_o}^2}{4r}\right) \cos\phi \tag{4.7}$$

The speed of the fluid on the surface of the cylinder (v) at $r = \frac{d_o}{2}$ can be calculated by deriving both the radial and angular velocity components,

$$\mathrm{v}_\theta = -\frac{1}{r}\frac{\partial \Phi}{\partial \phi} = \|\mathbf{q}\| \sin\phi \tag{4.8}$$

$$\mathrm{v}_r = -\frac{\partial \Phi}{\partial r} = \|\mathbf{q}\| \cos\phi \tag{4.9}$$

$$\mathrm{v}^2 = {\mathrm{v}_\theta}^2 + {\mathrm{v}_\theta}^2 = \|\mathbf{q}\|^2 \left(\cos^2\phi + \sin^2\phi\right) \tag{4.10}$$

The pressure around the cylinder can be calculated using the unsteady Bernoulli equation as follows,

$$\frac{P}{\rho} + \frac{\mathrm{v}^2}{2} - \frac{\partial \Phi}{\partial t} = constant \tag{4.11}$$

where as shown in Eq. (4.10), $\frac{\mathrm{v}^2}{2}$ is constant. Eq. (4.11) can be rearranged to give the pressure on the cylinder surface as,

$$P = \rho \frac{\partial}{\partial t}\left(\frac{1}{2} d_o \cos\phi \, \|\mathbf{q}\|\right) + constant \tag{4.12}$$

where the constant includes $\frac{v^2}{2}$ and will not contribute to the resulting force. Therefore the force due to added mass for a cylinder per unit length can be described as,

$$\mathbf{f}_{am} = \int_0^{2\pi} \frac{1}{4}\rho {d_o}^2 \dot{\mathbf{q}} \cos^2\phi \, d\phi \tag{4.13}$$

$$= \frac{\pi}{4}\rho {d_o}^2 \dot{\mathbf{q}} \tag{4.14}$$

The Froude-Krylov force occurs only when the fluid in which the body is submerged is in motion, *i.e.* waves. This force is due to the pressure gradient generated by the accelerating fluid in the outer-flow region, and can be shown by,

$$\frac{\partial P}{\partial x} = -\rho \frac{d\|\mathbf{U}\|}{dt} \tag{4.15}$$

where $\mathbf{U}$ is the fluid velocity far from the cylinder. As shown in Sumer [27], the Froude-Krylov force can be calculated from integrating the pressure on the surface of the cylinder using the surface integral,

$$\mathbf{f}_{FK} = -\int_S P \cdot \hat{\mathbf{n}} \, d\mathbf{S} \tag{4.16}$$

where $\mathbf{S}$ is the cylinder surface, and $\hat{\mathbf{n}}$ is the unit vector normal to the surface $\mathbf{S}$. Applying the Gauss theorem the Froude-Krylov force for a cylinder can be written as,

$$\mathbf{f}_{FK} = \rho V \frac{d\mathbf{U}}{dt} \tag{4.17}$$

where V is the volume of the body. Eq. (4.17) can be rewritten as the Froude-Krylov force per unit length given by,

$$\mathbf{f}_{FK} = \frac{\pi}{4}\rho {d_o}^2 \dot{\mathbf{U}} \tag{4.18}$$

Combining Eq. (4.6), Eq. (4.14), and Eq. (4.18) the Morison equation can be defined as,

$$\mathbf{f}_h = \frac{1}{2} C_D \rho d_o \, \mathbf{q} \parallel \mathbf{q} \parallel + \frac{\pi}{4}\rho {d_o}^2 \dot{\mathbf{q}} + \frac{\pi}{4}\rho {d_o}^2 \dot{\mathbf{U}} \tag{4.19}$$

which in this form can be applied using strip theory to evaluate the total hydrodynamic force $\mathbf{f}_h$ acting on the cylinder. Note that in Eq. 4.19, $\mathbf{q}$ is relative velocity of the fluid to the cylinder, while $\mathbf{U}$ is the velocity of solely the fluid induced by the waves.

4.1.2 Application of Morison Equation to Manipulator Dynamics

Joint frames $\{i\}$ and $\{i+1\}$ are assigned to the link, as shown in Figure 4.1. A local frame $\{j\}$ is located at point j and oriented identical to frame $\{i\}$. The local velocity ${}^j\mathbf{v}$ is described by,

$${}^j\mathbf{v} = \boldsymbol{\omega}_i \times {}^i\mathbf{p}_j + \mathbf{v}_i + {}^j_k\mathbf{R}\, {}^k\mathbf{U} \tag{4.20}$$

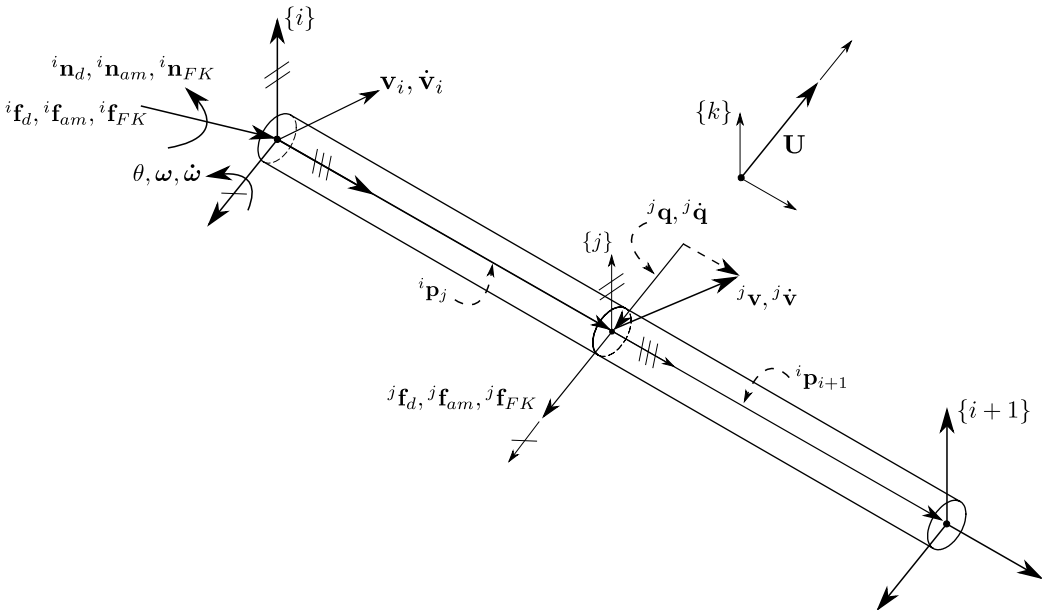

Figure 4.1: General free body diagram depicting pertinent variables for derivation of distributed Hydrodynamic forces.

where $\boldsymbol{\omega}_i$ is the angular velocity of link i, ${}^i\mathbf{p}_j$ is the local position vector of point j as seen from frame i, $\mathbf{v}_i$ is the Cartesian velocity of the link as seen from joint i, here the 3×3 rotation matrix ${}^j_k\mathbf{R}$ gives the orientation of frame j as seen from joint k, and ${}^k\mathbf{U}$ is the velocity of the fluid as seen in the frame k. The local acceleration ${}^j\dot{\mathbf{v}}$ is defined as,

$$ {}^j\dot{\mathbf{v}} = \dot{\boldsymbol{\omega}}_i \times {}^i\mathbf{p}_j + {}^i\boldsymbol{\omega}_i \times \left({}^i\boldsymbol{\omega}_i \times {}^i\mathbf{p}_j \right) + \dot{\mathbf{v}}_i + {}^j_k\mathbf{R}\, {}^k\dot{\mathbf{U}} \tag{4.21} $$

where $\dot{\boldsymbol{\omega}}_i$ is the angular acceleration of link i, $\dot{\mathbf{v}}_i$ is the Cartesian acceleration of the link as seen from joint i, and ${}^k\dot{\mathbf{U}}$ is the acceleration of the fluid as seen in the frame k.

Two dimensional strip theory is used to model the hydrodynamic forces on each link. For this analysis, it is assumed the hydrodynamic forces on the link can be determined by analyzing the flow at each cross-section in 2D planes normal to the longitudinal axis and summed over the entire link to estimate the total hydrodynamic force. When applying this method the axial component of the onset flow is ignored and the local onset velocity in the 2D cross-section plane is defined as,

$$ {}^{j}\mathbf{q} = -\left({}^{j}\mathbf{v} - \left(\frac{{}^{j}\mathbf{v} \cdot {}^{i}\mathbf{p}_j}{\|{}^{i}\mathbf{p}_j\|^2} \right) {}^{i}\mathbf{p}_j \right) \tag{4.22} $$

and local onset acceleration $\dot{\mathbf{q}}$ in the 2D cross-sectional plane can be expressed as,

$$ {}^{j}\dot{\mathbf{q}} = -\left({}^{j}\dot{\mathbf{v}} - \left(\frac{{}^{j}\dot{\mathbf{v}} \cdot {}^{i}\mathbf{p}_j}{\|{}^{i}\mathbf{p}_j\|^2} \right) {}^{i}\mathbf{p}_j \right) \tag{4.23} $$

where ${}^{j}\mathbf{q}$ is only the component perpendicular to the link member of the local velocity at point j in coordinates of frame $\{j\}$, and ${}^{j}\dot{\mathbf{q}}$ is the component perpendicular to the link member of the local acceleration at point j in coordinates of frame $\{j\}$.

Using this approach the local drag force in each cross-sectional plane ${}^{j}\mathbf{f}_d$ is defined as,

$$ {}^{j}\mathbf{f}_d = \left(\frac{1}{2} C_D d_o \rho \|{}^{j}\mathbf{q}\|^2 \, dL \right) {}^{j}\hat{\mathbf{q}} \tag{4.24} $$

where d_o is outer diameter of the link corresponding to the reference length for this specific body, dL is the elemental length of the discretized section

at point j, and ${}^{j}\hat{\mathbf{q}}$ is the unit vector of the normal onset velocity. The local moment due to drag (${}^{i}\mathbf{n}_{dj}$) is simply evaluated using the cross product,

$$ {}^{i}\mathbf{n}_{dj} = {}^{i}\mathbf{p}_{j} \times {}^{j}\mathbf{f}_{d} \tag{4.25} $$

Similarly, the force due to added mass (${}^{j}\mathbf{f}_{am}$) in each cross-sectional plane is quantified as,

$$ {}^{j}\mathbf{f}_{am} = \left(\rho \frac{\pi}{4} {d_o}^2 \| {}^{j}\dot{\mathbf{q}} \| \, dL\right) {}^{j}\hat{\mathbf{q}} \tag{4.26} $$

The moment due to the local force due to added mass (${}^{i}\mathbf{n}_{amj}$) can be described as,

$$ {}^{i}\mathbf{n}_{amj} = {}^{i}\mathbf{p}_{j} \times {}^{j}\mathbf{f}_{am} \tag{4.27} $$

Finally, the Froude-Krylov force in each cross-sectional plane is determined using Eq. (4.18) and the fluid particle acceleration which is obtained using linear wave theory presented in Chapter 3. The local Froude-Krylov force in each cross-sectional plane (${}^{j}\mathbf{f}_{FK}$) is defined as,

$$ {}^{j}\mathbf{f}_{FK} = \left(\frac{\pi}{4} \rho {d_o}^2 \| \dot{\mathbf{U}} \|\right) \hat{\dot{\mathbf{U}}} \tag{4.28} $$

where the moment due to the local Froude-Krylov force (${}^{i}\mathbf{n}_{FKj}$) is given by,

$$ {}^{i}\mathbf{n}_{FKj} = {}^{i}\mathbf{p}_{j} \times {}^{j}\mathbf{f}_{FK} \tag{4.29} $$

Since all of the hydrodynamic effects of interest are superposable vector quantities, they can be represented as single equivalent force-moment couples,

$$ {}^{i}\mathbf{f}_h = \sum_{j=0}^{L} {}^{j}\mathbf{f}_d + \sum_{j=0}^{L} {}^{j}\mathbf{f}_{am} + \sum_{j=0}^{L} {}^{j}\mathbf{f}_{FK} \tag{4.30a} $$

$$ {}^{i}\mathbf{n}_h = \sum_{j=0}^{L} {}^{i}\mathbf{n}_{dj} + \sum_{j=0}^{L} {}^{i}\mathbf{n}_{amj} + \sum_{j=0}^{L} {}^{j}\mathbf{n}_{FK} \tag{4.30b} $$

where ${}^{i}\mathbf{f}_h$ is the net hydrodynamic force as seen from the joint frame $\{i\}$ acting on link i, and ${}^{i}\mathbf{n}_h$ is the net hydrodynamic moment acting on the entire link as seen from the joint frame $\{i\}$ acting on link i.

4.2 2D Planar Dynamic Model Development of a Submerged Rigid Cylinder in General Plane Motion in Quiescent Water

A Planar 2DOF dynamic model of a submerged rigid cylindrical link operating in still sea water is investigated. Therefore, drag and the force due to added mass will be present but not the Froude-Krylov force. The link's motion is constrained to planar translation and rotation about a fixed axis, defining general plane motion. The free body diagram of the submerged link is depicted in Figure 4.2, defining the 2D problem.

The link is assumed to be neutrally buoyant, having uniform geometry

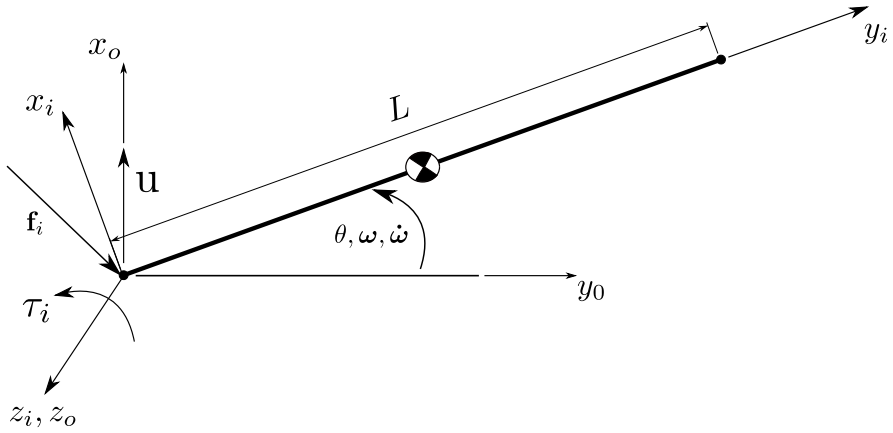

Figure 4.2: Definition of generic link i translating and rotating in general plane motion.

and density. The hypothesized geometry of the device was determined qualitatively from the design criteria in Section 2.2. The link length is defined by the maximum distance to the outer bound of the proposed workspace resulting in an overall length of L=8 m. To determine the link diameter the effect of link diameter on the 2D dimensionless drag coefficient was investigated. Using the Reynolds number, Eq. (4.5), and experimental data relating the 2D dimensionless drag coefficient and Reynolds number for cylinders in cross flow, shown in Figure 4.3, a range of potential diameters where the drag coefficient remained constant could be determined. Outer link diameters ranging between d_o=0.15 m to d_o=0.50 m resulted in a constant 2D dimensionless drag coefficient of C_D=1.2. Knowing the hydrodynamic forces increase with larger diameters the smaller diameter of d_o=0.15 m is preferred. As the selection of the hypothesized link diameter is somewhat arbitrarily chosen the preferred minimum link diameter is doubled to provide a more conser-

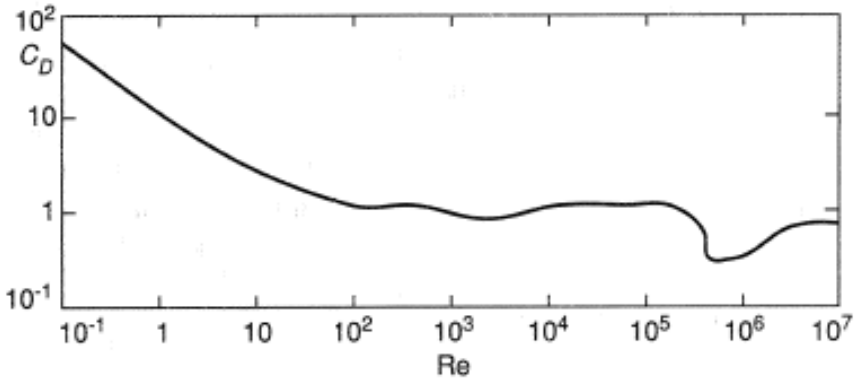

Figure 4.3: Experimental data relating the 2D dimensionless drag coefficient and Reynolds number for cylinders in cross flow [27].

vative evaluation of the dynamic model. Therefore, for simulation purposes a link diameter of d_o=0.30 m is selected. Qualitatively, the outer link diameter must be large enough to accommodate internal components (such as cabling) which may run through the device as well as allowing for sufficient wall thickness to sustain bending moments during operation. It is possible the diameter could be reduced to improve streamlining, however, further modelling of the flexibility of the joints and links is required. It should be noted that these geometric parameters solely provide a basis to evaluate the design concept. Due to neutral buoyancy, the gravitational effects can be neglected and an ideal mass of the link is determined as the equivalent mass of water which the link displaces. The real device will need to be balanced to produce near neutral buoyancy. Regardless whether the device will be neutrally buoyant, a controller and sufficiently sized actuators will be required to drive the system.

The Planar 2DOF dynamic model can be simplified to a system of equations representing the summation of forces,

$$\mathbf{f}_i - {}^i\mathbf{f}_h = m\dot{\mathbf{v}}_c = \mathbf{f}_i - (\mathbf{f}_d + \mathbf{f}_{am}) \tag{4.31}$$

where $\mathbf{f}_d$ and $\mathbf{f}_{am}$ are derived from Eq. 4.30a respectively, $\dot{\mathbf{v}}_c$ is the velocity of the body, and the summation of moments,

$$\tau_i - (\mathbf{n}_d + \mathbf{n}_{am}) = I\ddot{\theta} \tag{4.32}$$

where τ_i is the joint torque acting at frame i, $\mathbf{n}_d$ and $\mathbf{n}_{am}$ are derived from Eq. 4.30b, and I is the mass moment of inertia of the cylinder. The model can now be developed using the concepts presented in Section 4.1. Not the inertial force is identical to the force due to added mass in this case because the links are neturally bouyant cylinders.

4.2.1 Analytical Verification of Planar 2DOF Dynamic Model in Quiescent Water

The model can be decoupled into its components and verified analytically using 2D strip theory. Three verification tests are presented:

- the link moves in pure translation, extended perpendicular to the onset flow, with a forward velocity $\mathbf{u} = [1, 0]^T$ m/s,
- the link rotates about a fixed position, with a constant angular velocity

$\dot{\theta} = 0.1$ rad/s,

- and the manipulator rotates about a fixed position, with a constant angular acceleration $\ddot{\theta} = 0.001$ rad/s^2.

Verification tests one and two verify the linear and rotational portions of Eq. (4.22) respectively as well as verifying both Eq. (4.24) and Eq. (4.25). While the third case verifies the rotational portion of Eq. (4.23) respectively as well as verifying both Eq. (4.26) and Eq. (4.27).

To validate the first test case, a specific equation for drag is derived using 2D strip theory,

$$\mathrm{f}_d = \frac{1}{2} C_D d_o \rho \int_0^L (\mathrm{u})^2 dy \tag{4.33}$$

where $C_d = 1.2$ for cylindrical cross section. Because the member is not accelerating the force due to added mass is zero as shown by Eq. 4.26. The inertial effects due to the mass of the link are not present as the link is in pure translation having no rotation. The joint torque τ_i simply becomes,

$$\tau_i = \frac{1}{2} C_D d_o \rho \int_0^L y(\mathrm{u})^2 dy \tag{4.34}$$

The analytical results for test case one are shown in Table 4.1. The 2D dynamic model results, as shown in Figure 4.4, are verified by the analytical results. The simulation shows added mass and inertial effects do not contribute to the required joint torque in constant translation. This verifies the

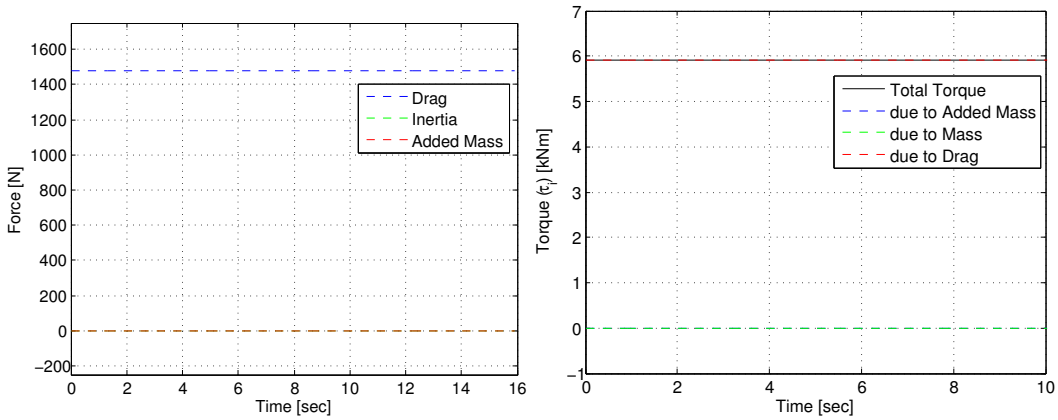

(a) (b)

Figure 4.4: Resultant (a) force and (b) torque from 2D General Plane Motion dynamic model, for submerged cylindrical link in pure translation (*Test Case 1*).

$\mathbf{n}_d$ [kNm]	$\mathbf{n}_{am}$ [kNm]	$I\ddot{\theta}$ [kNm]	τ_i [kNm]	$\mathbf{f_d}$ [N]	$\mathbf{f_{am}}$ [N]
5.90	0	0	5.90	1477	0

Table 4.1: Analytical results for *Test Case 1*, where linear velocity $\mathbf{u}=[1,0,0]^T$ m/s, angular velocity $\dot{\theta}=0$ rad/s, and angular acceleration $\ddot{\theta}=0$ rad/s^2.

translational component of the 2D general plane motion dynamic model.

The analytical equations for the second test case is similar to those of the first where u is replaced by,

$$\mathrm{u} = \dot{\theta} y \tag{4.35}$$

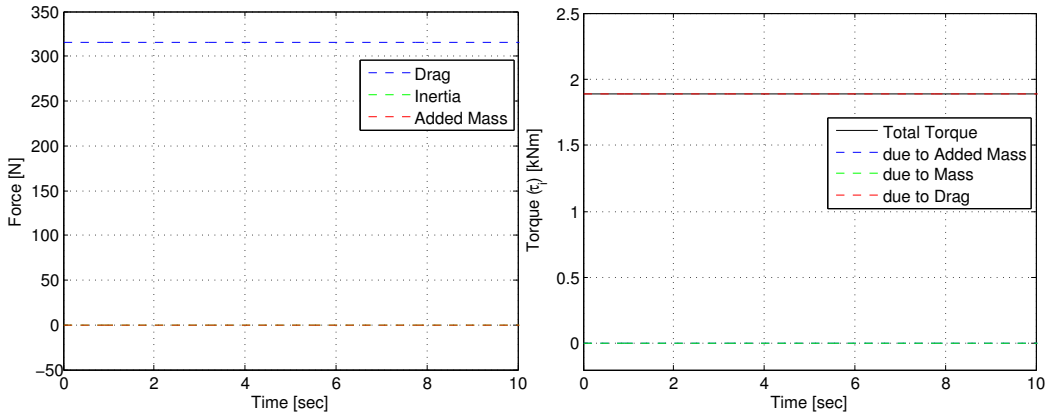

(a) (b)

Figure 4.5: Resultant (a) force and (b) torque from 2D General Plane Motion dynamic model, for submerged cylindrical link in fixed rotation with constant angular velocity (*Test Case 2*).

Again, added mass and inertia effects are not present as the link is rotating at a constant angular velocity. Therefore, drag can be expressed as

$$\mathbf{f}_d = \frac{1}{2} C_D d_o \rho \int_0^L (\dot{\theta} y)^2 dy \tag{4.36}$$

and torque can be expressed as,

$$\tau_i = \frac{1}{2} C_D d_o \rho \int_0^L y(\dot{\theta} y)^2 dy \tag{4.37}$$

It is important to note that the length of the overall device should be minimized to reduce hydrodynamic loads on the structure. The analytical results for test case two are shown in Table 4.2. The 2D dynamic model results, as shown in Figure 4.5, are verified by the analytical results. Like test case one,

$\mathbf{n}_d$ [kNm]	$\mathbf{n}_{am}$ [kNm]	$I\ddot{\theta}$ [kNm]	τ_i [kNm]	$\mathbf{f_d}$ [N]	$\mathbf{f_{am}}$ [N]
1.89	0	0	1.89	315.18	0

Table 4.2: Analytical results for *Test Case 2*, where linear velocity $\mathbf{u}=[0,0,0]^T$ m/s, angular velocity $\dot{\theta}=0.1$ rad/s, and angular acceleration $\ddot{\theta}=0$ rad/s^2.

the simulation shows added mass and inertial effects do not contribute to the required joint torque when rotating at a constant angular velocity about a fixed axis. This verifies the drag component of the 2D general plane motion dynamic model due to rotation.

The analytical equations for the third case are derived similarly to test case two. The analytical drag equation and torque due to drag are identical to those of test case two, Eq. 4.36. and Eq. 4.37 respectively. The analytical equation for the force due to added mass can be defined as,

$$\mathrm{f}_{\mathbf{am}} = \rho\frac{\pi}{4}{d_o}^2\int_0^L(\ddot{\theta}y)dy \tag{4.38}$$

The torque due to added mass and the inertia of the link are present with angular acceleration. Therefore, the torque required at the joint can be defined as,

$$\tau_i = I\ddot{\theta} + \left(\frac{1}{2}C_D d_o\rho\int_0^L y(\dot{\theta}y)^2dy + \rho\frac{\pi}{4}{d_o}^2\int_0^L y(\ddot{\theta}y)dy\right) \tag{4.39}$$

$\mathbf{n}_d$ [Nm]	$\mathbf{n}_{am}$ [Nm]	$I\ddot{\theta}$ [Nm]	τ_i [kNm]	$\mathbf{f_d}$ [N]	$\mathbf{f_{am}}$ [N]
varies	12.37	12.37	*varies*	*varies*	2.32

Table 4.3: Analytical results for *Test Case 3*, where linear velocity $\mathbf{u}=[0,0,0]^T$ m/s, angular velocity $\dot{\theta}$ is numerically integrated, and angular acceleration $\ddot{\theta}$=0.001 rad/s^2.

Similar to drag, the torque required to overcome added mass increases with length, supporting the suggestion overall length of the device should be minimized. The analytical results for test case three are shown in Table 4.3. The 2D dynamic model results, as shown in Figure 4.6, correlate to the expected values. The simulation shows added mass and inertial effects remain constant with $\ddot{\theta}$. While drag increases with the square of $\dot{\theta}$. This verifies the acceleration based components of the 2D general plane motion dynamic model.

4.2.2 Planar 2DOF Dynamic Model Evaluation for Horizontal and Vertical Kinematics of the Design Trajectory in Quiescent Water

The design trajectories established in Chapter 3, shown in Figures 3.2 to 3.4, are resolved into angular coordinates in terms of θ_x , for its horizontal x-axis particle kinematics, and θ_z, for its vertical z-axis particle kinematics, corresponding to the AUV motion in each perspective plane. A forward velocity of $\mathbf{u}=[1,0,0]^T$ m/s is added to the horizontal model evaluation which

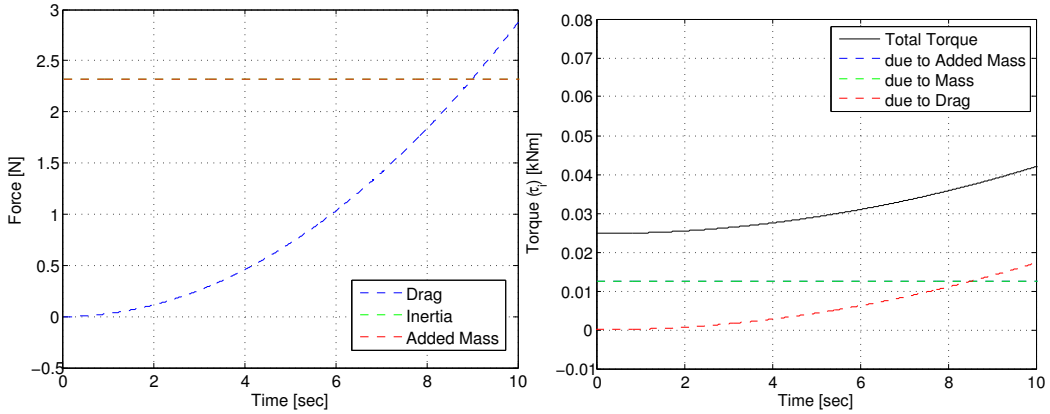

(a) (b)

Figure 4.6: Resultant (a) force and (b) torque from 2D General Plane Motion dynamic model, for submerged cylindrical link in fixed rotation with constant angular acceleration (*Test Case 3*).

is equivalent to the forward motion of the submarine. The estimated required torque for each planar motion is plotted in Figures 4.7 through 4.9.

4.2.3 Summary of 2D Planar Dynamic Model Evaluations of the Design Trajectory

The torque requirements of the mechanically actuated dock device are significant. The primary contributor to the large torque requirements for the device is due to the drag which the bluff submerged body must overcome. The estimated loads of the device suggests the mechanism must be well streamlined in order to be a feasible design.

A well streamlined body can potentially reduce the drag experienced by a bluff body with same frontal area by up to 10 times its original mag-

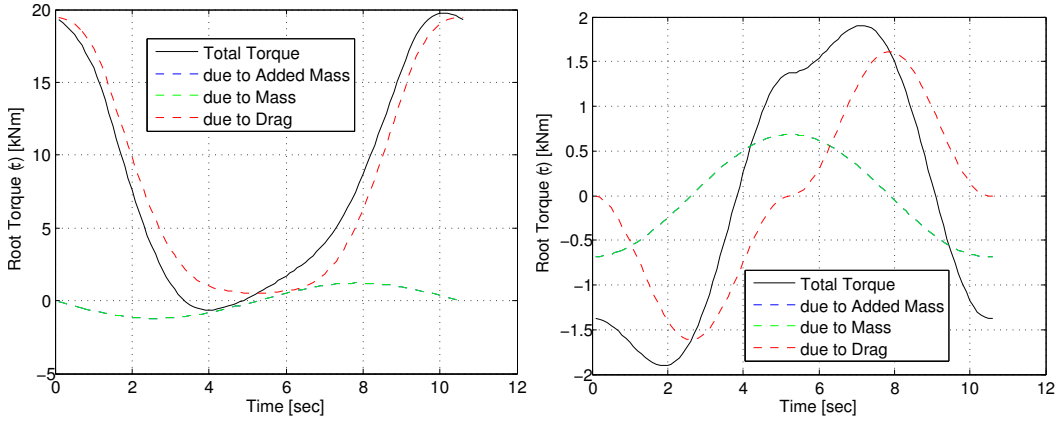

(a) (b)

Figure 4.7: Resultant torque from 2D General Plane Motion dynamic model, for submerged cylindrical link in (a) horizontal and (b) vertical planes due to drag, added mass, and mass effects as well as net resultant torque; given a minimum wave period (T_{min}) of 10.5 s.

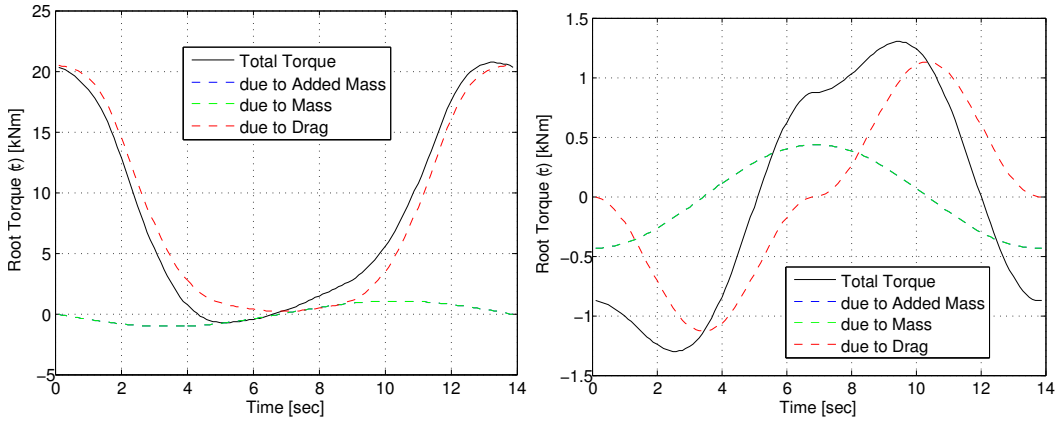

(a) (b)

Figure 4.8: Resultant torque from 2D General Plane Motion dynamic model, for submerged cylindrical link in (a) horizontal and (b) vertica l planes due to drag, added mass, and mass effects as well as net resultant torque; given a average wave period (T_{avg}) of 13.8 s.

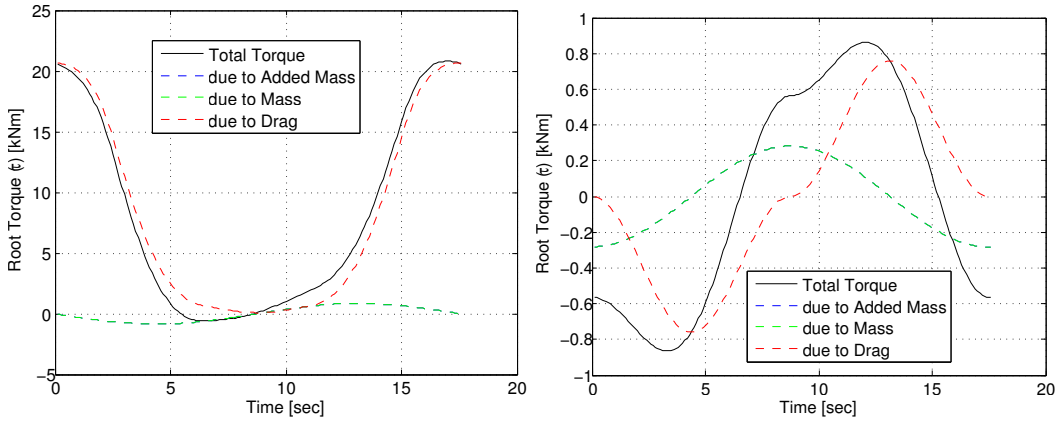

Figure 4.9: Resultant torque from 2D General Plane Motion dynamic model, for submerged cylindrical link in (a) horizontal and (b) vertical planes due to drag, added mass, and mass effects as well as net resultant torque; given a maximum wave period (T_{max}) of 17.5 s.

nitude [23]. The device could possibly operate in a swept-back position to improve streamlining, but the improvements are marginal. Alternatively,self-aligning fairings (*i.e.,* unactuated fairings which align freely with the flow) could be incorporated into the mechanically actuated dock design to improve streamlining.

Sweeping back a device of fixed overall length will reduce drag and possibly vibration. However, designing a swept-back device which must extend to an adjacent position (*i.e.*, the proposed workspace reach of 8 m) requires an increased overall length in comparison to a device which reaches the adjacent point with the minimum length. The later pertains to the RRP mechanically actuated docking concept. In pure translation a swept-back de-

sign will reduce the drag by a factor of $\cos\theta$ in comparison to the un-swept design in the identical flow. In rotation, preliminary results show that, due to the increased length the swept-back design will actually experience larger drag and force due to added mass than the direct design. Again, it is noted that, the torque required to overcome drag, increases quartically with length, while the torque required to overcome added mass, increases cubically with length, due to the links rotation. This increase due to length is greater than the reduction of $\cos\theta$ in drag in a swept-back device. This suggests fairing an unswept device would be a more appropriate solution for the mechanically actuated mechanism.

The 2D simulation shows the overall length and size of the device contributes significantly to the required actuation torques. This suggests the R$\perp$R$\|$R concept, shown in Figure 2.3, and the 2$\overline{\text{P}}$UU-SS concept, shown in Figure 2.4, are less feasible in comparison to the R$\perp$R$\perp$P concept, shown in Figure 2.5. Although the 2$\overline{\text{P}}$UU-SS concept may be able to have thinner links and therefore be streamlined, it requires longer overall link lengths which will increase drag cubically with length. The 2$\overline{\text{P}}$UU-SS link dimensions and interaction with one another requires further investigation, based on the preliminary Planar 2DOF model the 2$\overline{\text{P}}$UU-SS concept appears less feasible then the R$\perp$R$\perp$P (RRP) concept. Therefore, the R$\perp$R$\perp$P (RRP) concept is the most feasible device and will be further evaluated for simulation.

4.3 Dynamic Model Development of a Spatial 3DOF Submerged R⊥R⊥P Serial Manipulator

4.3.1 Kinematics

Conventional joint frames are assigned to each link, as shown in Fig. 4.10, using the Denavit-Hartenberg (DH) notation described in Craig [11]. The forward displacement problem, which describes a Cartesian end effector position given corresponding joint positions, is solved using the propagation of homogeneous transformation matrices. While, the inverse displacement solution, which describes joint positions corresponding to a given Cartesian end effector position, uses a geometric solution. The Jacobian is then derived and used to solve the velocity and acceleration vectors in both Cartesian and joint spaces respectively. The forward displacement solution is derived by propagating homogeneous transformation matrices from the base frame of the manipulator (0) outward towards the end effector (ee) . A homogeneous transformation matrix (${}^{i}_{i-1}\mathbf{T}$) describes a point in space relative to another,

$$ {}^{i}_{i-1}\mathbf{T} = \begin{bmatrix} & {}^{i}_{i-1}\mathbf{R} & & {}^{i}_{i-1}\mathbf{p} \\ & & & \\ 0 & 0 & 0 & 1 \end{bmatrix} \tag{4.40} $$

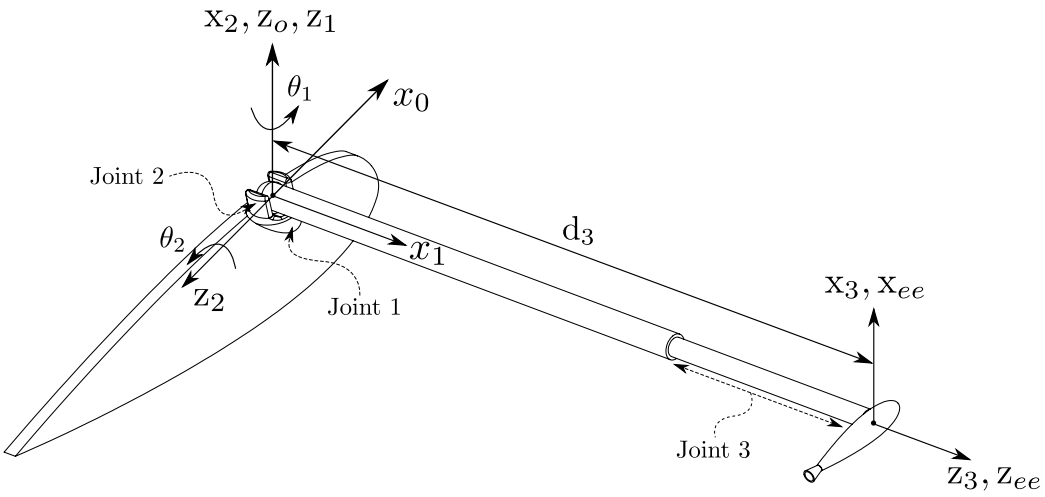

Figure 4.10: Denavit-Hartenberg frame assignment for RRP serial manipulator.

where the 3×3 rotation matrix ${}^{i}_{i-1}\mathbf{R}$ gives the orientation of joint i as seen from joint $i-1$ while the 3×1 position vector (${}^{i}_{i-1}\mathbf{p}$) gives the position of joint i from joint $i-1$ as seen from the base frame 0 of the manipulator. The position and orientation of link i is relative to link $i-1$ using the homogeneous transformation matrix ${}^{i}_{i-1}\mathbf{T}$.

The homogeneous transformation matrices are developed using the DH parameters, as described in Table 4.4, which define the relative link twist (α_{i-1}), link length (a_{i-1}), joint offset (d_i), and joint angle (θ_i) of each pair of joints in the mechanism. Link twist is the angle from z_{i-1} to z_i measured around x_{i-1}. Link length is the distance from z_{i-1} to z_i measured along x_{i-1}. The joint offset is the distance from x_{i-1} to x_i measured around z_i. The joint angle is the angle of x_{i-1} to x_i measured around z_i.

Joint i	α_{i-1}	a_{i-1}	d_i	θ_i
1	0	0	0	θ_1
2	$\frac{\pi}{2}$	0	0	θ_2
3	$\frac{\pi}{2}$	0	d_3	0
ee	0	0	0	0

Table 4.4: Denavit-Hartenberg parameters for RRP serial manipulator.

A homogeneous transformation matrix can now be obtained for each link of the manipulator, where,

$$
{}^{i}_{i-1}\mathbf{T} = \begin{bmatrix} \cos(\theta_i) & -\sin(\theta_i) & 0 & a_{i-1} \\ \sin(\theta_i)\cos(\alpha_{i-1}) & \cos(\theta_i)\cos(\alpha_{i-1}) & -\sin(\alpha_{i-1}) & -\sin(\alpha_{i-1})d_i \\ \sin(\theta_i)\sin(\alpha_{i-1}) & \cos(\theta_i)\sin(\alpha_{i-1}) & \cos(\alpha_i) & \cos(\alpha_{i-1})d_i \\ 0 & 0 & 0 & 1 \end{bmatrix} \tag{4.41}
$$

The transformation matrices are then pre-multiplied in a kinematic chain to obtain a specific joint's position and orientation relative to a defined frame, as described by the transformation equation,

$$
{}^{0}_{ee}\mathbf{T} = {}^{0}_{1}\mathbf{T}\,{}^{1}_{2}\mathbf{T}\,{}^{2}_{3}\mathbf{T}\,{}^{3}_{ee}\mathbf{T} \tag{4.42}
$$

The forward displacement solution, $\mathbf{x}$, can then be expressed as ${}^{0}_{ee}\mathbf{p}$ extracted

from the product of the homogeneous transformation matrix ${}^{0}_{ee}\mathbf{T}$,

$$ {}^{0}_{ee}\mathbf{p} = \mathbf{x} = \begin{bmatrix} \cos(\theta_1)\sin(\theta_2)d_3 \\ \sin(\theta_1)\sin(\theta_2)d_3 \\ -\cos(\theta_2)d_3 \end{bmatrix} \tag{4.43} $$

where θ_1 is the joint position of joint 1, θ_2 is the joint position of joint 2, and d_3 is the joint position of joint 3. ${}^{0}_{ee}\mathbf{p}$ describes the end effector position in Cartesian space relative to the base frame $\{0\}$.

The inverse displacement, $\mathbf{\Theta}$, solution is solved geometrically. $\mathbf{\Theta}$ describes the manipulator's position in joint space. That is, given a Cartesian end effector position, the inverse displacement problem will give the required joint positions to obtain the given Cartesian end effector position. The quadrant corrected arctangent function is applied to solve a specific joint angle θ_i, given the vector components of link i as seen from the base frame of the manipulator.

$$ \mathbf{\Theta} = \begin{bmatrix} \text{atan2}(y, x) \\ \text{atan2}(z, \sqrt{y^2 + x^2}) + \frac{\pi}{2} \\ \sqrt{x^2 + y^2 + z^2} \end{bmatrix} \tag{4.44} $$

where $\mathbf{\Theta}$ is a vector of joint positions.

The forward velocity solution is obtained through solving the time derivative of the forward displacement problem; it is convenient to write the

forward velocity solution in the form of a matrix equation,

$$\dot{\mathbf{x}} = \mathbf{J}(\mathbf{\Theta})\dot{\mathbf{\Theta}} \tag{4.45}$$

where $\dot{\mathbf{x}}$ is a vector of Cartesian velocities of the end effector, $\dot{\mathbf{\Theta}}$ is a vector of joint velocities, and $\mathbf{J}$ is the Jacobian matrix of the manipulator. The Jacobian matrix is defined as the matrix that transforms the joint rates in actuator space to the velocity state in the end effector space [28], and can be described as,

$$\mathbf{J}(\mathbf{\Theta}) = \begin{bmatrix} -\sin(\theta_1)\sin(\theta_2)d_3 & \cos(\theta_1)\cos(\theta_2)d_3 & cos(\theta_1)\sin(\theta_2) \\ \cos(\theta_1)\sin(\theta_2)d_3 & \sin(\theta_1)\cos(\theta_2)d_3 & \sin(\theta_1)\sin(\theta_2) \\ 0 & \sin(\theta_2)d_3 & -\cos(\theta_2) \end{bmatrix} \tag{4.46}$$

The forward velocity vector equation (4.45) is manipulated using basic matrix operations, the inverse velocity solution can be solved,

$$\dot{\mathbf{\Theta}} = \mathbf{J}^{-1}(\mathbf{\Theta})\dot{\mathbf{x}} \tag{4.47}$$

Similarly, the forward and inverse acceleration solutions are derived by taking the time derivative of the forward and inverse velocity solution

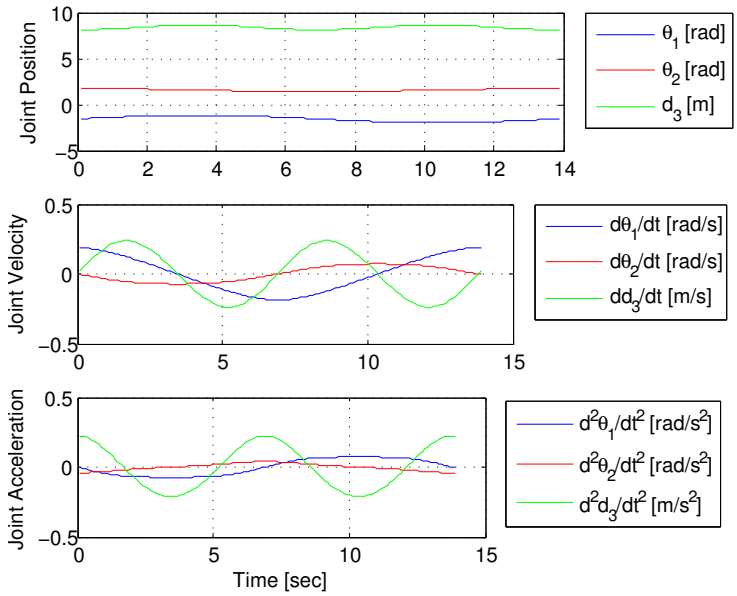

Figure 4.11: Resultant joint kinematics from Spatial 3DOF Inverse kinematic model, given an average wave period (T_{avg}) of 13.8 s.

matrix equation respectively,

$$\ddot{\mathbf{x}} = \dot{\mathbf{J}}(\mathbf{\Theta})\dot{\mathbf{\Theta}} + \mathbf{J}(\mathbf{\Theta})\ddot{\mathbf{\Theta}} \tag{4.48}$$

$$\ddot{\mathbf{\Theta}} = \dot{\mathbf{J}}^{-1}(\mathbf{\Theta})\dot{\mathbf{x}} + \mathbf{J}^{-1}(\mathbf{\Theta})\ddot{\mathbf{x}} \tag{4.49}$$

where $\ddot{\mathbf{x}}$ is a vector of Cartesian accelerations, $\ddot{\mathbf{\Theta}}$ is a vector of joint accelerations, and $\dot{\mathbf{J}}$ is the time derivative of the Jacobian matrix of the manipulator. The serial manipulator kinematics can now be fully defined; allowing the motion of mechanism to be described in both Cartesian space and joint space.

To verify both the forward and inverse kinematic models a simple test is presented. First set point trajectories are defined for the Cartesian kine-

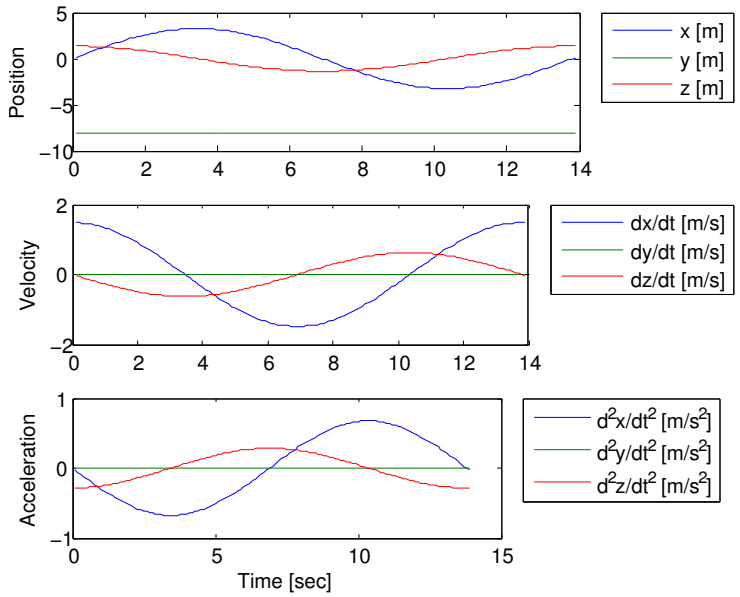

Figure 4.12: Resultant end effector kinematics from Spatial 3DOF forward kinematic model, given a average wave period (T_{avg}) of 13.8 s.

matics of the end effector using the AUV trajectory defined in Figure 3.3 with a nominal offset from the submarine of y = -8 m. The set points are evaluated using the inverse kinematic model, Eq. (4.44) for joint displacement, Eq. (4.47) for joint velocities, and Eq. (4.49) for joint accelerations with the results shown in Figure 4.11. These results are then used as inputs to the forward kinematic model, where Eq. (4.43) defines the end effector position, Eq. (4.45) defines the end effector velocity, and Eq. (4.48) defines the end effector acceleration. The forward kinematic model results are shown in Figure 4.12. The forward model results are then compared with the original setpoint profiles used as inputs to the inverse kinematic model. The resulting error is plotted in Figure 4.13. The minimal error shows both the inverse

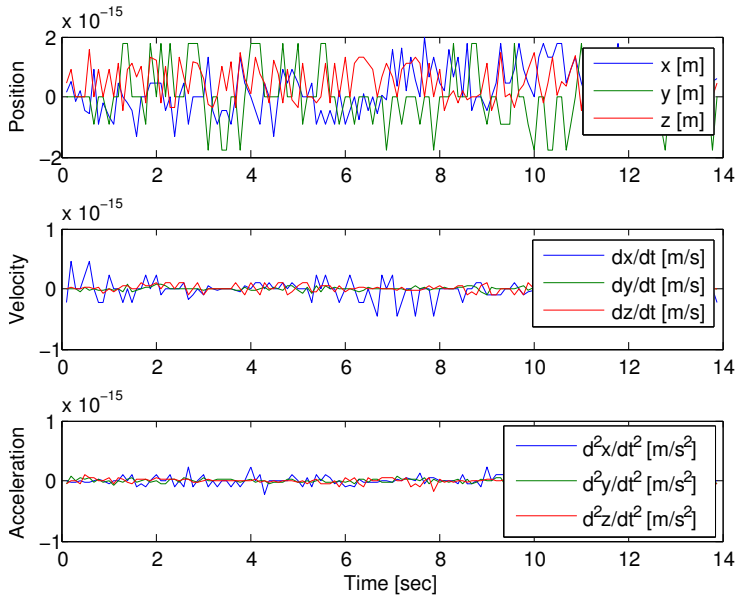

Figure 4.13: Resultant error between Spatial 3DOF forward kinematic model and inverse kinematic model, given a average wave period (T_{avg}) of 13.8 s.

and kinematic models behave as expected. The kinematic model can now be used to define trajectories for the Spatial 3DOF simulation.

4.3.2 Dynamics

The links of the RRP are assumed to be rigid bodies. The dynamic equations are propagated outward from the base to the end effector; using the propagated forward solution an inverse solution is solved. Knowing the kinematics of the end effector and the acting external forces on the mechanism the specific joint torques can be calculated.

The general form of the angular velocity of joint $i+1$ can be derived

as,

$$ {}^{i+1}\boldsymbol{\omega}_{i+1} = {}^{i+1}_{i}\mathbf{R}\,{}^{i}\boldsymbol{\omega}_{i} + \dot{\theta}_{i+1}\,{}^{i+1}\hat{\mathbf{z}}_{i+1} \tag{4.50} $$

and is a function of the angular velocity of the previous joint ${}^{i}\boldsymbol{\omega}_{i}$ and the current joint's joint velocity $\dot{\theta}_{i}$. Applying Eq. (4.50) to the specific joint variables, the angular velocity of each link is propagated,

$$ {}^{1}\boldsymbol{\omega}_{1} = {}^{1}_{0}\mathbf{R}\,{}^{0}\boldsymbol{\omega}_{0} + \dot{\theta}_{1}\,{}^{1}\hat{\mathbf{z}}_{1} \tag{4.51a} $$

$$ {}^{2}\boldsymbol{\omega}_{2} = {}^{2}_{1}\mathbf{R}\,{}^{1}\boldsymbol{\omega}_{1} + \dot{\theta}_{2}\,{}^{2}\hat{\mathbf{z}}_{2} \tag{4.51b} $$

$$ {}^{3}\boldsymbol{\omega}_{3} = {}^{3}_{2}\mathbf{R}\,{}^{2}\boldsymbol{\omega}_{2} \tag{4.51c} $$

$$ {}^{ee}\boldsymbol{\omega}_{ee} = {}^{3}\boldsymbol{\omega}_{3} \tag{4.51d} $$

It is useful to note ${}^{0}\boldsymbol{\omega}_{0}$, the angular velocity of the base of the manipulator, is typically a zero vector as most manipulators are assumed to have a fixed base. However, this allows the base frame of the manipulator to be defined as a non-inertial frame, such as the rate of roll, pitch, and yaw of a submarine.

The velocity of link $i+1$ can derived in the general form of,

$$ {}^{i+1}\mathbf{v}_{i+1} = {}^{i+1}_{i}\mathbf{R}\left({}^{i}\mathbf{v}_{i} + {}^{i}\boldsymbol{\omega}_{i} \times {}^{i}\mathbf{p}_{i+1}\right) \tag{4.52} $$

for a revolute joint, and,

$$ {}^{i+1}\mathbf{v}_{i+1} = {}^{i+1}_{i}\mathbf{R}\left({}^{i}\mathbf{v}_{i} + {}^{i}\boldsymbol{\omega}_{i} \times {}^{i}\mathbf{p}_{i+1}\right) + \dot{d}_{i+1}\,{}^{i+1}\hat{\mathbf{z}}_{i+1} \tag{4.53} $$

for a prismatic joint. Eq. (4.53) incorporates the velocity due to the extension of the link connected to the prismatic joint. The link velocities for the RRP can be derived as,

$$ {}^{1}\mathbf{v}_1 = {}^{1}_{0}\mathbf{R}\left({}^{0}\mathbf{v}_0 + {}^{0}\boldsymbol{\omega}_0 \times {}^{0}\mathbf{p}_1\right) \tag{4.54a} $$

$$ {}^{2}\mathbf{v}_2 = {}^{2}_{1}\mathbf{R}\left({}^{1}\mathbf{v}_1 + {}^{1}\boldsymbol{\omega}_1 \times {}^{1}\mathbf{p}_2\right) \tag{4.54b} $$

$$ {}^{3}\mathbf{v}_3 = {}^{3}_{2}\mathbf{R}\left({}^{2}\mathbf{v}_2 + {}^{2}\boldsymbol{\omega}_2 \times {}^{2}\mathbf{p}_3\right) + \dot{d}_3 {}^{3}\hat{\mathbf{z}}_3 \tag{4.54c} $$

$$ {}^{3}\mathbf{v}_3 = {}^{ee}\mathbf{v}_e \tag{4.54d} $$

Similar to the angular velocity vector of the base frame, a velocity vector ${}^{0}\mathbf{v}_0$ can be defined to represent the velocity of the base frame of the manipulator. This is equivalent to placing the entire manipulator in motion, such as the forward velocity of the submarine.

The general formulation of the angular acceleration ${}^{i+1}\dot{\boldsymbol{\omega}}_{i+1}$ of a link due to a revolute joint is described as,

$$ {}^{i+1}\dot{\boldsymbol{\omega}}_{i+1} = {}^{i+1}_{i}\mathbf{R}\,{}^{i}\dot{\boldsymbol{\omega}}_i + {}^{i+1}_{i}\mathbf{R}\,{}^{i}\boldsymbol{\omega}_i \times \dot{\theta}_{i+1}\,{}^{i+1}\hat{\mathbf{z}}_{i+1} + \ddot{\theta}_{i+1}\,{}^{i+1}\hat{\mathbf{z}}_{i+1} \tag{4.55} $$

Whereas, the general formulation of the angular acceleration of a link due to a prismatic joint is simply,

$$ {}^{i+1}\dot{\boldsymbol{\omega}}_{i+1} = {}^{i+1}_{i}\mathbf{R}\,{}^{i}\dot{\boldsymbol{\omega}}_i \tag{4.56} $$

The angular acceleration of each link can be then be derived as,

$$ {}^{1}\dot{\boldsymbol{\omega}}_1 = {}^{1}_{0}\mathbf{R}\,{}^{0}\dot{\boldsymbol{\omega}}_0 + {}^{1}_{0}\mathbf{R}\,{}^{0}\boldsymbol{\omega}_0 \times \dot{\theta}_1\,{}^{1}\hat{\mathbf{z}}_1 + \ddot{\theta}_1\,{}^{1}\hat{\mathbf{z}}_1 \tag{4.57a} $$

$$ {}^{2}\dot{\boldsymbol{\omega}}_2 = {}^{2}_{1}\mathbf{R}\,{}^{1}\dot{\boldsymbol{\omega}}_1 + {}^{2}_{1}\mathbf{R}\,{}^{1}\boldsymbol{\omega}_1 \times \dot{\theta}_2\,{}^{2}\hat{\mathbf{z}}_2 + \ddot{\theta}_2\,{}^{2}\hat{\mathbf{z}}_2 \tag{4.57b} $$

$$ {}^{3}\dot{\boldsymbol{\omega}}_3 = {}^{3}_{2}\mathbf{R}\,{}^{2}\dot{\boldsymbol{\omega}}_2 \tag{4.57c} $$

$$ {}^{ee}\dot{\boldsymbol{\omega}}_{ee} = {}^{3}\dot{\boldsymbol{\omega}}_3 \tag{4.57d} $$

The general form of the acceleration of link $i+1$, ${}^{i+1}\dot{\mathbf{v}}_{i+1}$, can be derived as,

$$ {}^{i+1}\dot{\mathbf{v}}_{i+1} = {}^{i+1}_{i}\mathbf{R}\left({}^{i}\dot{\boldsymbol{\omega}}_i \times {}^{i}\mathbf{p}_{i+1} + {}^{i}\boldsymbol{\omega}_i \times \left({}^{i}\boldsymbol{\omega}_i \times {}^{i}\mathbf{p}_{i+1}\right) + {}^{i}\dot{\mathbf{v}}_i\right) \tag{4.58} $$

due to a revolute joint, and,

$$ \begin{aligned} {}^{i+1}\dot{\mathbf{v}}_{i+1} = {}^{i+1}_{i}\mathbf{R}\left({}^{i}\dot{\omega}_i \times {}^{i}\mathbf{p}_{i+1} + {}^{i}\boldsymbol{\omega}_i \times \left({}^{i}\boldsymbol{\omega}_i \times {}^{i}\mathbf{p}_{i+1}\right) + {}^{i}\dot{\mathbf{v}}_i\right) \\ + 2\,{}^{i+1}\boldsymbol{\omega}_{i+1} \times \dot{\mathbf{d}}_{i+1}\,{}^{i+1}\hat{\mathbf{z}}_{i+1} + \ddot{\mathbf{d}}_{i+1}\,{}^{i+1}\hat{\mathbf{z}}_{i+1} \end{aligned} \tag{4.59} $$

due to a prismatic joint which must account for Coriolis effects. Applying Eq. (4.58) and Eq. (4.59), the specific equations for the acceleration of each link can then be described as,

$$ {}^{1}\dot{\mathbf{v}}_1 = {}^{1}_{0}\mathbf{R}\left({}^{0}\dot{\boldsymbol{\omega}}_0 \times {}^{0}\mathbf{p}_1 + {}^{0}\boldsymbol{\omega}_0 \times \left({}^{0}\boldsymbol{\omega}_0 \times {}^{0}\mathbf{p}_1\right) + {}^{0}\dot{\mathbf{v}}_0\right) \tag{4.60a} $$

$$ {}^{2}\dot{\mathbf{v}}_2 = {}^{2}_{1}\mathbf{R}\left({}^{1}\dot{\boldsymbol{\omega}}_1 \times {}^{1}\mathbf{p}_2 + {}^{1}\boldsymbol{\omega}_1 \times \left({}^{1}\boldsymbol{\omega}_1 \times {}^{1}\mathbf{p}_2\right) + {}^{1}\dot{\mathbf{v}}_1\right) \tag{4.60b} $$

$$ \begin{aligned} {}^{3}\dot{\mathbf{v}}_3 = {}^{3}_{2}\mathbf{R}\left({}^{2}\dot{\omega}_2 \times {}^{2}\mathbf{p}_3 + {}^{2}\boldsymbol{\omega}_2 \times \left({}^{2}\boldsymbol{\omega}_2 \times {}^{2}\mathbf{p}_3\right) + {}^{2}\dot{\mathbf{v}}_2\right) \\ + 2{}^{3}\boldsymbol{\omega}_3 \times \dot{\mathbf{d}}_3{}^{3}\hat{\mathbf{z}}_3 + \ddot{\mathbf{d}}_3{}^{3}\hat{\mathbf{z}}_3 \end{aligned} \tag{4.60c} $$

$$ {}^{ee}\dot{\mathbf{v}}_{ee} = {}^{3}\dot{\mathbf{v}}_3 \tag{4.60d} $$

The inertial force, ${}^{i+1}\mathbf{F}_{i+1}$, and inertial moment, ${}^{i+1}\mathbf{N}_{i+1}$, acting on link $i+1$ can now be evaluated using the forward propagated dynamic equations. First, the acceleration of center of mass of the link is determined,

$$ {}^{i+1}\dot{\mathbf{v}}_{\mathbf{c}i+1} = {}^{i+1}\dot{\boldsymbol{\omega}}_{i+1} \times {}^{i+1}\mathbf{p}_{\mathbf{c}i+1} + {}^{i+1}\boldsymbol{\omega}_{i+1} \times \left({}^{i+1}\boldsymbol{\omega}_{i+1} \times {}^{i+1}\mathbf{p}_{\mathbf{c}i+1}\right) + {}^{i+1}\dot{\mathbf{v}}_{i+1} \tag{4.61} $$

where ${}^{i+1}\mathbf{p}_{\mathbf{c}i+1}$ is the position vector of the center of mass of link $i+1$ as seen from frame $i+1$. That is,

$$ {}^{1}\mathbf{p}_{\mathbf{c}1} = [0, 0, 0]^T \tag{4.62a} $$

$$ {}^{2}\mathbf{p}_{\mathbf{c}2} = [0, -L_2/2, 0]^T \tag{4.62b} $$

$$ {}^{3}\mathbf{p}_{\mathbf{c}3} = [0, 0, -L_3/2]^T \tag{4.62c} $$

The inertial force acting on each link can now be derived as,

$$ {}^{i+1}\mathbf{F}_{i+1} = m_{i+1}{}^{i+1}\dot{\mathbf{v}}_{\mathbf{c}_{i+1}} \tag{4.63} $$

where m_{i+1} is the mass of link $i+1$ and can be derived as the mass of the volume of water which the link displaces, due to the assumption of neutral buoyancy. The inertial moment for link $i+1$ is then represented by,

$$ {}^{i+1}\mathbf{N}_{i+1} = {}^{i+1}\mathbf{I}_{i+1}\,{}^{i+1}\dot{\boldsymbol{\omega}}_{i+1} + {}^{i+1}\boldsymbol{\omega}_{i+1} \times {}^{i+1}\mathbf{I}_{i+1}\,{}^{i+1}\boldsymbol{\omega}_{i+1} \tag{4.64} $$

The hydrodynamic forces acting on the links can now be derived using the principles presented in Section 4.1. This completes the outward formulation of the dynamic model. The revised inward solution for equations of motion then become,

$$ {}^{i}\mathbf{f}_i = {}^{i}_{i+1}\mathbf{R}\;{}^{i+1}\mathbf{f}_{i+1} + {}^{i}\mathbf{F}_i + {}^{i}\mathbf{f}_{h_i} \tag{4.65} $$

$$ {}^{i}\mathbf{n}_i = {}^{i}\mathbf{N}_i + {}^{i}\mathbf{n}_{h_i} + {}^{i}_{i+1}\mathbf{R}\;{}^{i+1}\mathbf{n}_{i+1} + {}^{i}\mathbf{p}_{C_i} \times {}^{i}\mathbf{F}_i + {}^{i}\mathbf{p}_{i+1} \times {}^{i}_{i+1}\mathbf{R}\;{}^{i+1}\mathbf{f}_{i+1} \tag{4.66} $$

to determine the force, ${}^{i}\mathbf{f}_i$, and moment, ${}^{i}\mathbf{n}_i$, exerted on link i by link $i-1$. Where $\mathbf{f}_{\mathbf{h}i}$ and $\mathbf{n}_{\mathbf{h}i}$ is derived in Section 4.1 as Eq. 4.30a and Eq. 4.30b respectively, and ${}^{i}\mathbf{p}_{C_i}$ describes the location of the centre of gravity of link i with respect to the origin of frame i. The dynamic equations of a manipulator allow the joint torques or joint forces (τ_i) to be calculated as a function of joint type.

$$ {}^{Revolute}\tau_i = {}^{i}\mathbf{n}_i^{T\,i}\hat{\mathbf{z}}_i \tag{4.67} $$

$$ {}^{Prismatic}\tau_i = {}^{i}\mathbf{f}_i^{T\,i}\hat{\mathbf{z}}_i \tag{4.68} $$

where ${}^{i}\mathbf{n}_i$ is the moment vector experienced by joint i, ${}^{i}\mathbf{f}_i$ is the force vector experienced by joint i, and $\hat{\mathbf{z}}_i$ is a unit vector corresponding to the degree of freedom joint i constrains. It should be noted that the remaining components of the force and moment are assumed to be supported by the structure of the manipulator; that is, they are sustained by the joint which constrains the relative degree of freedom.

4.3.3 Analytical Verification of Spatial 3DOF Dynamic Model

The spatial 3DOF dynamic model is verified in two stages. The first being the same as Section 4.2, where the model is tested in quiescent water to verify its translational and angular components using 2D strip theory. A linear constant acceleration test case is added, to the Section 4.2 test cases, to verify the translational component of added mass. Although the submarine will maintain a constant linear velocity during docking, the Spatial 3DOF dynamic model accounts for linear acceleration of the manipulator base, *i.e.* submarine acceleration, for completeness. Therefore, four quiescent water verification tests are presented:

- the manipulator moves in pure translation, extended perpendicular to the onset flow in quiescent water, with a forward velocity ${}^{0}\mathbf{v}_0 = [1, 0, 0]^T$ m/s,
- the manipulator rotates about a fixed position in quiescent water, with

a constant angular velocity $\dot{\theta}_1 = 0.1$ rad/s,

- the manipulator rotates about a fixed position in quiescent water, with a constant angular acceleration $\ddot{\theta}_1 = 0.001$ rad/s^2,

- and the manipulator moves in pure translation, extended perpendicular to the onset flow in quiescent water, with a forward acceleration of ${}^0\dot{\mathbf{v}}_0 = [0.1, 0, 0]^T$ m/s^2.

Again, verification tests one and two verify the linear and rotational portions of Eq. (4.22) respectively as well as verifying both Eq. (4.24) and Eq. (4.25). While verification tests three and four verify the linear and rotational portions of Eq. (4.23) respectively as well as verifying both Eq. (4.26) and Eq. (4.27). The second stage of analytical testing will verify the Froude-Krylov force Eq. (4.18) in the presence of waves. One verification test is presented,

- the manipulator moves in pure translation, extended perpendicular to the onset flow, with a forward acceleration of ${}^0\dot{\mathbf{v}}_0 = [0.1, 0, 0]^T$ m/s, while the flow has an equal and opposite acceleration of $\dot{\mathbf{U}} = [-0.1, 0, 0]^T$ m/s^2.

The first test case is verified using Eq. (4.33) and Eq. (4.34). The results are plotted in Figure 4.14 and Figure 4.15. The plotted results correspond to the analytical results for test case one shown in Table 4.1. Therefore, the linear drag component of the spatial 3DOF dynamic model is

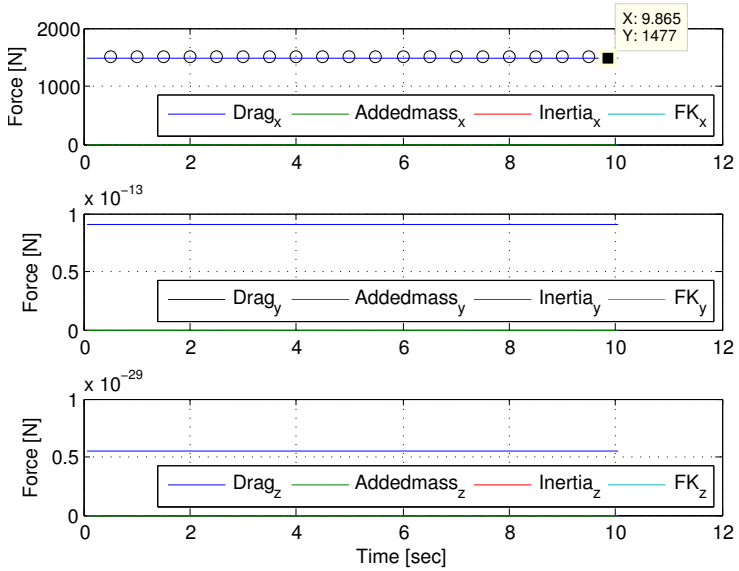

Figure 4.14: Resultant force from Spatial 3DOF dynamic model, for submerged cylindrical link RRP manipulator in quiescent water moving in pure translation with a constant velocity of 1 m/s (*Test Case 1*).

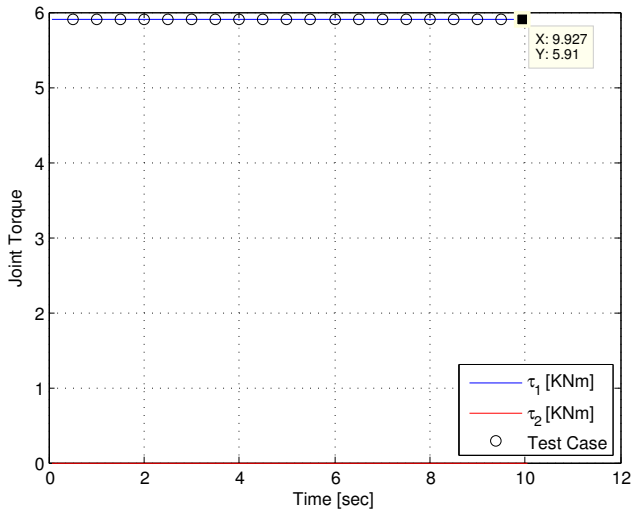

Figure 4.15: Resultant torque from Spatial 3DOF dynamic model, for submerged cylindrical link RRP manipulator in quiescent water moving in pure translation with a constant velocity of 1 m/s (*Test Case 1*).

verified by the simplified analytical result. Again, the simulation shows added mass and inertial effects do not contribute to the required joint torque in translation with a constant velocity as they are both functions of acceleration.

The second test case is verified using Eq. (4.36) and Eq. (4.37). The results of the spatial 3DOF dynamic model are plotted in Figure 4.16 and Figure 4.17 corresponding to the analytical results for test case two shown in Table 4.2. The spatial 3DOF dynamic model results are verified by the simplified analytical result. Like test case one, the simulation shows added mass and inertial effects do not contribute to the required joint torque when rotating at a constant angular velocity about a fixed axis. This verifies the rotational drag component of the spatial 3DOF dynamic model.

The third test case is verified using Eq. (4.38) and Eq. (4.39). The results of the spatial 3DOF dynamic model are plotted in Figure 4.18 and Figure 4.19 corresponding to the analytical results for test case three shown in Table 4.3. The spatial 3DOF dynamic model results are verified by the simplified analytical result. The result shows the force due to added mass and the inertia is constant due to the constant angular acceleration. This verifies the rotational added mass component of the spatial 3DOF dynamic model.

The analytical equations for the fourth case are derived similarly to test case one. The analytical drag equation and torque due to drag are identical to those of test case two, Eq. 4.33. and Eq. 4.34 respectively. The

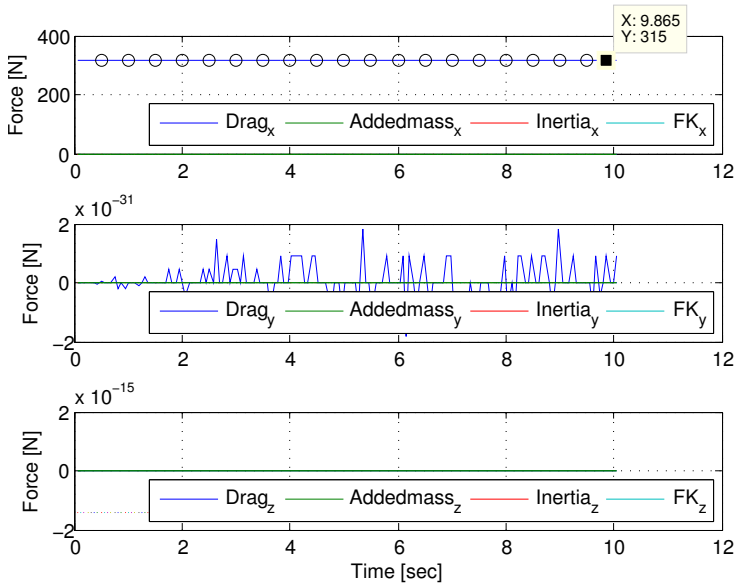

Figure 4.16: Resultant force from Spatial 3DOF dynamic model, for submerged cylindrical link RRP manipulator in quiescent water moving in pure rotation with a constant angular velocity of 0.1 rad/s (*Test Case 2*).

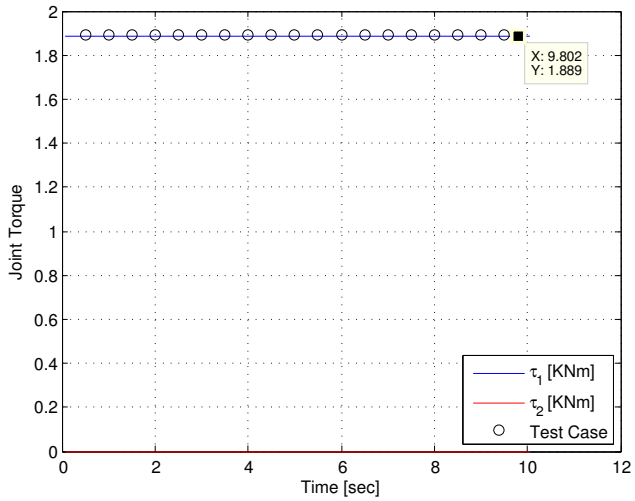

Figure 4.17: Resultant torque from Spatial 3DOF dynamic model, for submerged cylindrical link RRP manipulator in quiescent water moving in pure rotation with a constant angular velocity of 0.1 rad/s (*Test Case 2*).

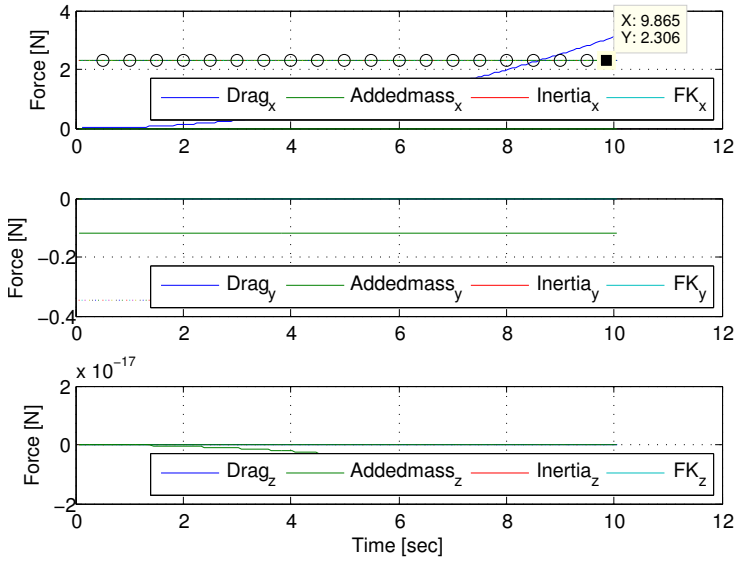

Figure 4.18: Resultant force from Spatial 3DOF dynamic model, for submerged cylindrical link RRP manipulator in quiescent water moving in pure rotation with a constant angular acceleration of 0.001 rad/s^2 (*Test Case 3*).

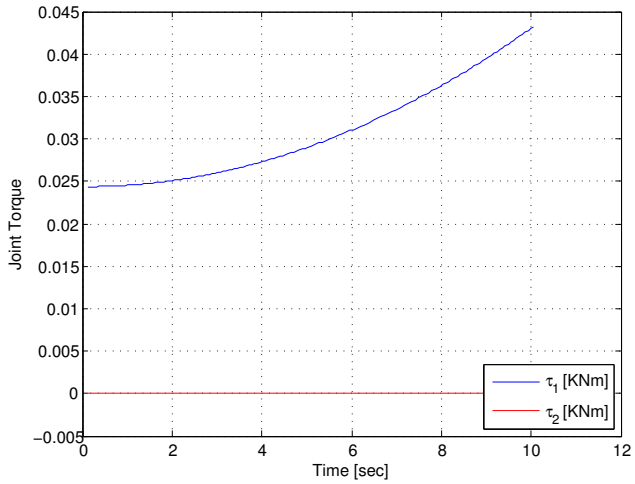

Figure 4.19: Resultant torque from Spatial 3DOF dynamic model, for submerged cylindrical link RRP manipulator in quiescent water moving in pure rotation with a constant angular acceleration of 0.001 rad/s^2 (*Test Case 3*).

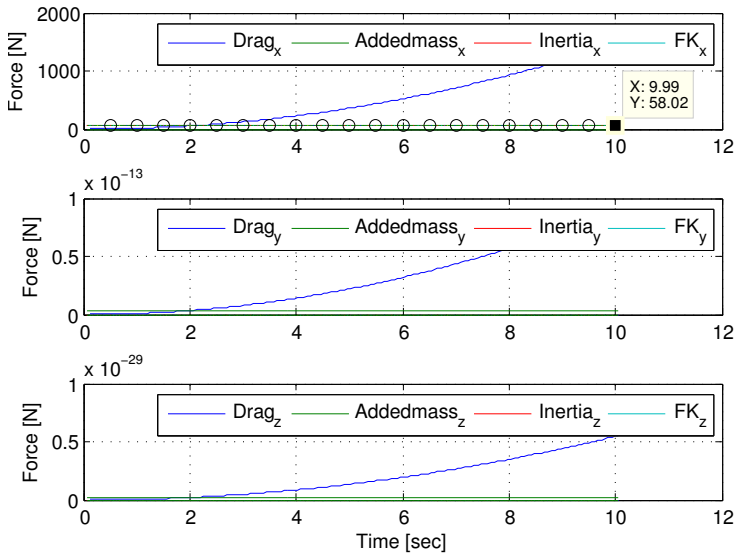

Figure 4.20: Resultant force from Spatial 3DOF dynamic model, for submerged cylindrical link RRP manipulator in quiescent water moving in pure translation with a constant acceleration of 0.1 m/s^2, with analytical force result ($\mathbf{f}_{am} = 58.02$ N) denoted by circle. (*Test Case 4*).

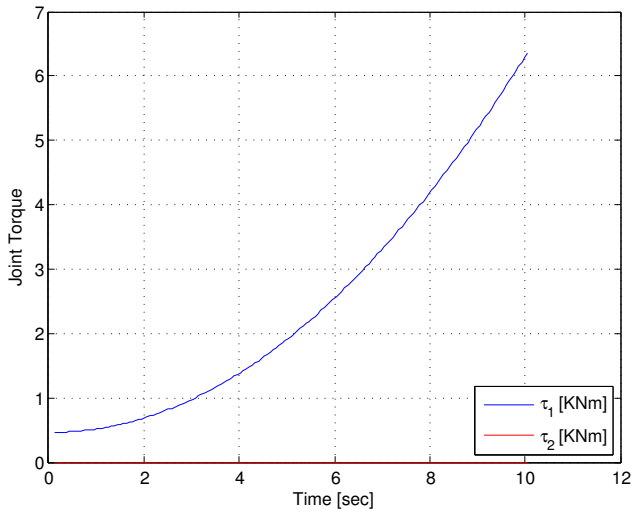

Figure 4.21: Resultant torque from Spatial 3DOF dynamic model, for submerged cylindrical link RRP manipulator in quiescent water moving in pure translation with a constant acceleration of 0.1 m/s^2 (*Test Case 4*).

analytical equation for the linear force due to added mass can be defined as,

$$\mathbf{f_{am}} = \rho\frac{\pi}{4}{d_o}^2\int_0^L(\dot{u})dy \tag{4.69}$$

The torque due to added mass and the inertia of the link are present with acceleration. Therefore, the torque required at the joint can be defined as,

$$\tau_i = I\ddot{\theta} + \left(\frac{1}{2}C_D d_o\rho\int_0^L u^2dy + \rho\frac{\pi}{4}{d_o}^2\int_0^L(\dot{u})dy\right) \tag{4.70}$$

The results of the spatial 3DOF dynamic model are plotted in Figure 4.18 and Figure 4.19 corresponding to the analytical results for test case four denoted by circle in Figure 4.20). The spatial 3DOF dynamic model

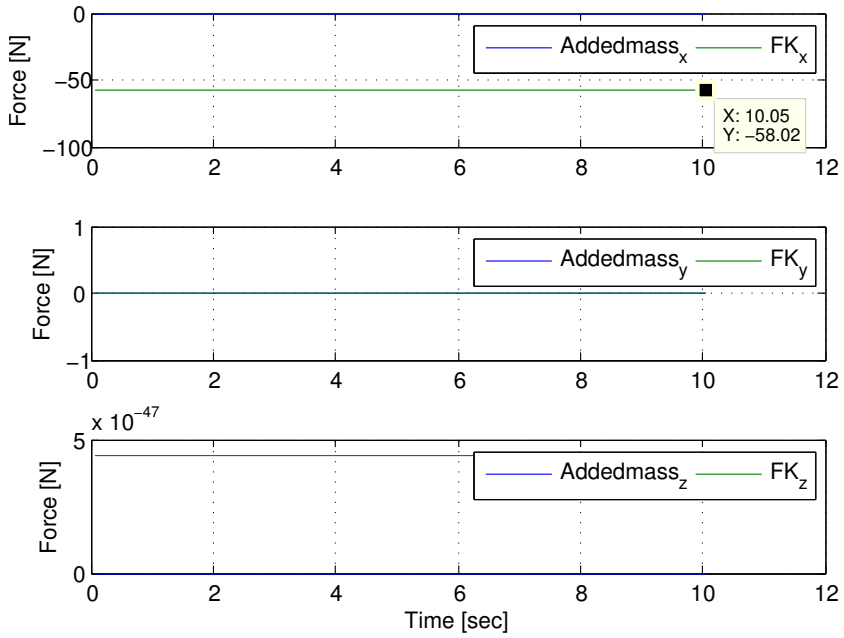

Figure 4.22: Resultant force from Spatial 3DOF dynamic model, for submerged cylindrical link RRP manipulator in moving water, with a flow acceleration of $\dot{\mathbf{U}} = [-0.1, 0, 0]^T$ m/s^2, moving in pure translation with a constant acceleration of ${}^0\dot{\mathbf{v}}_0 = [0.01, 0, 0]^T$ m/s^2.

results are verified by the simplified analytical result. The result shows the force due to added mass is constant due to the constant linear acceleration. This verifies the linear added mass component of the spatial 3DOF dynamic model.

For the second stage test verifying the Froude-Krylov force, test case 5, the analytical equations are derived from Eq. (4.18) and Eq. (4.14). The onset acceleration, $\dot{\mathbf{q}}$, will equal zero due to the acceleration of the manipulator base, ${}^0\dot{\mathbf{v}}_0$, being equal in magnitude and opposite in direction of the fluid acceleration, $\dot{\mathbf{U}}$. This results in no force due to added mass but a Froude-

Krylov force being present with a value of $\mathbf{f}_{FK} = -58.02$ N.

The results of the spatial 3DOF dynamic model are plotted in Figure 4.22 corresponding to the analytical results for test case 5. The spatial 3DOF dynamic model results are verified by the simplified analytical result. This verifies the Froude-Krylov force component of the spatial 3DOF dynamic model.

4.3.4 Simulation of Spatial 3DOF RRP Dynamic Model

The spatial 3DOF model of the RRP fully mechanically actuated mechanism can now be used to estimate the required actuator loads to track the established design trajectories in Chapter 3. The design trajectories are rotated into the base frame coordinates of the RRP serial manipulator and located on a plane at y_o=-8 m, for the average wave period shown in Figure 4.12. The inverse kinematic model can then be employed to determine the joint torques, for the average wave period shown in Figure 4.11. This is repeated for both the minimum and maximum wave periods.

The spatial 3DOF dynamic model of the RRP serial manipulator can be evaluated using the design trajectories. The model is simulated for both quiescent water and for the presence of waves. First, the quiescent water simulations are plotted in Figure 4.23 for an end effector design trajectory with a period of 10.5 s, Figure 4.24 for an end effector design trajectory with a period of 13.8 s, and Figure 4.25 for an end effector design trajectory with a period of 17.5 s. Note the values of torque for joint two τ_2 are larger than

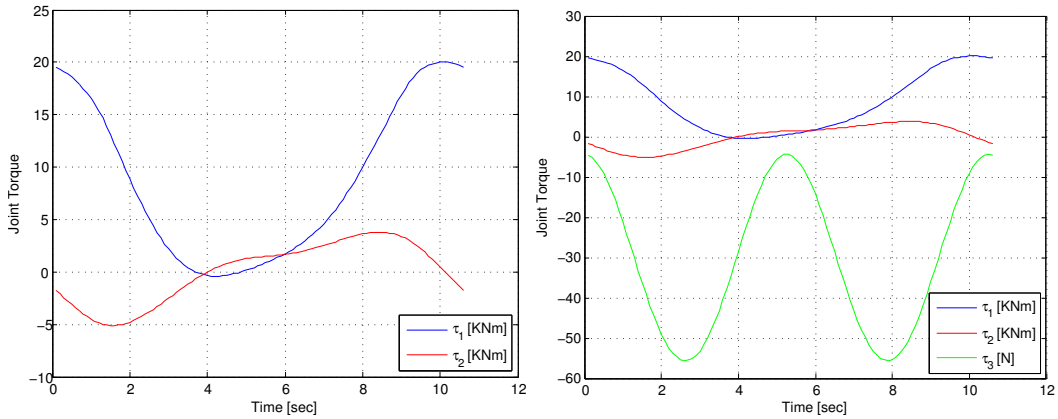

(a) (b)

Figure 4.23: Resultant joint torque from Spatial 3DOF dynamic model, for submerged cylindrical link RRP manipulator in quiescent water showing (a) joints one and two in detail and (b) all joint torques given an end effector design trajectory with a minimum period (T_{min}) of 10.5 s.

the estimated values of torque for the vertical plane using the planar model in Section 4.8. This is due to the planar model strictly evaluating the motion in the vertical plane, omitting the contribution of the horizontal forward velocity component to the local onset velocity at the 2D cross=sectional plane. Hence, the increase in τ_2 in the spatial 3D dynamic model. Secondly, waves are incorporated into the simulation resulting in the Froude-Krylov force being present. The results are plotted in Figure 4.26 for the minimum wave period, Figure 4.27 for the average wave period, and Figure 4.28 for the maximum wave period.

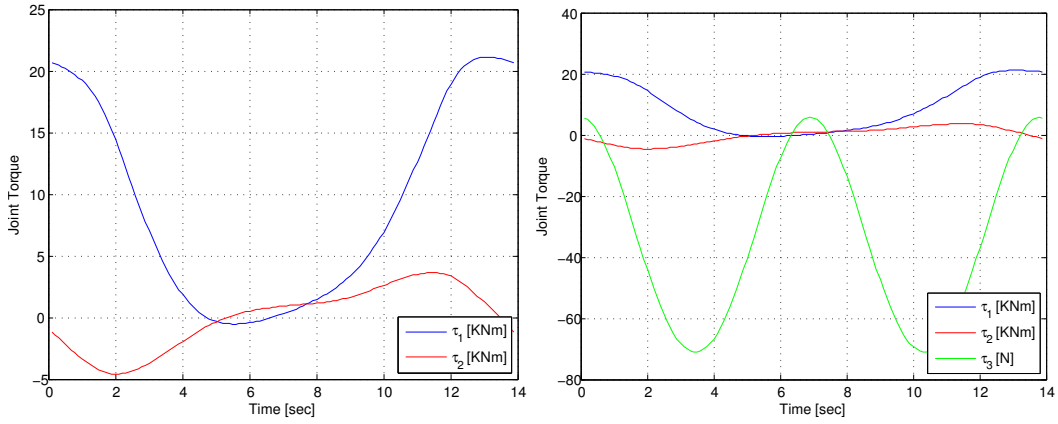

(a) (b)

Figure 4.24: Resultant joint torque from Spatial 3DOF dynamic model, for submerged cylindrical link RRP manipulator in quiescent water showing (a) joints one and two in detail and (b) all joint torques given an end effector design trajectory with a average period (T_{avg}) of 13.8 s.

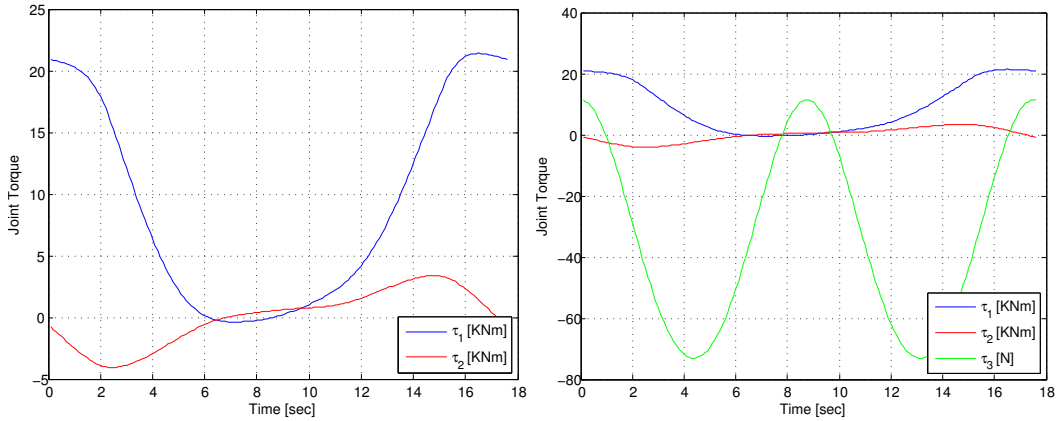

(a) (b)

Figure 4.25: Resultant joint torque from Spatial 3DOF dynamic model, for submerged cylindrical link RRP manipulator in quiescent water showing (a) joints one and two in detail and (b) all joint torques given an end effector design trajectory with a maximum period (T_{max}) of 17.5 s.

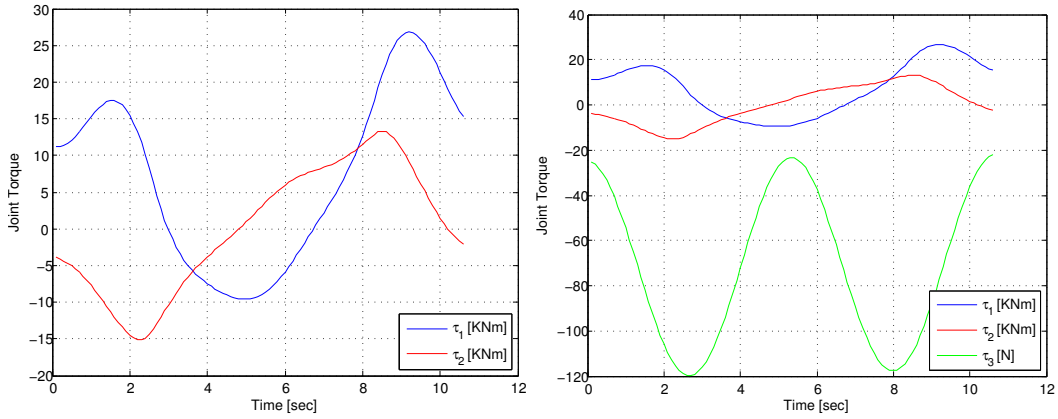

(a) (b)

Figure 4.26: Resultant joint torque from Spatial 3DOF dynamic model, for submerged cylindrical link RRP manipulator in moving water with waves showing (a) joints one and two in detail and (b) all joint torques given a minimum wave period (T_{min}) of 10.5 s.

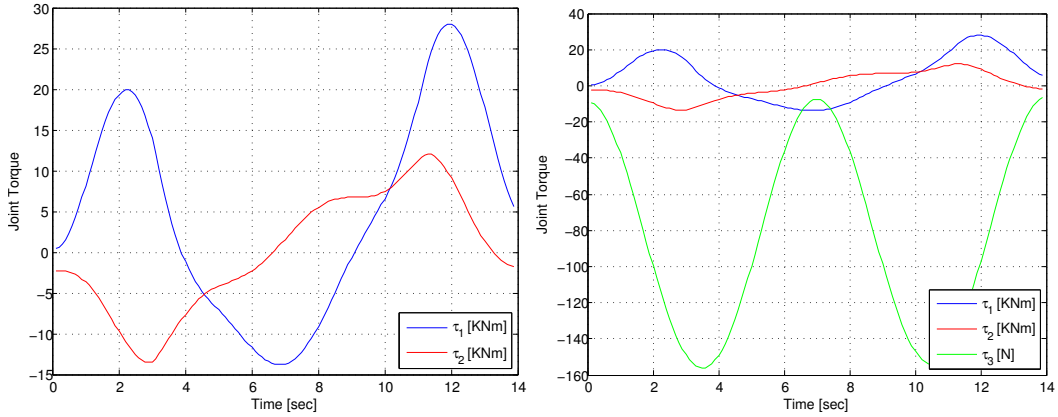

(a) (b)

Figure 4.27: Resultant joint torque from Spatial 3DOF dynamic model, for submerged cylindrical link RRP manipulator in moving water with waves showing (a) joints one and two in detail and (b) all joint torques given a average wave period (T_{avg}) of 13.8 s.

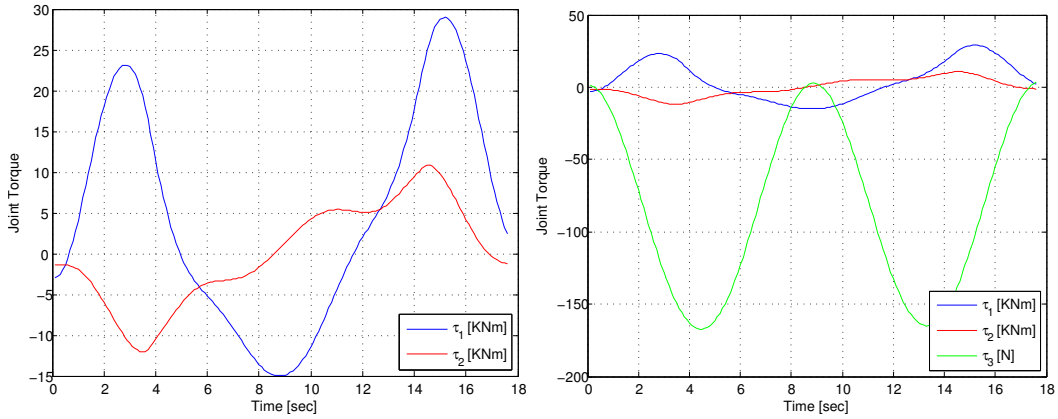

(a) (b)

Figure 4.28: Resultant joint torque from Spatial 3DOF dynamic model, for submerged cylindrical link RRP manipulator in moving water with waves showing (a) joints one and two in detail and (b) all joint torques given a maximum wave period (T_{max}) of 17.5 s.

4.3.5 Summary of Spatial 3DOF Dynamic Model Results

The spatial 3DOF RRP dynamic model accurately estimates the required joint torques of the potential device. The results are supported by the 2D dynamic model calculations derived in Section 4.2. The spatial 3DOF model results are slightly larger in magnitude in horizontal plane, joint 1, this can be attributed to the overall length of the simulated device. The 2D dynamic model uses a fixed length of L=8 m. However, the 3D dynamic model varies the overall link length d_3 with time to maintain a nominal extension of y_o=-8 m alongside the submarine. The effect of waves, using unimodal linear wave theory, is observed. It is interesting to note that dependent on the

position of manipulator within the phase of the wave, the wave current can assist sustaining the position of the manipulator by effectively lowering the required joint torque due to the direction of the fluid's acceleration vector. Contrarily, the opposite can be true were the wave current may potentially significantly increase actuator torque requirements.

Overall, the results emphasize the requirement to streamline the device. Similar to Section 4.2 findings, the required joint torques are large and primarily due to drag. Overall this model provides a basis for multi-body simulations, although it should be validated experimentally.

4.3.6 Simulation of Spatial 3DOF Dynamic Model with Self-Aligning Fairings

The spatial 3DOF dynamic model will be adapted to evaluate the effect of using self-aligning fairings on the device. Three prototype variations will be tested: one semi-faired design, with the base link faired, one semi-faired design, with the end link faired, and one fully faired design.

Although, manipulating a linear actuator with self aligning fairings may prove difficult to implement in reality. A design which is partially faired, and can retract and extend its faired section will be easier to implement mechanically. It is hypothesized the extending joint should be faired as the velocities and accelerations are larger at the end effector. While the design is retracted it will be fully faired, only when it is extend to its maximum

workspace bound will half the device be unfaired.

Self-aligning fairings are commonly used on tow cables to reduce drag [17]. They have also been used successfully on small semi-submersible vehicles [31]. The fairings are incorporated into the spatial 3DOF dynamic model through decreasing the 2D dimensionless drag coefficient by a factor of 10. While both the force due to added mass and the Froude-Krylov force remain the same as they are proportional to the breadth of the body relative to the onset flow, *i.e.*, the thickness of the fairings will be identical to the diameter of the unfaired cylinder for these test conditions. It should be noted the mass of the self-aligning fairings is not accounted for in the current simulation and would still need to be neutrally bouyant. The self-aligning fairings are assumed to align instantaneously. The results of the faired spatial 3DOF dynamic model are compared to the unfaired results in Figure 4.29 for an end effector design trajectory with a average period (T_{avg}) of 13.8 s design trajectory in quiescent water. While, the results of the faired spatial 3DOF dynamic model are compared to the unfaired results in Figure 4.30 for an average wave period (T_{avg}) of 13.8 s design trajectory in the presence of waves.

It is evident streamlining the device is required to produce a feasible full scale design. As expected the fully-faired device produces the best result, minimizing the overall required joint torques. The mechanical complexity of implementing a telescoping fully faired device is large and may not be merited. It is noted the end-faired design, as shown in Figure 5.1, also has

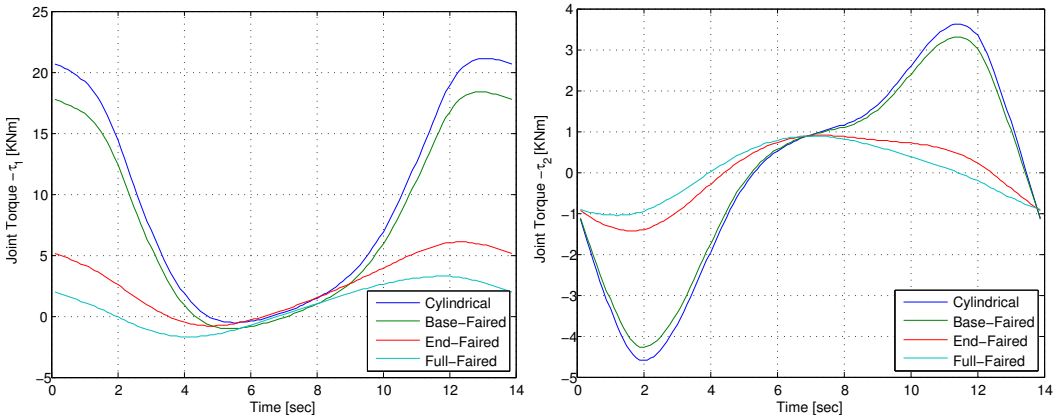

(a) (b)

Figure 4.29: Resultant joint torque from Spatial 3DOF dynamic model, for submerged faired link RRP manipulator in quiescent water showing (a) joint one and (b) joint 2 given an average wave period (T_{avg}) of 13.8 s.

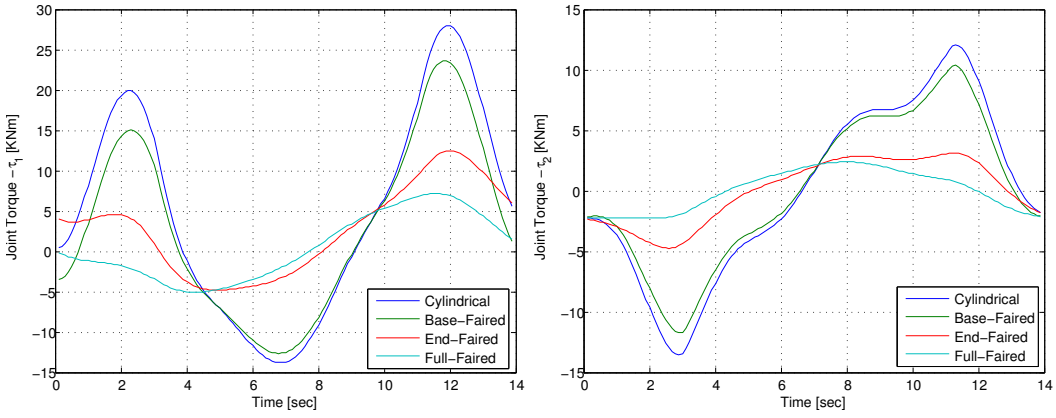

(a) (b)

Figure 4.30: Resultant joint torque from Spatial 3DOF dynamic model, for submerged faired link RRP manipulator in moving water with waves showing (a) joint one and (b) joint 2 given an average wave period (T_{avg}) of 13.8 s.

significantly improved performance over the unfaired design.

The end-faired RRP device is the more feasible design as it balances its mechanical complexity while minimizing the required actuation loads, producing a more robust overall mechanically actuated design. The end-faired RRP device will be used for further simulation and controller design.

Chapter 5

Control

A controller for the mechanically actuated, end-faired, RRP mechanism, shown in Figure 5.1, is developed to facilitate simulations of the docking process. The controller provides the mechanism with the ability to follow commanded set-point trajectories.

Conventional control schemes rely solely on the real-time feedback they receive to manipulate their control signal for the next time step. Some common conventional schemes are proportional-integral (PI), proportional-integral-derivative (PID), and Dahlin. These schemes are prevalent in industry, but have their shortfalls when dealing with non-linearities and actuator dead zones. Model based predictive control (MPC) uses a known or estimated model of the plant being controlled to minimize future predicted errors to improve closed-loop response. MPC schemes are convenient as raw data can be used potentially in real-time to develop the system models.

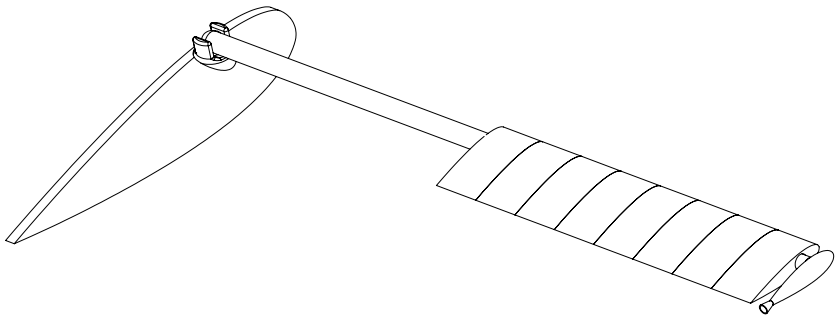

Figure 5.1: End-faired RRP prototype, using cylindrical link and NACA0015 fairings.

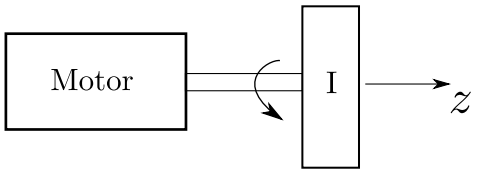

Figure 5.2: A generic model of servo driven revolute joint.

5.1 Characterization of RRP Actuators

The motor drive type varies per joint. Joints one and two will use a geared servo drive, as shown in Figure 5.2. Joint three will use a linear drive via a lead screw, as shown in Figure 5.3.

The actuator's behavior can be simulated by developing its transfer

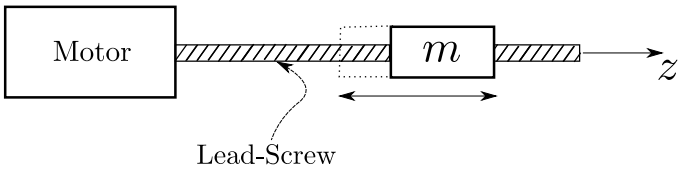

Figure 5.3: A generic model of a lead screw driven prismatic joint.

function. The transfer function of the actuator is equivalent to the transfer function of the plant, a controls term used to generically describe the system being investigated. Individual transfer functions are developed for each joint type. The transfer function is solved in Laplace form. The general transfer function is derived for a DC motor with reference to the general block diagram of the plant, shown in Figure 5.4. The torque produced by the motor through its armature, τ_m, can be described as,

$$\tau_m(s) = \left(\frac{K_\tau}{Ls + R}\right)\left(V(s) - \dot{\theta}_o(s)K_{\dot{\theta}}\right) \tag{5.1}$$

where K_τ is the motor torque constant, L is the motor inductance, R is the motor resistance, V is the input voltage, $\dot{\theta}_o$ is the motor velocity, and $K_{\dot{\theta}}$ is the motor back electro-motive force constant. The motor velocity can be described as a function of the motor torque and load torque, τ_L, where,

$$\dot{\theta}_o(s) = \left(\frac{1}{Js + B}\right)(\tau_m(s) - \tau_L(s)) \tag{5.2}$$

J is the inertia of the motor drive, and B is the damping of the motor drive. Substituting Eq. 5.1 into Eq. 5.2, the motor velocity can be described as a function of input voltage and load torque, where,

$$\dot{\theta}_o(s) = \frac{K_\tau V(s) - \tau_L(s)(Ls + R)}{JLs^2 + (JR + BL)s + (BR + K_\tau K_{\dot{\theta}})} \tag{5.3}$$

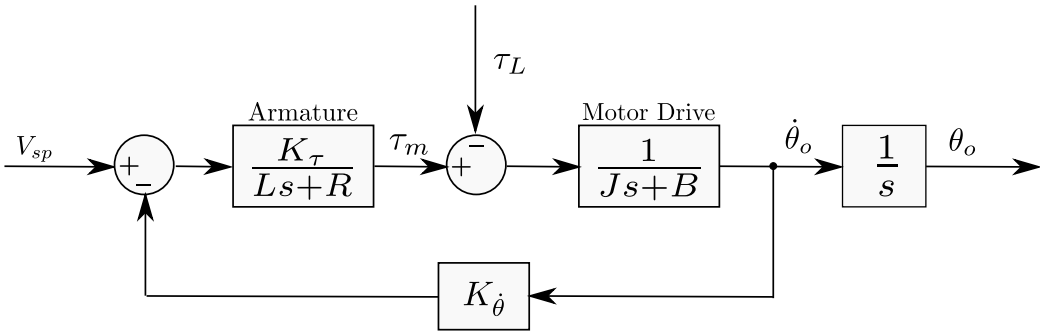

Figure 5.4: Block diagram of plant model of direct drive DC motor.

Given,

$$\theta_o(s) = \frac{1}{s}\dot{\theta}_o(s) \tag{5.4}$$

where $\dot{\theta}_o$ is the motor position. The motor position can be integrated from Eq. 5.3 and is described as,

$$\theta_o(s) = \frac{K_\tau V(s) - \tau_L(s)(Ls+R)}{JLs^3 + (JR+BL)s^2 + (BR + K_\tau K_{\dot{\theta}})s} \tag{5.5}$$

Similarly, the transfer function of the leadscrew actuator can be developed. The leadscrew actuator consists of a DC motor connected to a leadscrew, a traveler translates along the leadscrew due to the rotation of the DC motor and the pitch (lead) of the screw. The position of the traveler can be related to the position of the DC motor through the leadscrew's pitch gain, K_{LSp},

$$X(s) = K_{LSp}\theta(s) \tag{5.6}$$

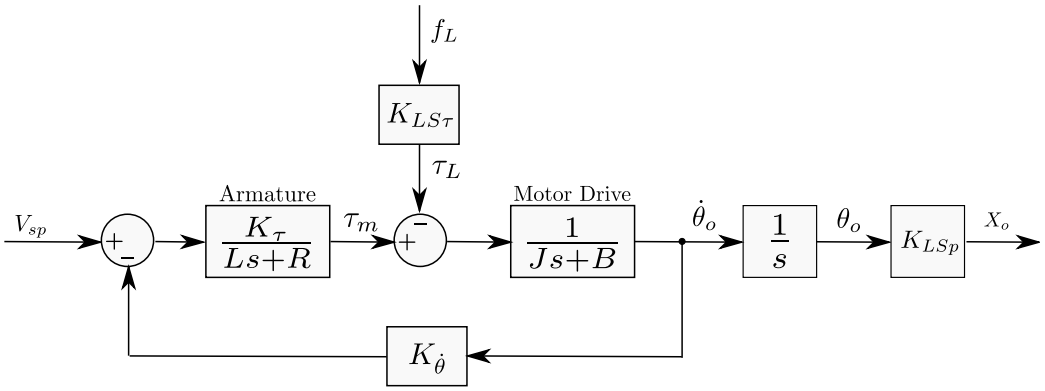

Figure 5.5: Block diagram of plant model of leadscrew actuator using a direct drive DC motor.

where X is the traveler position, and,

$$K_{LSp} = \frac{2\pi}{\lambda_p} \tag{5.7}$$

The torque load on the motor can be related to the force applied by the traveler, f_L, through,

$$\tau_L = K_{LS\tau} f_L \tag{5.8}$$

where $K_{LS\tau}$ is the leadscrew force gain,

$$K_{LS\tau} = \frac{f_L \lambda_p}{2\pi\eta} \tag{5.9}$$

and η is the leadscrew efficiency. Substituting Eq. 5.6, and Eq. 5.8 into Eq. 5.5, the leadscrew transfer function for position as a function of load

force and voltage input can be solved,

$$X_o(s) = \frac{K_\tau K_{LSp} V(s) - F_L(s) K_{LS\tau} K_{LSp}(Ls + R)}{JLs^3 + (JR + BL)s^2 + (BR + K_\tau K_{\dot{\theta}})s} \tag{5.10}$$

Eq. 5.10 is differentiated to obtain the transfer function of the leadscrew velocity,

$$\dot{X}_o(s) = \frac{K_\tau K_{LSp} V(s) - F_L(s) K_{LS\tau} K_{LSp}(Ls + R)}{JLs^2 + (JR + BL)s + (BR + K_\tau K_{\dot{\theta}})} \tag{5.11}$$

Given the specific transfer functions of the actuators response, the manipulator can now be characterized for control.

The joint actuators are sized using the estimated joint torques for the end faired RRP manipulator, shown in Figure 4.29, for the average wave period of 13.8 s. The kinematics of each joint are also considered when sizing the motor rpm and leadscrew pitch. Actuator parameters are approximated using industry specifications from commercially available systems. All joints are assumed to be ideal, flexibility and backlash within the motor drive will not be modelled.

Motors are selected based on the kinematic and torque requirements established for the average wave period and end-faired design case. Joint one uses a Kollmorgen KBM-260H03-A (480 V) DC direct drive motor to simulate its actuator, the specific motor parameters are given in Table 5.1. Similarly, Joint two uses a Kollmorgen KBM-260H01-A (480 V) DC direct drive motor for actuation, its parameters are displayed in Table 5.2. The third joint uses a Kollmorgen KBM-17H01-B (480 V) DC direct drive motor connected to a

Parameter	Value	Units
K_τ	119	N-m/A
$K_{\dot{\theta}}$	68.6	V/rad/s
J	9.56	kg-m^2
L	0.032	H
R	1.9	Ω
B	144486	N-m-s

Table 5.1: Joint one actuator parameters, approximated from a Kollmorgen KBM-260H03-A (480 V) DC direct drive motor.

Parameter	Value	Units
K_τ	59.3	N-m/A
$K_{\dot{\theta}}$	34.2	V/rad/s
J	4.88	kg-m^2
L	0.016	H
R	1.06	Ω
B	64914	N-m-s

Table 5.2: Joint two actuator parameters, approximated from a Kollmorgen KBM-260H01-A (480 V) DC direct drive motor.

24 mm Kerk LSSTKR-093-2000-XXXX leadscrew, the actuator parameters are given in Table 5.3.

The specific actuator's response is modelled using a step test. A step test consists of applying a unit step in input and observing the plants behavior over a time, both step tests for a unit voltage and unit load torque input are performed. From Eq. 5.5, the transfer function is discretized in software and joint one position can be observed due to both a unit step input in voltage, shown in Figure 5.6, and a unit step input of load torque, shown in Figure 5.8. Using Eq. 5.3, the same process can be applied to observe the behavior of the system velocity due to a unit step in voltage, shown in Figure 5.7, and

Parameter	Value	Units
K_τ	0.681	N-m/A
$K_{\dot{\theta}}$	0.393	V/rad/s
J	5.12E-5	kg-m^2
L	0.018	H
R	6.02	Ω
B	0.884	N-m-s
λ_p	0.0508	m
η	0.85	

Table 5.3: Joint three actuator parameters, approximated from a Kollmorgen KBM-17H01-B (480 V) DC direct drive motor, and a 24 mm Kerk leadscrew LSSTKR-093-2000-XXXX.

a unit step in load torque, as shown in Figure 5.9. Joint two response for position step tests is shown in Figure 5.10 and Figure 5.12 for both unit voltage and unit load torque respectively. Whereas, the velocity response step tests due to unit voltage and unit load torque inputs are shown in Figure 5.11 and Figure 5.13 respectively. Joint three uses Eq. 5.10, discretized in software, to develop the characteristics of the actuator's position due to a unit input voltage, shown in Figure 5.14, and unit input load force, as shown in Figure 5.16. Repeating the process using Eq. 5.11, the velocity response for joint three can be determined for a unit step in voltage, shown in Figure 5.15, and unit step in load force, as shown in Figure 5.17.

The data from the actuator characterizing can now be used to develop the controller. The normalized responses from the step tests are used to predict the future response of the actuator when a given set of input voltage and load is applied. This characteristic is the fundamental property used

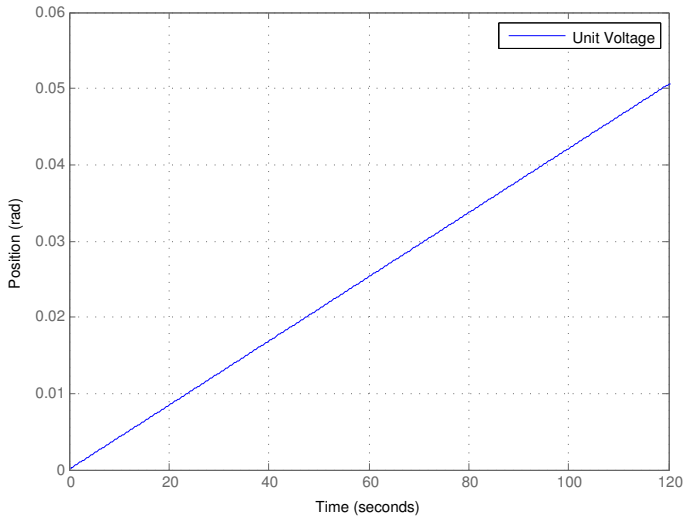

Figure 5.6: Unit step response of joint one actuator position due to unit voltage input.

when implementing the model based predictive control methodology.

5.2 Dynamic-Matrix-Control

Dynamic matrix control (DMC) is a linear model predictive controller commonly used and studied. DMC uses the plant's, *i.e.*, actuators, open-loop step tests along with an optimization routine to minimize future predicted errors to determine the best current control action, ΔU. DMC uses raw measured data or simulated data to develop the controller which lends itself well to implementing adaptive DMC control routines. DMC provides good robustness, with simplified tuning, and can compensate for non-linearities within the plant to a reasonable degree. DMC is efficient as it uses matrix

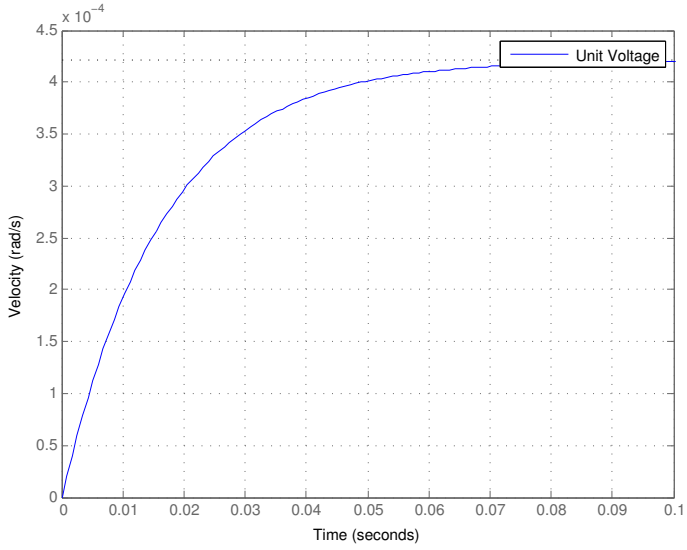

Figure 5.7: Unit step response of joint one actuator velocity due to unit voltage input.

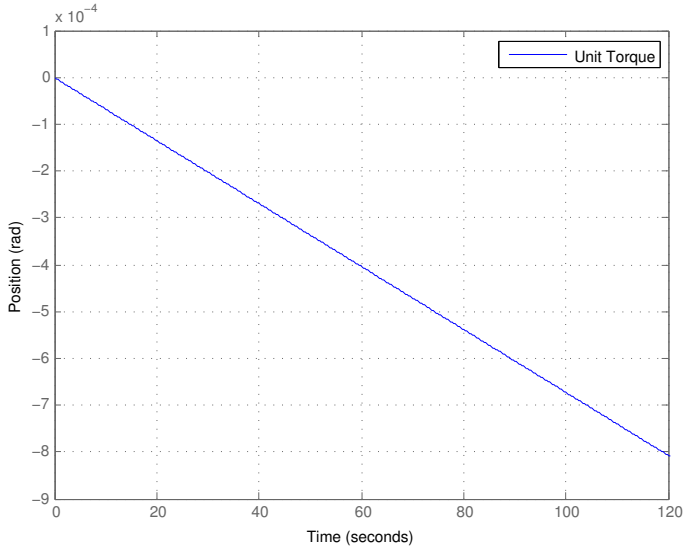

Figure 5.8: Unit step response of joint one actuator position due to unit torque input.

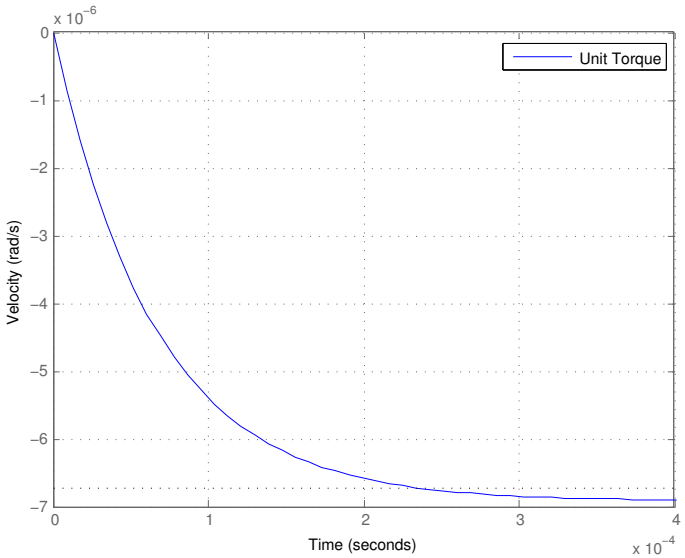

Figure 5.9: Unit step response of joint one actuator velocity due to unit torque input.

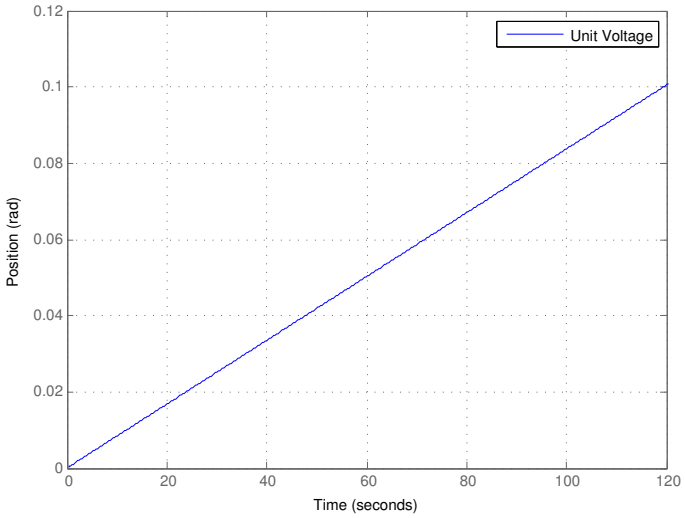

Figure 5.10: Unit step response of joint two actuator position due to unit voltage input.

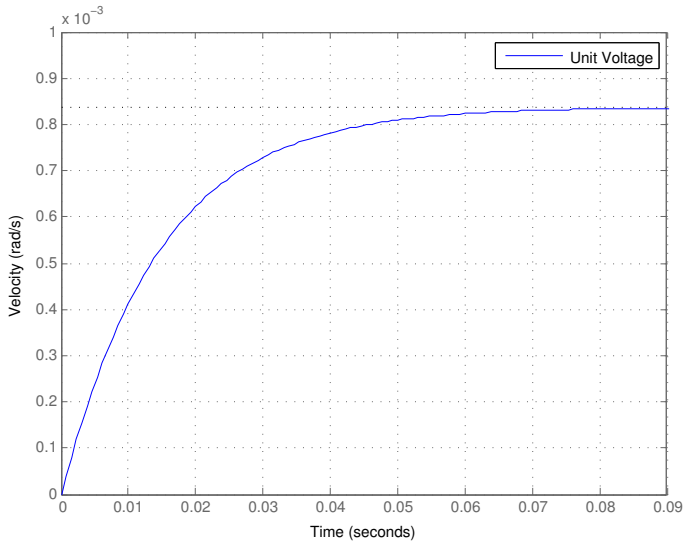

Figure 5.11: Unit step response of joint two actuator velocity due to unit voltage input.

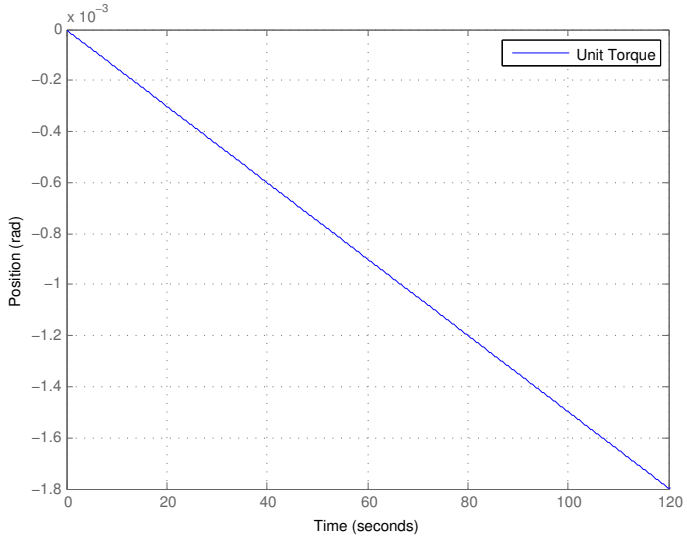

Figure 5.12: Unit step response of joint two actuator position due to unit torque input.

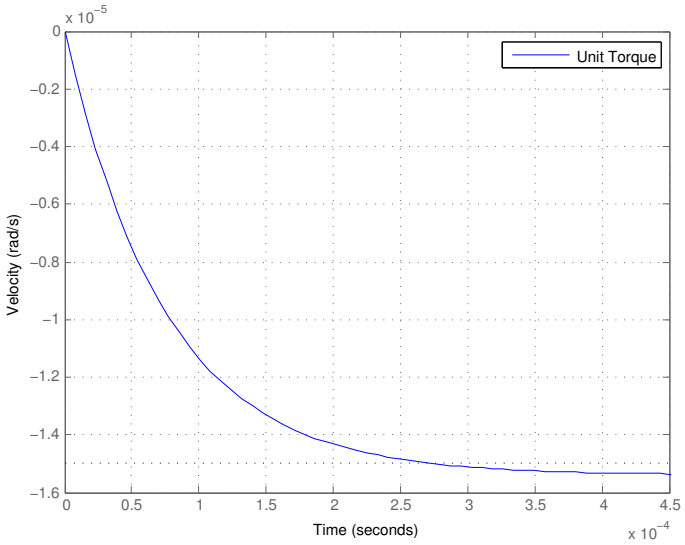

Figure 5.13: Unit step response of joint two actuator velocity due to unit torque input.

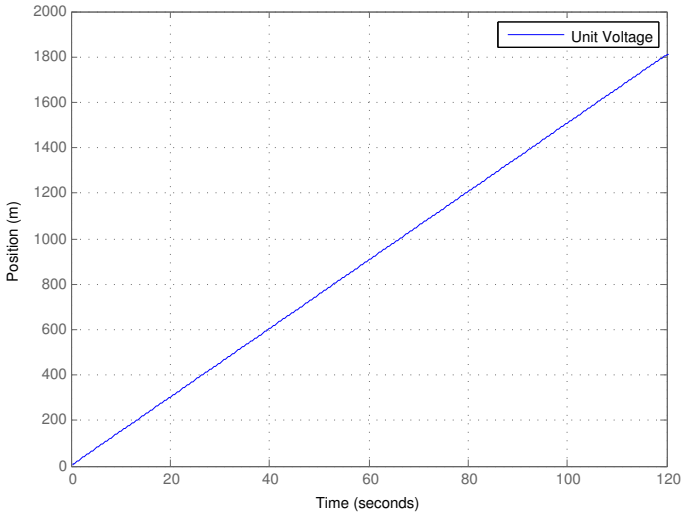

Figure 5.14: Unit step response of joint three actuator position due to unit voltage input.

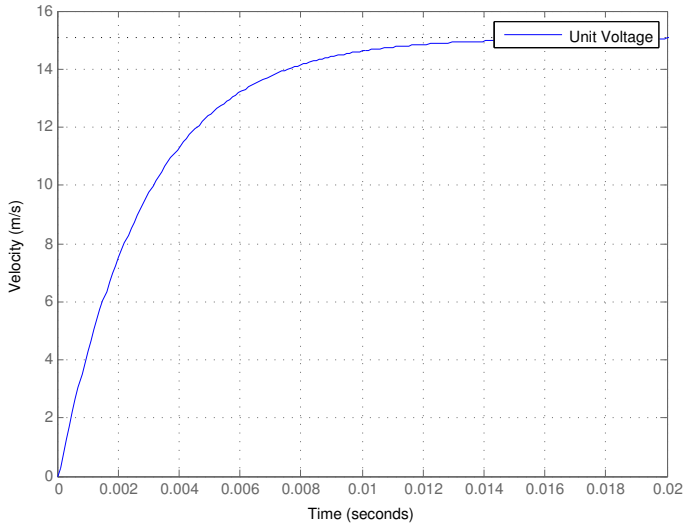

Figure 5.15: Unit step response of joint three actuator velocity due to unit voltage input.

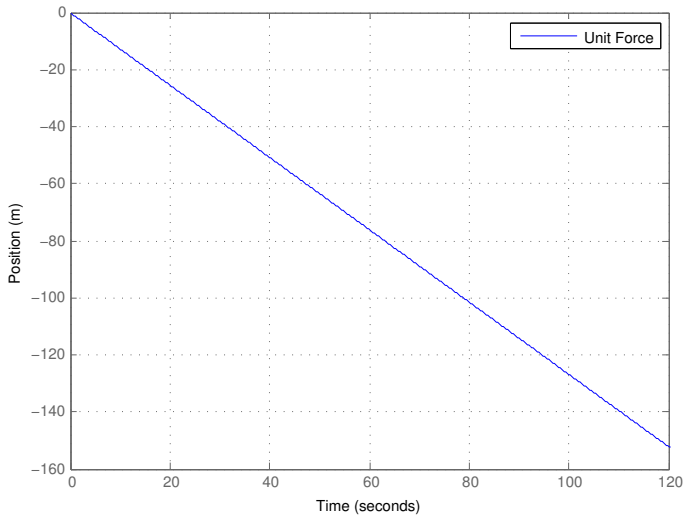

Figure 5.16: Unit step response of joint three actuator position due to unit torque input.

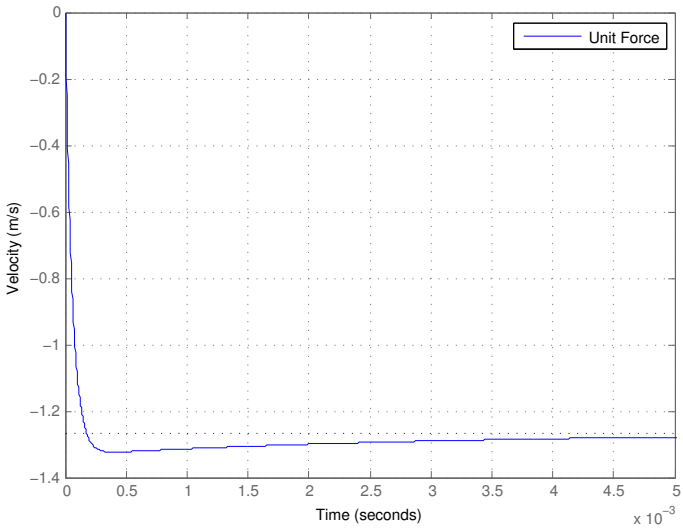

Figure 5.17: Unit step response of joint three actuator velocity due to unit torque input.

algebra for computations. It is suitable for both single-input-single-output (SISO) systems and multiple-input-multiple-output (MIMO) systems.

The conventional DMC control law is,

$$\Delta U = \left(A^T A\right)^{-1} A^T \left(y_{sp} - \hat{y}\right) \tag{5.12}$$

where A is a dynamic matrix, y_{sp} is a set point vector, and $\hat{y}$ is a vector of a predicted future plant response. The conventional control law can be adapted to include the predicted effects due to a disturbance on the system, and is given by,

$$\Delta U = \left(A^T A\right)^{-1} A^T \left(y_{sp} - \hat{y} - \Delta U_d B\right) \tag{5.13}$$

where ΔU_d is a scalar value of the change in disturbance, *i.e.*, load, and B is a vector of the plant response due to a unit step in load. The modified DMC control law can be developed with reference to Figure 5.18. First a prediction horizon, P, is defined as,

$$P = \frac{T_{ss}}{dt} \tag{5.14}$$

where T_{ss} represents the time it takes the plant to reach at least 95% of its steady state value, and dt is the time step. P is a scalar value and represents the duration of the response in time which is being predicted in time steps. A control horizon, n_u, is also defined and represents how many future control actions are predicted. It is useful to note although P is typically the length of time intervals the system requires to reach 95% of its steady state, this can be reduced to drive the system more aggressively or increased to reduce the control actions. A control horizon of $n_u = 2$ works well, it is important n_u is much less then P otherwise the controller will be unstable. Future control errors, e_i, are determined for $n_u = 2$ using a convolution method,

$$e_1 = (y_{sp_1} - (\hat{y}_1 + a_1\Delta U_0 + a_0\Delta U_1 + b_1\Delta U_d) \tag{5.15}$$

$$e_2 = (y_{sp_2} - (\hat{y}_2 + a_2\Delta U_0 + a_1\Delta U_1 + b_2\Delta U_d) \tag{5.16}$$

$$e_3 = (y_{sp_3} - (\hat{y}_3 + a_3\Delta U_0 + a_2\Delta U_1 + b_3\Delta U_d) \tag{5.17}$$

where a_i is element i of the open loop response of the plant due to an input

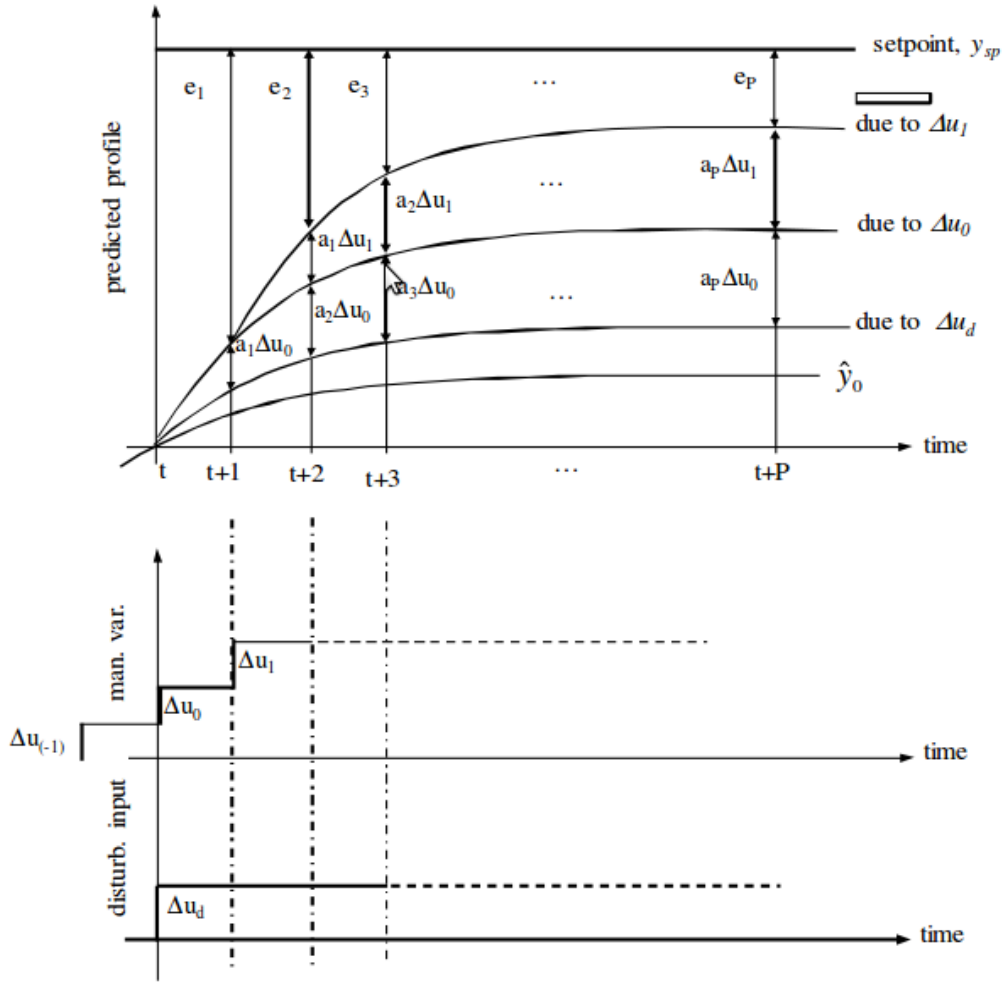

Figure 5.18: Dynamic Matrix Control disturbance model diagram [4]

voltage, and b_i is element i of vector B. The errors define a performance index, $I_{\Delta U}$,

$$I_{\Delta U} = {e_1}^2 + {e_2}^2 + {e_3}^2 + \ldots {e_p}^2 \tag{5.18}$$

which uses the method of least squares to define the objective function for the control action. The partial derivatives of $I_{\Delta U}$ with respect to ΔU_i can be obtained from i =0...n$_u$ and equated to zero to solve for the control action which minimizes the plant error.

$$\frac{\partial I_{\Delta U}}{\partial \Delta U_0} = 0 \tag{5.19}$$

$$\frac{\partial I_{\Delta U}}{\partial \Delta U_1} = 0 \tag{5.20}$$

Solving Eq. 5.19 and Eq. 5.20 for ΔU_i in vector format, the DMC control law presented in Eq. 5.2 is determined,

$$\Delta U = \left(A^T A\right)^{-1} A^T \left(y_{sp} - \hat{y} - \Delta U_d B\right)$$

where the dynamic matrix A is formulated using open loop response data,

a_i, for a given prediction horizon p and the control horizon n_u.

$$A = \begin{pmatrix} a_1 & 0 & 0 & \cdots & 0 \\ a_2 & a_1 & 0 & \cdots & 0 \\ a_3 & a_2 & a_1 & \cdots & \vdots \\ \vdots & \vdots & \vdots & \cdots & a_{P-n_u} \\ a_P & a_{P-1} & a_{P-2} & \cdots & a_{P-n_u+1} \end{pmatrix} \tag{5.21}$$

The specific DMC algorithm consists of 15 primary steps and is presented in Appendix A.

5.3 Controller Development

Typically robotic mechanisms are given a Cartesian point in space to follow as a trajectory while their control signals are evaluated in joint space. Initially solving the inverse solutions of the mechanism's kinematic equations a Cartesian position can be transcribed in terms of a joint angle to act as the controller set point. This allows individual controllers to be developed for each joint, simulating the RRP mechanism as three SISO systems operating in parallel. Joint one and two both use the simulation routine depicted in Figure 5.19 to control position. While joint three uses the simulation routine represented in Figure 5.20 to control position. The spatial 3DOF dynamic model is used to simulate load torques on the controller, the queiscent version is used for all tests except when disturbance is injected in the form of wave

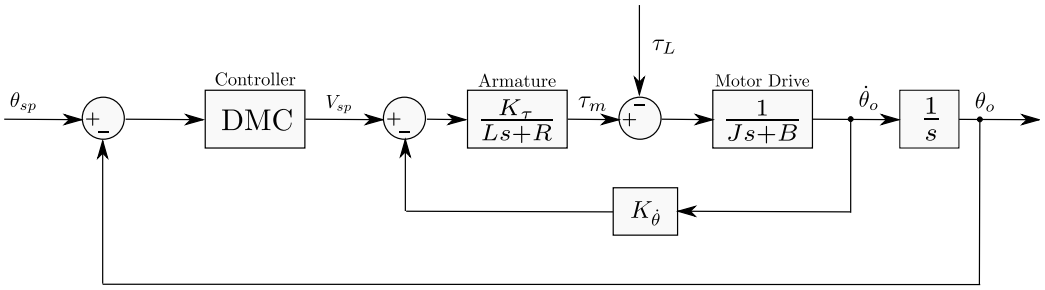

Figure 5.19: Block diagram of position control model of a direct drive DC motor.

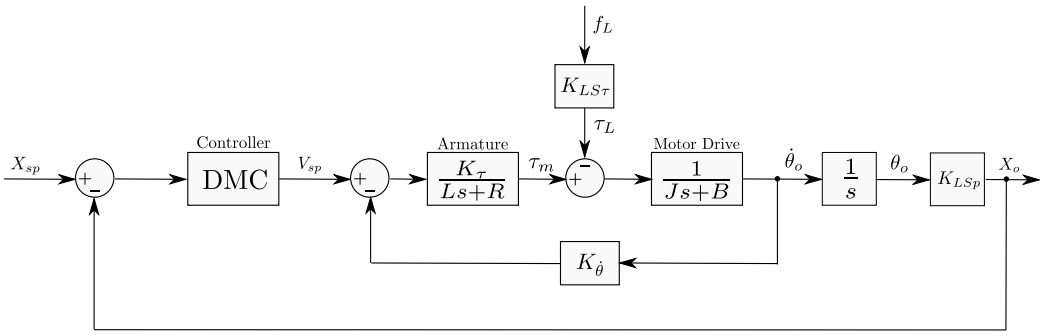

Figure 5.20: Block diagram of position control model of leadscrew actuator using a direct drive DC motor.

loading.

The position controller is developed using the open-loop data shown in Figures 5.6 through 5.17. Position responses of the motor due to a unit voltage input are used to develop the corresponding dynamic matrix for each actuator. While the position responses due to a unit load torque are used to generate the disturbance vector, B, for their respective actuator. The prediction horizon for each actuator is determined from the 95% steady-state interval of the velocity response due to a unit voltage input for each actuator.

Joint	Parameter	Value
One	P	33
	$\lambda_{\Delta U}$	1.01
	Sample Rate	100 Hz
Two	P	45
	$\lambda_{\Delta U}$	1.01
	Sample Rate	100 Hz
Three	P	48
	$\lambda_{\Delta U}$	1.01
	Sample Rate	100 Hz

Table 5.4: Controller parameters for end-faired RRP mechanically actuated manipulator simulation.

The velocity response is used to evaluate the prediction horizon because it is difficult to determine the steady-state value of a position response. The steady-state value of the position response occurs when its slope becomes constant, in other words, when its velocity reaches a constant value. It should be noted all step tests per actuator must be preformed with the same time step otherwise the prediction horizon will not be equivalent throughout the data for the controller. A tuning parameter, $\lambda_{\Delta U}$, referred to as move suppression is used to improve controller performance. Move suppression is a scalar value near one which multiplies the diagonal of the $A^T A$ term in the control routine. This effectively shifts the roots of the predicted plant used in the controller, allowing for more or less aggressive control actions to be sent to the actuators. The specific controller parameters are given in Table 5.4. These parameters are maintained for all test cases throughout control simulations.

The set point trajectory for the position simulation consists of two phase, a deployment phase from 0 to 600 seconds where the device is extended alongside the submarine to a steady-state position, and a tracking phase consisting of 10 cycles of the AUV design trajectory at sea state 6 given the average wave period of 13.8 s. The results of the total trajectory are shown in Figure 5.21. Note the initial transient error at the beginning of the trajectory is due to the simulation having limited data an the initial few time steps, the real system will have measurable feedback from its sensors. The controller appears to preform well during the deployment phase, however, lags in the AUV tracking phase shown in Figure 5.22. Figure 5.23 shows the controlled torques compared to the expected torques predicted by the dynamic modelling. Although the actuated joint torques differ slightly then the predicted joint torques, the actuated joints torques behave similar in phase and magnitude with the exception of joint one. The control torque in joint one is larger then expected due to the fact it is always lagging the set-point. This results in large control actions requiring larger torques to bring the system back to its setpoint.

To quantitatively evaluate the controllers performance the error is observed in Figure 5.24. The controller preforms well reaching a steady-state set point like those during the deployment phase but has some difficulty during tracking. Figure 5.25 shows the error during the AUV tracking phase. This shows two interesting traits, the steady offset in the x-axis error indicates the joint one actuator is insufficient in size to maintain the required position,

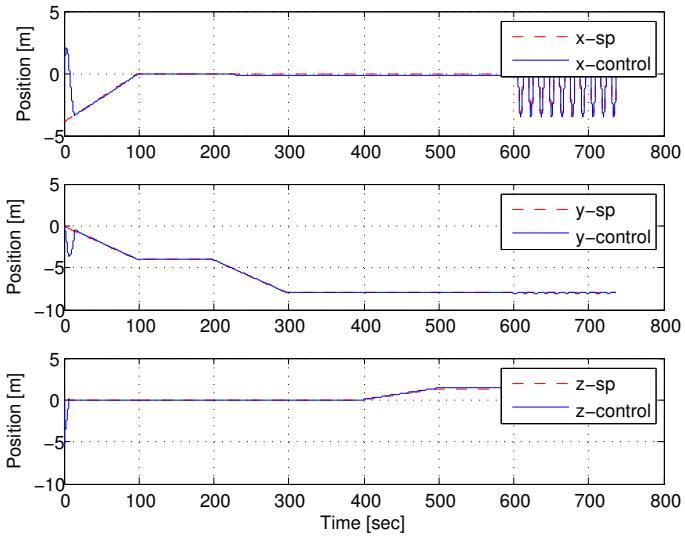

Figure 5.21: RRP end-faired manipulator controlled position for deployment phase and 10 cycles of AUV tracking at Sea-state (SS) 6.

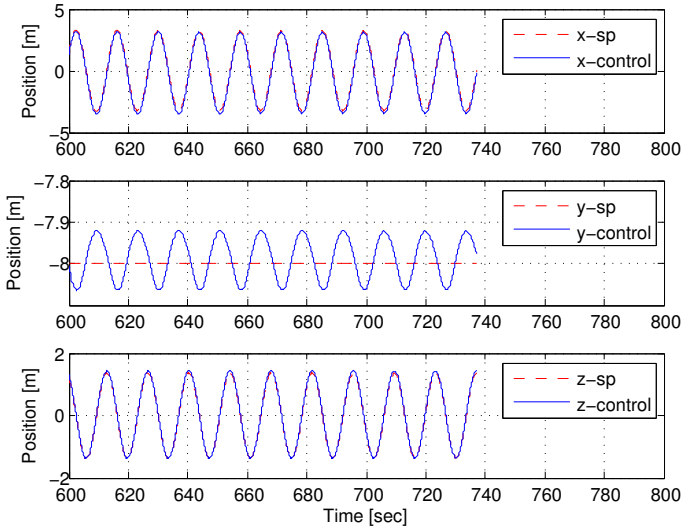

Figure 5.22: RRP end-faired manipulator controlled position for 10 cycles of AUV tracking at Sea-state (SS) 6.

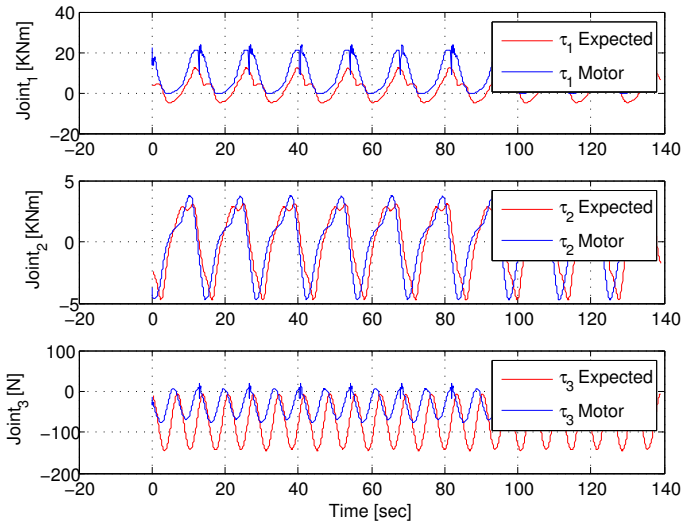

Figure 5.23: RRP end-faired manipulator controlled position motor torques for 10 cycles of AUV tracking at Sea-state (SS) 6.

and joint three's actuator appears to be to slow as its error oscillates evenly in both positive and negative direction. All errors appear to converge to a steady error profile after the first cycle. Figure 5.24 also shows an increase in error near $t = 300$ s corresponding to the extension of the mechanism from 4 m to 8 m alongside the submarine. This error during extension is shown in Figure 5.26 and again suggests the actuators, specifically joint one, may be insufficiently sized.

The effect of the sea-state on the controller performance is investigated. The original controller is used to track AUV trajectories of reduced sea-state with the comparison of absolute tracking error shown in Figure 5.27. The results show a decrease in transient error with each sea-state, this is expected as the amplitude of the set point trajectory decrease with sea-state.

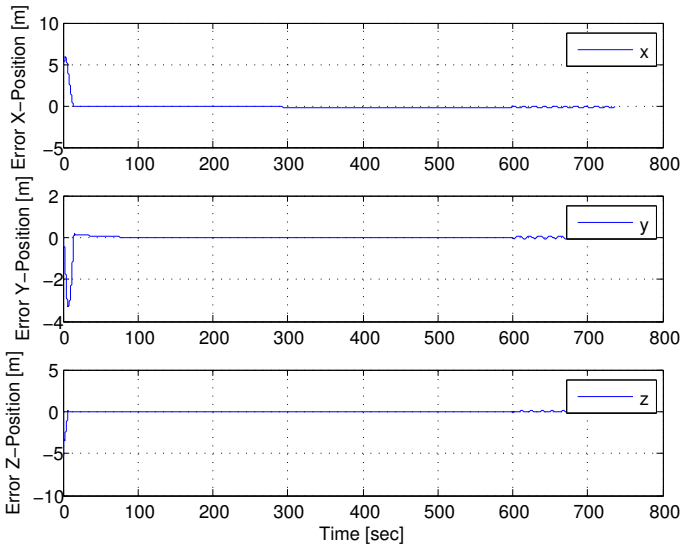

Figure 5.24: RRP end-faired manipulator controlled position error for deployment phase and 10 cycles of AUV tracking at Sea-state (SS) 6.

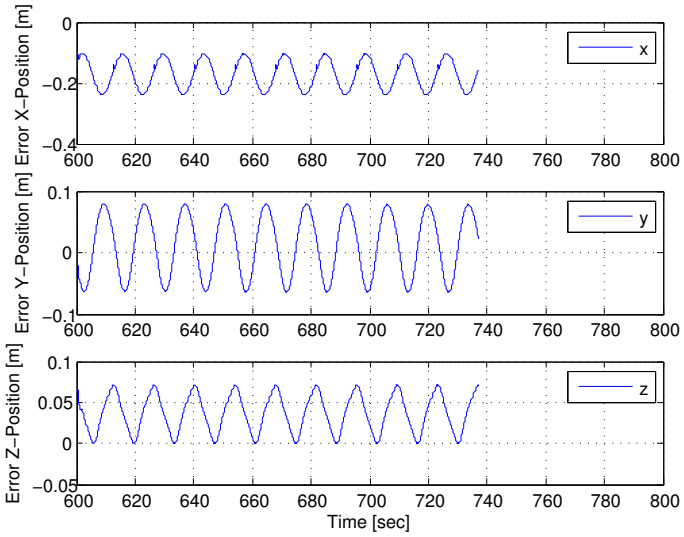

Figure 5.25: RRP end-faired manipulator controlled position error for 10 cycles of AUV tracking at Sea-state (SS) 6.

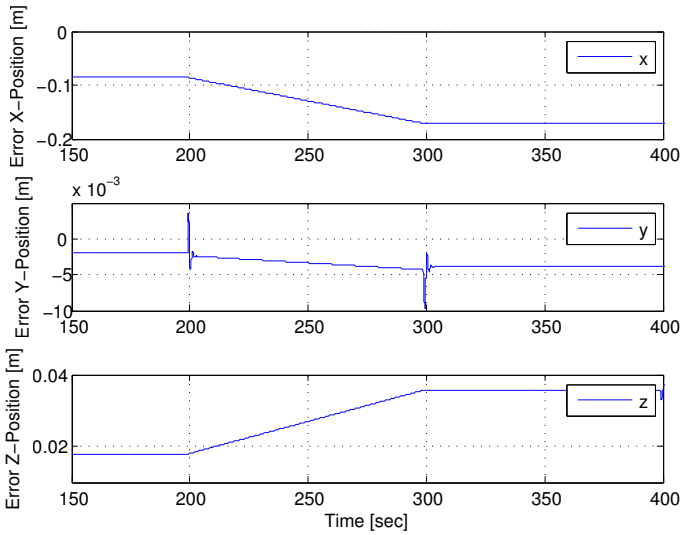

Figure 5.26: RRP end-faired manipulator controlled position error during extension of manipulator to 8 m at Sea-state (SS) 6.

What is more interesting to note is regardless of sea-state the mean error, shown in Figure 5.28, appear to converge to the same limit. This suggests the system is limited by its parameters and controller more than its operating conditions.

Tracking solely the transverse plane of the AUV trajectory is investigated, with results shown in Figure 5.29. The results show joint one is incapable of sustaining the manipulator's perpendicular position to the submarine. A comparison of the absolute error of fixing joint one during vertical tracking opposed to controlling joint one during vertical tracking is shown in Figure 5.30. The reduction in error is not significant and does not justify constraining the device to operating strictly in 2DOF. A 3DOF device will increase the probability of capture as it increases the devices workspace..

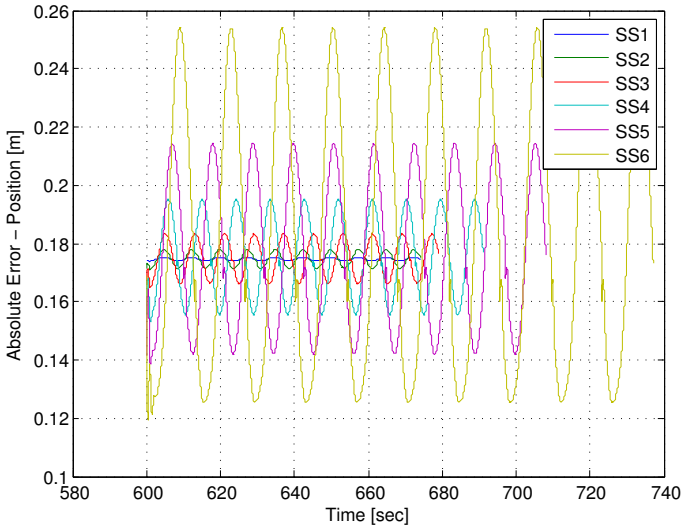

Figure 5.27: RRP end-faired manipulator controlled position error for 10 cycles of AUV tracking for ranging sea-states (SS).

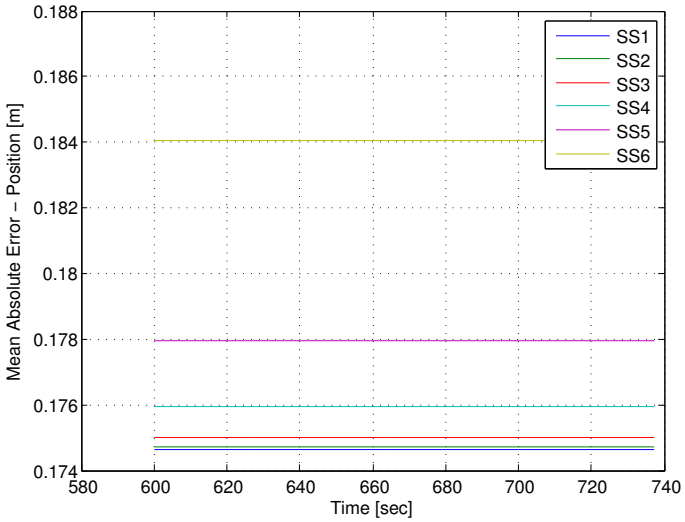

Figure 5.28: RRP end-faired manipulator controlled position mean error for 10 cycles of AUV tracking for ranging sea-states (SS).

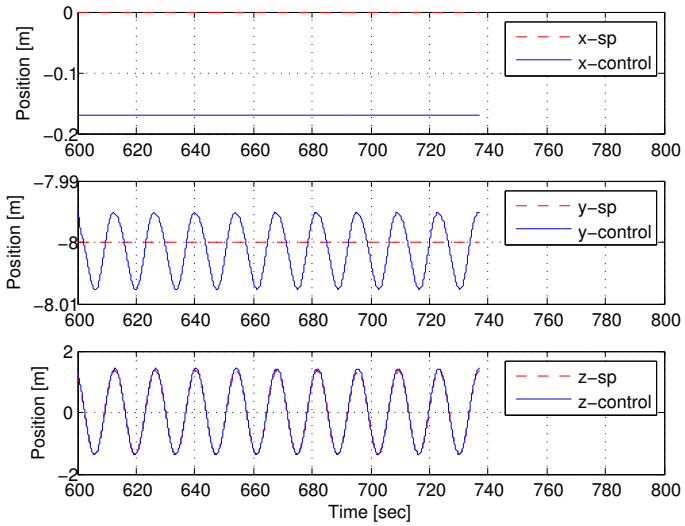

Figure 5.29: RRP end-faired manipulator controlled position for 10 cycles of AUV z-axis tracking at Sea-state (SS) 6.

Again, the error approaches a similar mean error which indicates the system is reaching a performance limit and a enhanced controller is required.

Indirect position control using a velocity controller is investigated. Hybrid position velocity controllers are often used when controlling motor positions. The controllers are typically set up as a mode selector scheme where the manipulated variable switches between a position error or velocity error based evaluation. The velocity controller can provide improved performance as it increases the order of the denominator of the transfer function which is being controlled, reducing the phase margin the controller must overcome when operating. However, controlling position using a velocity based controller is highly dependent on the initial position of the device. This is why both position based and velocity based position controllers are used in

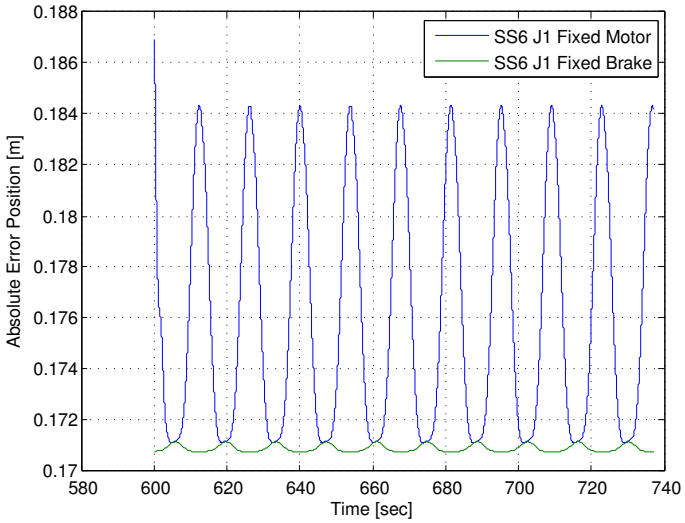

Figure 5.30: Comparison of RRP end-faired manipulator controlled position error for 10 cycles of AUV z-axis tracking at Sea-state (SS) 6, given a motorized joint one versus a mechanically fixed joint one during tracking.

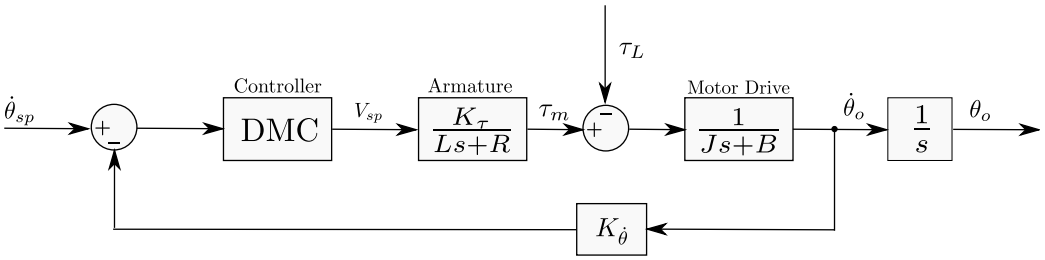

Figure 5.31: Block diagram of velocity control model of a direct drive DC motor.

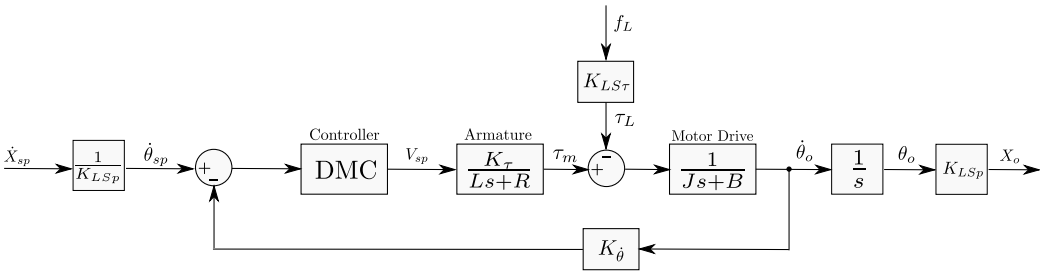

Figure 5.32: Block diagram of velocity control model of leadscrew actuator using a direct drive DC motor.

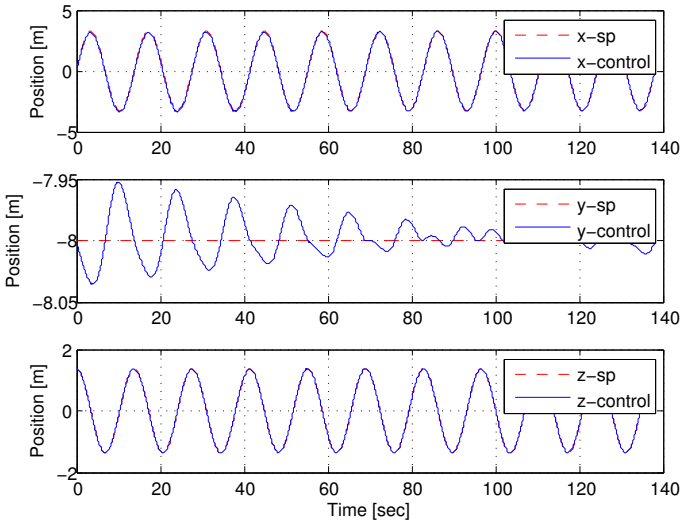

Figure 5.33: RRP end-faired manipulator position using velocity control for 10 cycles of AUV tracking at Sea-state (SS) 6.

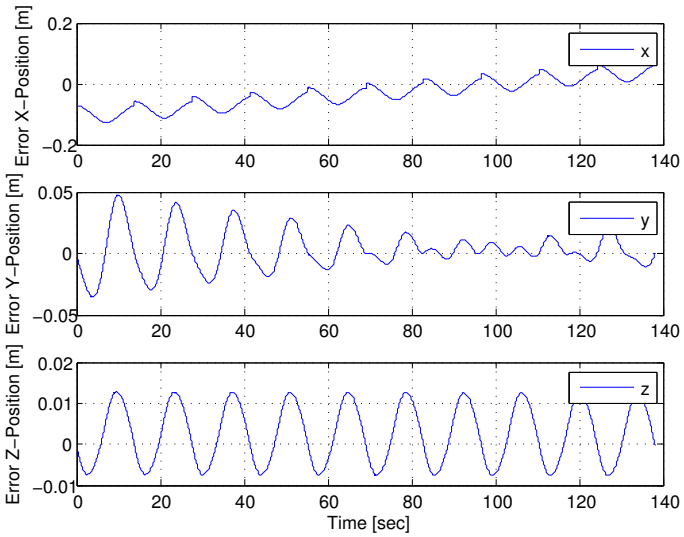

Figure 5.34: RRP end-faired manipulator position error using velocity control for 10 cycles of AUV tracking at Sea-state (SS) 6.

parallel. The control block diagrams are modified and given in Figure 5.31 and Figure 5.32 for both joint one and two, and joint three respectively. The velocity controller uses the open-loop velocity responses to generate its dynamic matrix a disturbance prediction vector. The results of the velocity based position controller are shown in Figure 5.33 with set point error given in Figure 5.34. The velocity based controller does show an improvement in tracking error over strictly position control shown in Figure 5.35. The velocity based controller can reduce the tracking error in position to below the 10 mm maximum error design objective, however, the response is highly transient.

To evaluate the robustness of the controllers a disturbance load was injected on the motor, in this case wave loading, *i.e.*, the Froude-Krylov

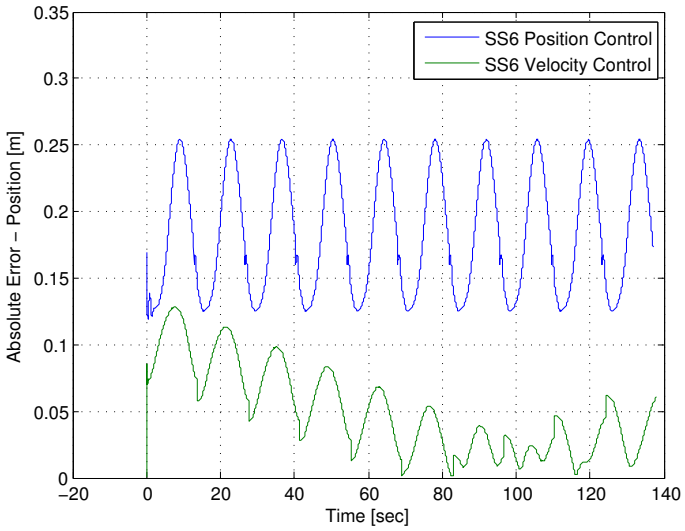

Figure 5.35: Comparison of position control error for 10 cycles of AUV tracking at Sea-state (SS) 6 between position based control versus velocity based control.

force. When the effects of the waves are introduced into the simulation the position controller can overcome the disturbance and drive the system back to relatively the same error profile. This is shown by comparing the variance in absolute tracking position error with and without disturbance shown in Figure 5.36. Despite an initial transient variance the position controller preforms relatively the same proving DMC is robust. When comparing the variance in error due to a disturbance with the velocity based position controller, Figure 5.37 shows an steady offset error due to the system being shifted with the initial disturbance. The disturbance changes the initial position, so although the velocity controller handles the disturbance well in terms of velocity it is incapable of ever correcting the systems position it can

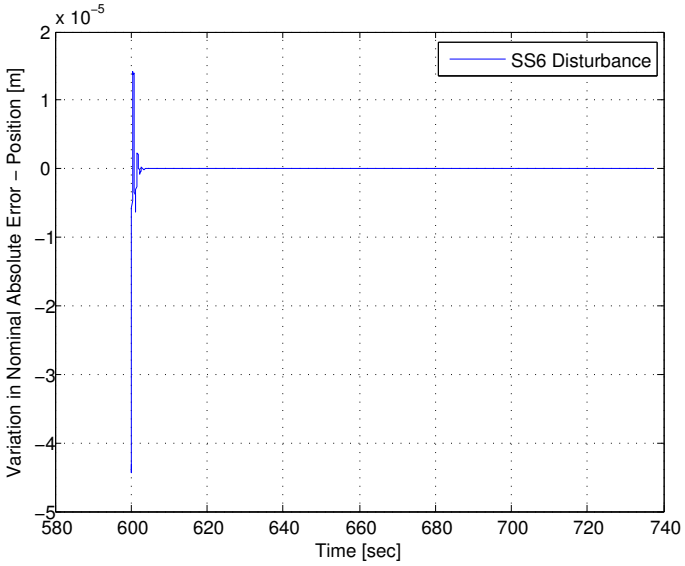

Figure 5.36: Variation in position control error due to disturbance using position based control for 10 cycles of AUV tracking at Sea-state (SS) 6.

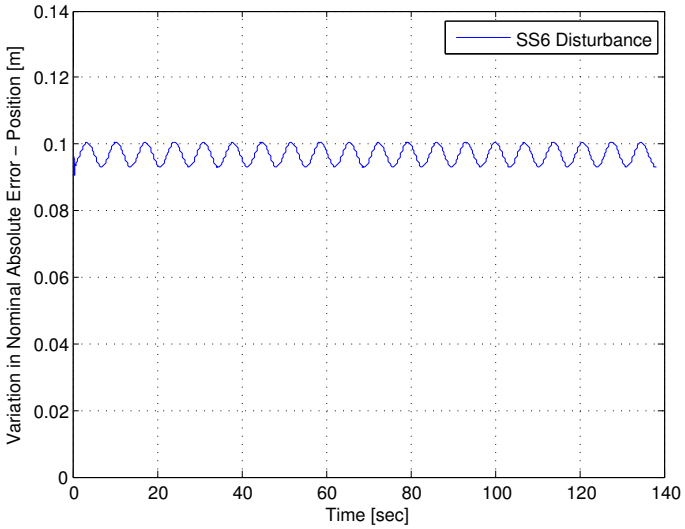

Figure 5.37: Variation in position control error due to disturbance using velocity based control for 10 cycles of AUV tracking at Sea-state (SS) 6.

only maintain it.

Overall, the DMC control scheme displays good promise. However, the system has a finite time constant which can not be overcome as is. A further enhanced controller and possibly faster response actuators are required to obtain good tracking of the nonlinear setpoint trajectory. This is necessary to minimize effects of phase lag and attenuation.

Chapter 6

Conclusion

AUV kinematics were simulated using unimodal linear wave theory, providing a basis for design trajectories for the manipulator. Hydrodynamic forces acting on the RRP mechanically actuated manipulator were successfully modelled using the Morrison equation. The hydrodynamic model was integrated into the conventional recursive Newton-Euler manipulator dynamics to produce an overall dynamic model for the manipulator.

It is shown drag is the largest contributer to hydrodynamic loading, proving streamlining of the device is essential to a feasible design. It is suggested the device be faired using self-aligning fairings. The end-faired RRP device is deemed the most feasible design as it balances its mechanical complexity while minimizing the required actuation loads, producing a more robust overall mechanically actuated design.

Actuation force may be reduced depending on wave direction. How-

ever, more sophisticated wave modelling is required to be conclusive. It may be possible to use wave loading to assist the mechanism when choosing when to intercept the AUV.

The DMC controller preforms well in tracking but does not reduce the absolute error to the design objective of 10 mm absolute error. The dmc position based controller is capable of minimizing the absolute error between the end effector and AUV within 0.17 m and sustains disturbances. While the velocity based dmc controller is capable of minimizing the absolute error between the end effector and AUV to within the 10 mm design goal, however, the velocity based controller can not accomodate position based disturbances. The initial control simulations show control is limited by the plant properties, *i.e.*, motor parameters. The time constant of the plant is finite and limits the performance the controller is capable of achieving, *i.e.*, steady-state error, during nonlinear tracking. In other words, the DMC controller can only drive the plant so fast and is incapable of overcoming this limit without a more enhanced controller design structure and/or actuators. The simulations show constraining the manipulator to 2DOF, tracking only the vertical plane of the AUV, does not significantly improve the performance. Varying sea-state does effect the transient error during non-linear tracking. However, the mean error, *i.e.*, steady-state error, seems to converge to the same limit regardless of sea-state. This suggests one controller can be implemented for all sea-states, although the current controller and plant properties need to be improved as the system has reached its performance limit. A hybrid position

velocity DMC controller was suggested and shows the error can potentially be reduced using velocity control. The velocity controller improved error within the 10 mm design limit as long as the manipulator is in the correct initial position prior to AUV tracking. The velocity based position controller does not handle disturbances well, if implemented it will have to operate in parallel with a direct position based controller to regain a steady position when the manipulator exceeds an acceptable position error during tracking. The hybrid position velocity DMC controller shows merit in investigating an enhanced control scheme for the mechanism.

Overall the design appears to be feasible. The device must be streamlined and sufficiently sized actuators are required. Constraining the device to solely actuate in the vertical plane does not appear to significantly improve performance, a full 3DOF device remains possible. The critical design problem to overcome for the full scale device is its controller. Regardless of the mechanism's design if control is not robust it will be incapable of AUV capture.

Recommendations

- Further analysis of self-aligning fairings should be completed. Perform testing to determine the optimal width of fairings and verify their loading effects on the device.

- Improve modelling to include vibrational effects and define minimum

link diameters to improve streamlining.

- Determine exact actuator specifications required for full scale device or prototype.
- Revise controller models using the real device through open-loop testing.
- Investigate more advanced adaptive controller to improve performance. Possibly generate open-loop plant data on the fly using initial conditions of the current state of the device. Also, investigate more advanced optimization routines within the DMC architecture to minimize error.

Bibliography

[1] *Unmanned surface vehicle (USV) payloads*, Tech. report, ODIM Brooke Ocean, April 2010, http://www.brooke-ocean.com/usv_main.html.

[2] *Launch and recovery systems (LARS)*, Tech. report, Rolls-Royce Canada Limited-Naval Marine, June 2012, www.brooke-ocean.com/handling_main.html.

[3] *Millennium plus ROV*, Tech. report, Oceaneering International Inc., 2012, www.oceaneering.com/rovs/rov-systems/millennium-plus-rov/.

[4] *1rm1579 – predictive control and intelligent sensors*, September 2013, http://noerpamoengkas.files.wordpress.com/2009/01/dynamic-matrix-controller.pdf.

[5] B. Allen, T. Austin, N. Forrester, R. Goldsborough, A. Kukulya, G. Packard, M. Purcell, and R. Stokey, *Autonomous docking demonstrations with enhanced remus technology*, Oceans 2006, September 2006, pp. 1–6.

[6] T. Aske, M. Barton, and T. MacKay, *Docking of unmanned underwater vehicles with submarines*, Senior Report, Deptartment of Mechanical Engineering, University of New Brunswick, April 2011.

[7] R. Bashour, M. Ansay, and D. French, *MARV, NUWC's mid-sized autonomous reconfigurable vehicle (MARV): Sub surface ship launch & recovery of a UUV efforts*, American Society of Naval Engineers Launch and Recovery Symposium (Arlington, Virginia), December 2010.

[8] J. Colwell, *Private communication 2009-09-10*, DRDC, September 2009.

[9] J. Cote, C. Gillis, and K. Hilton, *Docking autonomous underwater vehicles (UUV) on submarines*, Senior Report, Deptartment of Mechanical Engineering, University of New Brunswick, April 2011.

[10] S. Cowen, J. Breist, and Dombrowski, *Underwater docking of autonomous undersea vehicles using optical terminal guidance*, Oceans 97 vol 2 (Halifax), October 1997, pp. 1143–1147.

[11] J.J. Craig, *Introduction to robotics mechanics and control*, 3 ed., Pearson Prentice Hall, 2005.

[12] R. Fedor, *Simulation of a launch and recovery of an UUV to an submarine*, Master's thesis, KTH Royal Institute of Technology, Stockholm, Sweden, October 2009.

[13] M.D. Feezor, F. Yates Sorrell, P.R. Blankinship, and J.G. Bellingham, *Autonomous underwater vehicle homing/docking via electromag-*

netic guidance, Oceanic Engineering, IEEE Journal of **26** (2001), no. 4, 515 –521.

[14] P.J. From, J.T. Gravdahl, and P. Abbeel, *On the influence of ship motion prediction accuracy on motion planning and control of robotic manipulators on seaborne platforms*, 2010 IEEE Int. Conf. Robotics and Automation (ICRA), on, May 2010, pp. 5281 –5288.

[15] R. Granger, J. Smith, S. Somlyody, B. Thomas, and J. Labosky, *UUV docking and recharging station: Demonstration results and next steps*, Proceedings of the ASNE Launch and Recovery 2012 Symposium (Baltimore, USA), 2012.

[16] Joseph Katz and Allen Plotkin, *Low-speed aerodynamics*, 2 ed., Cambridge University Press, 2001.

[17] ODIM Spectrum Ltd., *Tufnose tufstream fairing systems*, September 2013, http://www.odimspectrum.com/fairings.html.

[18] NATO, *Stanag 4154: Common procedures for seakeeping in the ship design process*, NATO Military Agency for Standardization, 1998.

[19] United States Navy, *The navy unmanned undersea vehicle (UUV) master plan*, Tech. report, November 2004, www.navy.mil/navydata/technology/uuvmp.pdf.

[20] J.T. Park, B.H. Jun, P.M. Lee, and J. Oh, *Experiments on vision guided docking of an autonomous underwater vehicle us-*

ing one camera, Ocean Engineering **36** (2009), no. 1, 48 – 61, http://www.sciencedirect.com/science/article/pii/S0029801808002242.

[21] L. Scheutte, *Innovation opportunities in launch & recovery*, American Society of Naval Engineers Launch and Recovery Symposium, December 2010, Keynote Address, PowerPoint Presentation, www.navalengineers.org/publications/symposiaproceedings/Pages/LaunchandRecovery2010.aspx.

[22] M. Seizer, *An unmanned underwater vehicle launch, recovery, and onboard handling and servicing system (LROHSS) for use with unmanned surface vehicles*, American Society of Naval Engineers Launch and Recovery Symposium, December 2010, PowerPoint presentation, www.navalengineers.org/publications/symposiaproceedings/Pages/LaunchandRecovery2010.aspx, pp. 1143–1147.

[23] T. Sharpkaya and M. Issacson, *Mechanics of wave forces on offshore structures*, Van Nostrand Reinhold Company, 1981.

[24] J. Siesjö, *SUBROV, a versatile submarine ROV system, or getting a grip on AUVs*, American Society of Naval Engineers Launch and Recovery Symposium, 2010, www.rovonline.com/?p=100.

[25] M. S. Stewart and J. Pavlos, *A means to networked persistent undersea surveillance (U)*, Submarine technology symposium, Applied Physics

Laboratory University of Washington, General Dynamics Electric Boat, 2006.

[26] R. Stokey, M. Purcell, N. Forrester, T. Austin, R. Goldsborough, B. Allen, and C. von Alt, *A docking system for REMUS, an autonomous underwater vehicle*, OCEANS '97. MTS/IEEE Conference Proceedings, vol. 2, October 1997, pp. 1132–1136.

[27] Fredsøe J. Sumer, B.M., *Hydrodynamics around cylindrical structures*, London: World Scientific Pub, 2006.

[28] L.-W. Tsai, *Robot analysis*, John Wiley & Sons Inc., 1999.

[29] Det Norske Veritas, *Environmental conditions and environmental loads*, Recommended practice dnv-rp-c205, DNV, October 2010.

[30] G.D. Watt, *Estimates for the added mass of a multi-component, deeply submerged vehicle part I: Theory and program description*, Technical memorandum 88/213, Defence Research Establishment Atlantic, October 1988.

[31] G.D. Watt, *A fairing rotating about a distant axis*, CFD2001, the 9th Annual Conference of the CFD Society of Canada (Waterloo) (Ontario, CA), May 2001.

[32] G.D. Watt, *Active automated uuv docking with a slowly moving submarine*, American Society of Naval Engineers Launch and

Recovery Symposium, November 2012, PowerPoint presentation, https://www.navalengineers.org/publications/symposiaproceedings/Pages/LR12Proceedings.aspx.

[33] G.D. Watt, J.A. Carretero, R Dubay, and M.R. MacKenzie, *Towards an automated active UUV dock on a slowly moving submarine*, RINA Warship 2011: Naval Submarines and UUVs (Bath, UK), June 2011.

[34] G.D. Watt and M.R. MacKenzie, *Detailed design criteria rev-4*, DRDC Atlantic Technical Memorandum, January 2011.

[35] F.M. White, *Fluid mechanics*, 6 ed., McGraw-Hill, 2008.

Appendix A

DMC Algorithm

```
function [V,sigma,gamma,yhat,ysp,chat,U,phi]=dmc...
(motorstep,loadstep,P,Nu,alpha,lambda,ym,ysp...
,yspf,yhat,Umax,Umin,U,chat,tau_L,tau_L_m1)

%Outputs:
%V,sigma,gamma,yhat,ysp,chat,U,phi

%Inputs:
%motorstep,loadstep,P,Nu,alpha,lambda,ym,ysp,yspf,yhat,...
%Umax,Umin,U,chat,tau_L,tau_L_m1
Uold=U;

deltaU = zeros(Nu,1);
delta_Ud=zeros(Nu,1);
```

```
phi=zeros(P,1);
Au=zeros(P,Nu);
Aload=zeros(P,Nu);

%Build A matrix for motor position due to unit voltage
for i = 1:1:Nu
    for j = 1:1:P
        if(j<i)
            Au(j,i) = 0;
        else
            Au(j,i) = motorstep(j-i+1);
        end
    end
end

%Build A matrix for motor position due to unit load
for i = 1:1:Nu
    for j = 1:1:P
        if(j<i)
            Aload(j,i) = 0;
        else
            Aload(j,i) = loadstep(j-i+1);
        end
    end
end

%Create Big A
```

```
AtA = Au'*Au;

%Move Surpression
for i=1:size(AtA)
    AtA(i,i) = AtA(i,i)*lambda;
end

%Check the suitability of Big A
sigma=det(AtA);
gamma=cond(AtA);

for i=1:1:P
    if(i==1)
        ysp(i,1)=ym;
    else
        ysp(i,1)=alpha*ysp(i-1)+(1-alpha)*yspf;
    end
end

for i=1:1:P
   phi(i,1)=ym-chat;
end

yhat=yhat+phi;

delta_Ud(:,1)=(tau_L-tau_L_m1);
```

```
err(:,j)=ysp(2:end)-yhat;

deltaU(:,1)=(inv(AtA))*Au'*(err(:,j)-(delta_Ud(1)*Aload(:,1)));

U(:,1)=Uold+deltaU;

for i=1:Nu
if(U(i)>Umax)
    U(i)=Umax;
elseif(U(i)<Umin)
    U(i)=Umin;
else
    U(i)=U(i);
end
end

V=U(1);

deltaU=U-Uold;

yhat=yhat+Au(:,1)*deltaU(1);

chat=yhat(1);

for i=1:1:P-1
    yhat(i)=yhat(i+1);
end
```

Curriculum Vitae

Name of Candidate: Colin Blaine Gillis

Universities Attended:

- Bachelor of Science in Mechanical Engineering, Mechatronics Option
  University of New Brunswick, 2011
  Fredericton, New Brunswick, Canada

- Diploma of Engineering
  Saint Francis Xavier University, 2009
  Antigonish, Nova Scotia, Canada

Publications:

Refereed Journals

- Watt, G.D., Roy, A., Currie, J., **Gillis, C.**, Giesbrecht, J., Birsan, M., Seto, M., Heard, G., Carretero, J.A., Dubay, R., and Jeans, T., *A Concept for Docking a UUV with a Slowly Moving Submarine Under Waves*, IEEE Journal of Ocean Engineering, 2013JOE001317, *Submitted.*

- Currie, J., **Gillis, C.**, Carretero, J.A., Dubay, R., Jeans, T., and Watt, G.D., *Dynamics of Two Active Autonomous Dock Mechanisms for AUV Recovery*, Transactions of the Canadian Society for Mechanical Engineering, Vol. 38, No. 2, 2014, 13-CSME-189.

Refereed Conferences

- Currie, J., and **Gillis, C.**, Carretero, J.A., Dubay, R., Jeans, T., and Watt, G.D., *Dynamics of Two Active Autonomous Dock Mechanisms*

for AUV Recovery, Canadian Committee of the Theory of Machines and Mechanisms (CCToMM) - Mechanisms, Machines, and Mechatronics (M^3) Symposium 2013, Montreal, QC, Canada.

- Currie, J., **Gillis, C.**, *Development of Two Active Autonomous Dock Concepts for UUV Recovery with a Slowly Moving Submerged Submarine*, American Society of Naval Engineers (ASNE) Launch and Recovery Symposium 2012, Baltimore, MD, USA.